



An Experimental Study into the Effect of Damage on the Capacitance of Structural Composite Capacitors

T. CARLSON^{1,*} and L. E. ASP^{1,2}

¹Swerea SICOMP AB, Box 104, 43122 Mölndal, Sweden

²Luleå University of Technology, 97187 Luleå, Sweden

KEYWORDS

Multifunctional composites
Layered structures
Electrical properties
Matrix cracking

ABSTRACT

This paper presents the work to characterise the effects of tensile induced matrix cracks on capacitance of structural composite capacitor materials. The study is based on earlier work within the field of multifunctional materials where mechanical and electrical properties have been characterised. Effects of damage on electrical properties have, however, not been covered by earlier studies.

The structural capacitor materials were made from carbon fibre/epoxy pre-pregs as structural electrodes with thermoplastic PET as the dielectric separator. NaOH etching was used as a route for improved adhesion between the epoxy and PET to ensure matrix cracking in the CFRP electrodes occurred prior to delamination between the electrodes and the PET separator.

A method to induce and measure the effect of the matrix cracks on electrical properties was successfully developed and used in this study. The method is based on a simple tensile test and proved to be quick and easy to perform with consistent results. The structural capacitor material was found to maintain its capacitance even after significant intralaminar matrix cracking in the CFRP electrodes from high tensile mechanical loads.

© 2013 DEStech Publications, Inc. All rights reserved.

1. INTRODUCTION

The need for lightweight design and electrification are ever growing in consumer products, ranging from phones and laptops to road vehicles, etc. To meet these needs, novel approaches in material and product development are required. An elegant way to achieve lightweight energy storage is realisation of multifunctional materials and/or components, performing several tasks at once. This approach is particularly attractive since there is a limitation to the weight reduction achievable by optimisation of individual single purpose components and devices.

Chung and Wang [1] proposed the idea to exploit the semi-conductive nature of carbon fibres in “structural electronics” and to use CFRP laminas to make structural capacitors. The idea was realised in a follow-on study by Luo

and Chung [2] making thin structural capacitors from carbon fibre epoxy pre-preg laminate electrodes and different paper dielectric separators. Baechle [3], O’Brien [4], Wetzel [5] and co-workers have expanded the idea by making structural capacitors employing glass fibre/epoxy pre-preg as the dielectric separator with metalized polymer films as electrodes. More recently, Yurchak *et al.* [6] investigated the interlaminar shear strength of the metalized film electrode and the glass fibre composite separator for these devices. The study showed interlaminar shear strength as high as 39.6 MPa between the metalized polyimide electrode and the epoxy based glass fibre composite separator. The approach in [6] is very similar to earlier work performed by Carlson *et al.* [7–11]. Carlson *et al.* investigated multifunctional performance of a series of structural capacitors made in the spirit of Luo and Chung [2], employing carbon fibre composite electrodes and dielectric separator made from different surface weight printing paper or polymer films. The concept of making capacitors with carbon fibre epoxy pre-

*Corresponding author. Tel: +46(0)31 706 6376, fax +46(0)31 276130;
Email: tony.carlson@swerea.se

preg electrodes separated by a thin polymer film was found to be most promising [7–11].

The objective of the current investigation was to determine the influence of damage caused by tensile loading on the electrical performance of structural capacitor materials of the type developed in previous studies [10–11]. Intralaminar matrix cracks are well known to affect mechanical performance of a composite material, as reported by Varna *et al.* [12] and Gao *et al.* [13] among others. There are also concerns that matrix cracks may affect electrical properties of the structural composite capacitor material. By the current structural capacitor design, with structural electrodes and a ductile polymer separator film, it is believed that cracks in the electrodes caused by high tensile strains may be sustained without substantial loss in capacitance. However, to date no experimental studies have been performed to confirm this and consequently no method to perform such measurements is available. Hence, there is a need to develop a method to evaluate the effect of matrix cracks on the electrical performance in multifunctional composite materials. In this study we propose such a method to measure capacitance of a structural composite capacitor material under tensile loading, and present the first results on structural capacitor damage tolerance with respect to its capacitance. It should be noted that the work presented here is focused on the development of the testing method for the capacitance under influence of matrix cracks and not to correlate the cracks to the change in capacitance which is a whole field of study in itself.

2. MATERIALS

The structural capacitor materials were made from the same materials as in previous studies [10–11], using carbon fibre epoxy pre-preg woven laminas as electrodes separated by thermoplastic polyester (PET) dielectric film. The pre-preg was a 245 g/m² 2 × 2 Twill HS (3K) 0°/90° prepreg, MTM57/CF3200-42% RW, supplied by Cytec, UK, and the dielectric separator was a 50 µm thick (DuPont Mylar A), thermoplastic polyester film, supplied by Trafomo AB, Sweden.

Adhesion between PET and epoxy is generally poor and earlier studies [10–11] have proposed plasma treatment as a route for improved adhesion. In the current study NaOH was examined as a way to chemically etch the PET-film to provide better adhesion to the epoxy. A set of samples were prepared by etching the surface in 80°C NaOH solution (6.25 M) for 6 minutes according to the guideline by Huntsman for pre-treatment of PET [14]. The NaOH was supplied by Sigma Aldrich.

2.1. Composites Manufacture

Composite manufacture was done in the same manner as in previous work [7–11]. Laminates were stacked in the

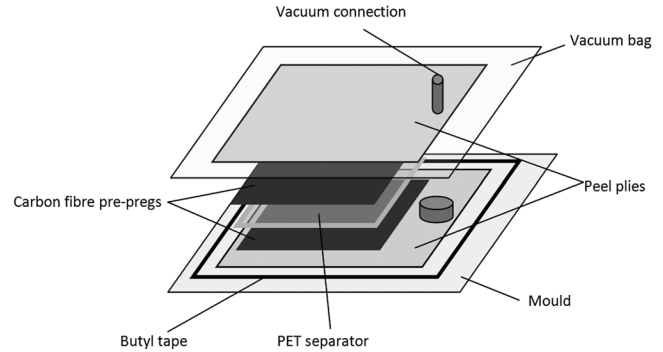


Figure 1. Schematic description of laminate manufacture.

desired configuration, vacuum was applied followed by debulking without heat for 30 minutes, and then cured according to the supplier's recommendations (120°C for 30 minutes). A schematic of the manufacture is shown in Figure 1.

2.1.1. Specimen Preparation

Firstly, interlaminar shear strength (ILSS) specimens were manufactured to allow evaluation of the effect of the NaOH etching of the PET-film on separator adhesion to the CFRP electrode laminates. ILSS specimens were made using a lay-up of [pre-preg₁₀/PET-film/pre-preg₁₀] providing a thickness close to that recommended in the ASTM standard for short beam interlaminar shear strength test [15]. Nominal specimen dimensions were 30.3 mm long, 10.1 mm wide and 5.05 mm thick.

For damage tolerance studies of the multifunctional composite material tensile structural capacitor specimens were made from four prepreg plies, two on each side of the PET film. The method developed here is based on the ASTM standard for tensile testing of composites [16]. The tensile test is well suited for introducing matrix cracks in the specimen and is straightforward to perform. Since the test is not aimed at measuring stiffness or strength, but merely to introduce matrix cracks, there is no need for full length specimens as recommended in the standard [16]. For this reason specimen smaller than that recommended in the ASTM standard, 160 mm long and 20 mm wide (c.f. the length 250 mm and width 25 mm in [16]) were prepared. The chosen lay-up resulted in

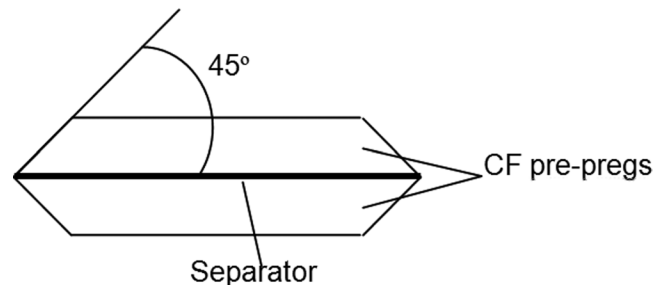


Figure 2. Principle cross-section of a tensile specimen for capacitance measurements.



Figure 3. Tensile capacitance specimen.

a theoretical nominal specimen thickness of 1.05 mm. These dimensions allow fitting of the extensometer and the electrical connections needed to perform the test. The tensile specimens were tabbed with 2 mm thick GFRP tabs bonded to the specimens with Araldite 2012 epoxy adhesive and cured overnight at room temperature. The tabs served two purposes, to provide a good grip in the tensile test machine and to electrically insulate the specimens from the tensile testing machine so as not to disturb the electrical measurement.

Specimen preparation required cutting, in this process short circuiting from carbon dust and bridging fibres at the edges was of concern. To mitigate short circuit in the specimens the edges extending parallel to the loading direction were grinded and polished in a 45° angle from the separator mid-plane, as schematically illustrated in Figure 2. A photograph of a specimen is shown in Figure 3.

A set of five specimens were made for both ILSS and tensile capacitance tests.

3. EXPERIMENTAL CHARACTERISATION

3.1. Measuring Effects of NaOH Surface Treatment

The motivation for finding a good surface treatment stems from the need to achieve intralaminar matrix cracks without prior delamination at the epoxy/PET-film interface. Earlier studies using plasma treatment to improve adhesion between epoxy and the PET separator have shown onset of delamination failure around 0.2% strain [10–11]. The early delamination failure onset is a problem in this study as delaminations may form prior to intralaminar matrix cracks, and well below the targeted strain level of 0.6%. In this study, the aim was to initiate intralaminar matrix cracks only. Intralaminar matrix cracks are commonly formed as the first mode of damage in composites during service serving as initiation sites for delaminations and fibre failures. The effect of intralaminar matrix cracks on the mechanical performance is usually small [12], whereas delaminations can be critical to the mechanical performance [17]. Matrix cracks and delaminations in a multifunctional composite capacitor are schematically illustrated in Figure 4.

Interlaminar shear strength (ILSS) was measured on the structural capacitor laminates to evaluate the effect of NaOH treatment of the PET-film on its adhesion to the CFRP electrodes. The results were compared to those achieved for neat and plasma treated PETfilms reported previously [10–11]. The interlaminar shear strength was evaluated at room temperature using the short beam three-point bending test ac-

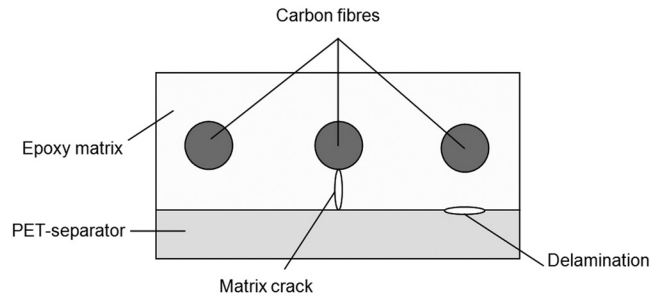


Figure 4. Schematic representation of undamaged and damaged structural capacitor composite.

cording to the ASTM D2344/D2344 M standard [15]. The equipment used was a MTS 20/M with a 10 kN load cell. A constant crosshead speed of 1 mm/min was used.

3.2. Damage Investigation

To get an insight in the amount of damage sustained by the specimens the crack density (cracks per length of specimen) was evaluated.

The angled edge used to avoid short circuit of the charged structural capacitor made it difficult to detect cracks during tensile loading. Therefore, after testing, completing a full loading-unloading cycle in tension and the capacitance measurements, the specimen's edges were grinded and polished to a 90° angle. The specimens were then fitted to the tensile tester again and loaded to a lower strain (approximately 0.3%) than before to open up the cracks making them possible to detect. A random 20 mm part of the specimen edge was chosen for close up microscopic evaluation using a portable USB microscope (Dino-Lite Pro) to determine the crack density in the specimen.

3.3. Measuring Effects of Intralaminar Matrix Cracks on Capacitance

To characterise the structural capacitor materials electrical performance the capacitance was measured by sweeping through 200 mHz–100 kHz at 1 V recording the electrical response (impedance spectroscopy). The equipment used was a Gamry Reference 3000 with Gamry Instruments Framework and Gamry Echem Analyst. A simple model for the structural capacitor material, shown in Figure 5, was used. In this model a capacitance (C) was connected in parallel with a resistance (R_2) and in turn connected in series with a resistor (R_1). C and R_2 are connected to the PET-films electrical properties whereas R_1 is connected to the electrical resistivity in the electrodes. The Echem Analyst software (Levenberg-Marquardt method) was used to find the best fit to the measured data by adjusting the parameters, R_1 , R_2 and C .

The specimens were electrically connected to the potentiostat by thin enamelled wires and copper tape with con-

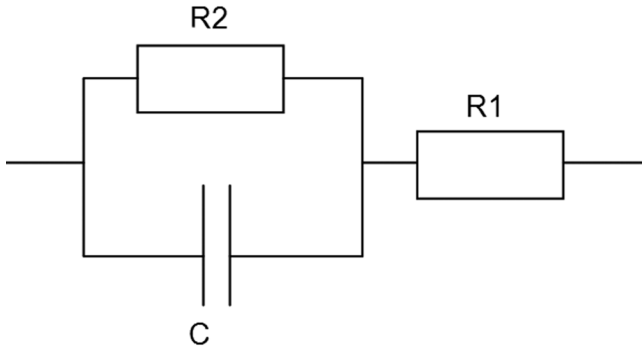


Figure 5. Structural capacitor electrical model.

ductive glue. This set-up is very flexible and allowed fast changes of specimen in the tensile test machine. A specimen mounted in the tensile tester is shown in Figure 6, where the extensometer has been removed for better visibility of the electrical wires. The position of the extensometer is visualised by the white areas on the surface of the specimen. Figure 7 illustrates the principle test setup.

The specimens were loaded in tension at a stroke of 1 mm/min up to 0.6–0.65% strain to introduce intralaminar matrix cracks in the structural capacitor CFRP electrodes. Matrix cracks typically occur beyond 0.2% strain [13]. Capacitance was measured before tensile loading, during tensile loading and after the load had been released. By this procedure a comparison of capacitance for undamaged specimens, specimens with open cracks and specimens with closed cracks was facilitated.

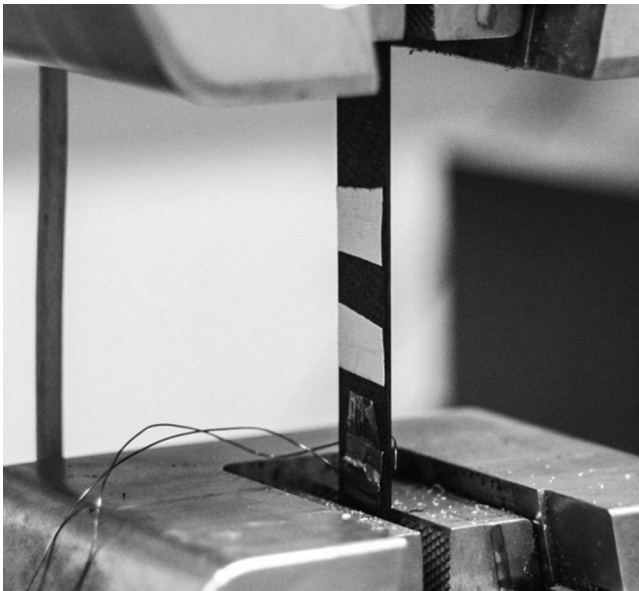


Figure 6. Specimen for measurement of capacitance with matrix cracks.

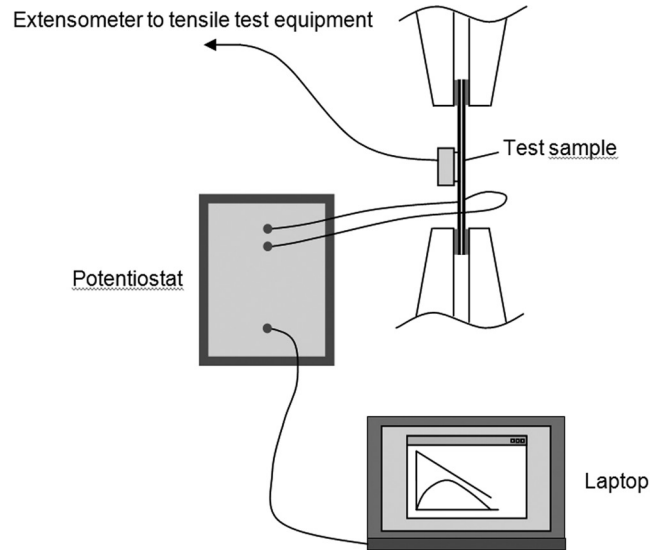


Figure 7. Principle test setup.

4. RESULTS

4.1. Effects of NaOH Surface Treatment on ILSS

Results of the effect on ILSS of NaOH treatment of the PET-film are presented in Table 1. In the Table, ILSS data for the same structural capacitor materials with plasma treated PET-film separator as well as for a full CFRP reference laminate are also presented for comparison. As seen in Table 1 the plasma treated capacitor material specimens showed significantly lower ILSS values than the CFRP reference. The NaOH treatment shows a modest improvement in performance compared to the plasma treated capacitor material, but its interlaminar shear strength is still significantly lower than that of the reference. Hence, neither plasma treatment nor NaOH etching provide strong adhesion between the CFRP electrodes and the PET separator. The NaOH etching was chosen for this study as it provides the best adhesion, and hence the least risk of delaminations forming prior to intralaminar matrix cracks during the tensile loading.

4.2. Damage Characteristics

The specimens were polished flat at the edges after testing to allow identification of matrix cracks present during the test. An average crack density of 0.26 cracks/mm was

Table 1. ILSS for NaOH Treated, Plasma Treated Structural Capacitor Materials and a CFRP Reference.

Sample	No Treatment [11]	NaOH	Plasma Treatment [11]
PET-film	29.5 ± 1.3	34.3 ± 0.6	29.6 ± 1.4
CFRP Ref.	54.4 ± 1.5	–	–

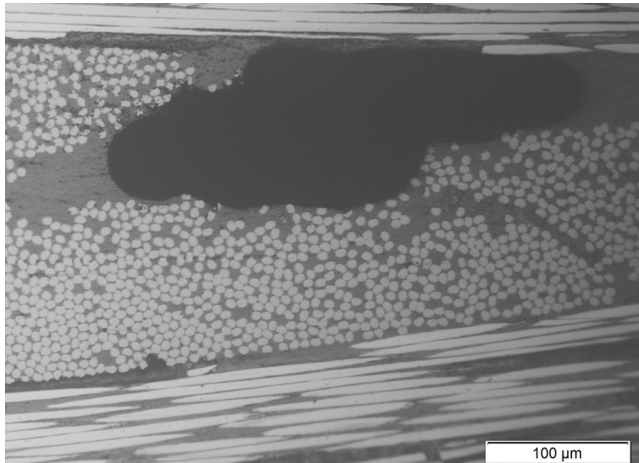


Figure 8. Close up of a typical pore inside the CFRP electrode.

found in the five specimens examined. However, it was very difficult to identify cracks due to the small crack opening displacement in the fairly thin laminates. Cracks were found to occur in all 90° bundles. In some cases the matrix cracks were found to link up to an existing pore (the out of autoclave manufacturing process resulted in some porosity of the laminates, usually found in the interface between the two plies of pre-preg). A typical pore is shown in Figure 8. Figure 9 shows typical matrix cracks, pointed out by the thin white arrows, in a specimen after testing. The middle crack is seen to link up with a pore in between the pre-preg plies. The PET separator is also clearly visible in the centre of the picture, extending from left to right and marked out by the thick white arrow. Figure 10 shows a close-up of a matrix crack with a white arrow indicating the location of a transverse crack in the vicinity of the PET separator film.

The crack density, and the corresponding crack opening displacement, was too small to result in any significant stiffness reduction. A stiffness reduction of approximately 0.15% was estimated for a crack density $\rho = 0.26$ cracks/mm using the approach by Varna and co-workers Lundmark [18]

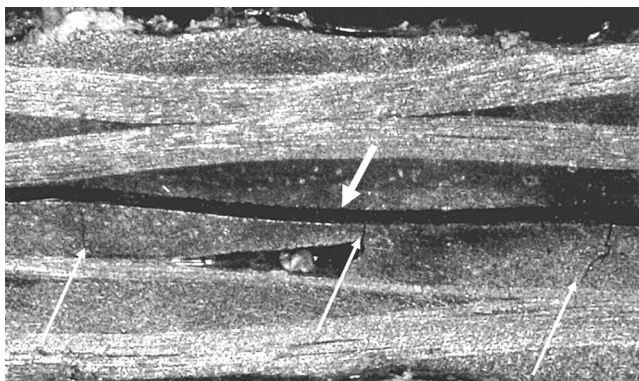


Figure 9. Matrix cracks (pointed out by thin arrows) in CFRP electrodes in a tensile capacitance specimen. The PET separator is identified by the thick arrow.

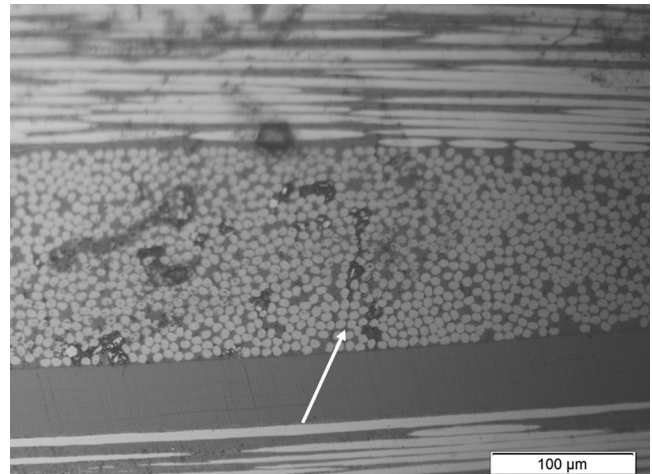


Figure 10. Close up on a matrix crack extending towards the PET separator film.

and Mattsson [18]. Consequently, only the effect of the presence of cracks on capacitance was evaluated experimentally.

4.3. Effect of Matrix Cracks on Capacitance

The results from the non-mechanically loaded capacitance measurements are presented in Table 2. A significant drop in capacitance for the NaOH treated film was observed compared to the non-treated and plasma-treated films. It should be noted that the geometry of the specimens measured are different for the different specimens; the non-treated and plasma treated specimens were square 100×100 mm and the NaOH specimens were 160×20 mm with angled edges. However, the geometric and connector type differences did not cause this significant drop in capacitance as the specimen geometry and connector was checked and found to provide capacitances of the expected level for non treated PET-film before proceeding with this study. Capacitance measurements were performed on the plates prior to cutting and specimen preparation for NaOH treated and non-treated PET capacitor. The results conclusively showed similar capacitances for plates and specimens of each kind, i.e. approximately 8 nF/m^2 for the NaOH treated and 440 nF/m^2 for the non-treated materials. Furthermore the validity of the connector was proven by consistent capacitance results for 100×100 mm square specimens with copper mesh connector, plates with copper tape connector and

Table 2. Capacitance of the Structural Capacitors.

Dielectric	Capacitance [nF/m ²]
PET-film 50 μm	447 ± 3.8 [9]
PET-film 50 μm 15s PT	442 ± 2.6 [9]
PET-film 50 μm NaOH	8.0 ± 4.1

Table 3. Capacitance Change with Matrix Cracks.

Dielectric	Capacitance nF/m ²		
	Before	Loaded	After
NaOH treated 50 µm PET	8.0 ± 4.1	3.9 ± 1.3	11.0 ± 3.0

finished 160 × 20 mm specimens with angled edges. NaOH etching creates a porous and rough surface [20] and for a thin film like the one used in this study this may affect the resistive properties of the whole film resulting in a lower dielectric constant. The rough surface provides better wetting and adhesion of the epoxy matrix in the electrodes which can result in a larger amount of epoxy at the electrode/separator interface effectively creating a thicker separator layer further reducing capacitance. However no general thickness increase by the formation of resin rich interface layers between the CFRP electrodes and the PET separator could be recorded by microscopy of polished samples. The drop in capacitance, caused by the NaOH treatment, does not cause a problem for the purpose of this study, where the change in capacitance from the formation of matrix cracks is sought. However, for realisation of structural capacitor materials of this design the NaOH etching of the PET-film is not advised.

The results from the capacitance measurements in the tensile test machine are shown in Table 3. As seen there was a significant drop, but not critical, in capacitance for the tensile loaded state (i.e. at 0.6% strain). This is found inherent to the opening of matrix cracks resulting in a lower dielectric constant for the insulating layer (consisting of the PET-Film and the epoxy matrix that sits in between the CF electrodes) since air has a lower dielectric constant than polymers. No other damage mechanisms, i.e fibre fractures or delaminations, were observed to occur in the tests. It should be noted that as the specimen was unloaded the capacitance was recovered, and was even higher than that before the mechanical load had been applied. The recovery was found inherent to complete crack closure as the specimens were unloaded (i.e. the small crack opening displacement observed in loaded specimens was found to vanish as cracks closed completely when the specimens were unloaded). A possible explanation for the gained capacitance is permanent plastic deformation of the insulating layer consisting of the PET-film and epoxy matrix resulting in a thinner separator after unloading than before introduction of matrix cracks. However this assumption has not been possible to confirm through inspection in an optical microscope.

The most important result is the fact that the capacitance of the structural capacitor is not critically affected by mechanical damage in the structure.

5. CONCLUSIONS

In this study a method to investigate the effect of intrala-

minar matrix cracking on capacitance of structural capacitors has been developed and employed. The method developed for measuring capacitance with matrix cracks works very well and the use of simple specimen geometry, in a tensile test set-up, along with a versatile potentiostat makes the test applicable on other types of multifunctional composite devices, i.e. supercapacitors or batteries.

The structural capacitors developed and tested in this study were found to maintain their capacitance even after sustaining intralaminar matrix cracking in the CFRP electrodes all the way up to the PET separator. This result is very important as the material shows a significant robustness to perform its electrical function in a damaged state.

Further, the effects of different surface treatment on the separator have been studied. NaOH treatment performed in this study has been compared to the plasma treatment performed in earlier studies [7–11] and it has been shown that NaOH is not suitable as surface treatment for the PET-film in a multifunctional composite capacitor. The treatment will improve the adhesion to epoxy but it will simultaneously lower the capacitance of the device to an unacceptable level.

ACKNOWLEDGEMENTS

Financial support from the European Commission via the FP7 project grant no. 234236, StorAge is gratefully acknowledged. Mr. P. Bartolotta is gratefully acknowledged for his assistance with NaOH treatment, and mechanical testing. Mr. M. Loukil is gratefully acknowledged for his assistance with some microscopy work. Prof. J. Varna is gratefully acknowledged for his participation in valuable discussions.

REFERENCES

- [1] Chung DDL, Wang S. Carbon fiber polymer-matrix structural composite as a semiconductor and concept of optoelectronic and electric devices made from it. *Smart Matererials and Structures*, Vol. 8, p. 161–166, 1999. <http://dx.doi.org/10.1088/0964-1726/8/1/018>
- [2] Luo X, Chung DDL. Carbon-fiber/polymer-matrix compositors as capacitors. *Composite Science and Technology*, Vol. 61, p. 885–888, 2001. [http://dx.doi.org/10.1016/S0266-3538\(00\)00166-4](http://dx.doi.org/10.1016/S0266-3538(00)00166-4)
- [3] Baechle DM, O'Brien DJ, Wetzel ED. Design and processing of structural composite capacitors. Proceedings of SAMPE 2007, Baltimore, MD, USA, 2007. PMCid:PMC2265925
- [4] O'Brien DJ, Baechle DM, Wetzel ED. Multifunctional structural composite capacitors for U.S. army applications. *Proceedings of SAMPE 2006*, Dallas, Texas, USA, 2006.
- [5] Wetzel ED. Reducing weight: Multifunctional composites integrate power, communications and structure, *AMPTIAC Quarterly*, Vol. 8, p. 91–95 2004.
- [6] Yurchak OB, O'Brien DJ, Baechle DM, Wetzel ED. Shear properties of multifunctional structural capacitors. *Proceedings of SAMPE 2012*, Baltimore, MD, USA, 2012.
- [7] Carlson T, Ordéus D, Wysocki M. "Load carrying composites for electrical energy storage" SICOMP TR08-02, Swerea SICOMP, Sweden, 2008.

- [8] Carlson T, Ordéus D, Wysocki M, Asp LE. Structural capacitor materials made from carbon fibre epoxy composites, *Composite Science and Technology*, Vol. 70(7), p.1135-1140, 2010. <http://dx.doi.org/10.1016/j.compscitech.2010.02.028>
- [9] Carlson T, Ordéus D, Wysocki M, Asp LE. CFRP structural capacitor materials for automotive applications, *Plastics, Rubbers and Composites*, Vol. 40(6-7), p. 311-316, 2011.
- [10] Carlson T, Asp LE. Structural carbon fibre composite/PET capacitors—Effects of dielectric separator thickness, *Composites Part B: Engineering*, Vol 49, p. 16-21, 2013. <http://dx.doi.org/10.1016/j.compositesb.2013.01.009>
- [11] Carlson T, Asp LE. Plasma treatment—a route for improved adhesion between PET and epoxy in multifunctional composite capacitors?, *Proceedings of ECCM15 Venice, Italy*, 2012.
- [12] Varna J, Talreja R. Integration of macro- and microdamage mechanics for performance evaluation of composite materials, *Mechanics of Composite Materials*, Vol. 48(2), p. 145–160, 2012. <http://dx.doi.org/10.1007/s11029-012-9261-y>
- [13] Gao F, Boniface L, Ogin SL, Smith PA, Greaves RP. Damage accumulation in woven-fabric CFRP laminates under tensile loading: part 1. Observation of damage accumulation, *Composites Science and Technology*, Vol. 59, p. 123–136, 1999. [http://dx.doi.org/10.1016/S0266-3538\(97\)00231-5](http://dx.doi.org/10.1016/S0266-3538(97)00231-5)
- [14] Surface preparation and pretreatments, www.huntsman.com/adhesives, 2010.
- [15] ASTM Standard test method for short-beam strength of polymer matrix composite materials and their laminates, *Annual book of ASTM standards, West Conshohocken*, Vol. 15.03, p. 71–78, 2010.
- [16] ASTM Standard test method for tensile properties of polymer matrix composite materials and their laminates, *Annual book of ASTM standards, West Conshohocken*, Vol. 15.03, p. 79–91, 2010.
- [17] Asp LE, Nilsson S, Singh S, An experimental investigation of the influence of delamination growth on the residual strength of impacted laminates, *Composites Part A: Applied Science and Manufacturing*, 2001;32(9):1229–1235. [http://dx.doi.org/10.1016/S1359-835X\(01\)00075-6](http://dx.doi.org/10.1016/S1359-835X(01)00075-6)
- [18] Lundmark P. and Varna J., “Constitutive Relationships for Laminates with Ply Cracks in In-plane Loading”, *International Journal of Damage Mechanics*, Vol. 14(3), p. 235–261, 2005. <http://dx.doi.org/10.1177/1056789505050355>
- [19] Mattsson H.D. and J. Varna, Average strain in fiber bundles and its effect on NCF composite stiffness, *J. of Engineering materials and technology*, 129, p. 211-219, April 2007.
- [20] Garbassi F, Morra M, Occhiello E. Polymer Surfaces—From Physics to Technology, Revised and updated edition, p. 365, 1998.



Fabrication and Mechanical and Thermal Behaviour of Graphene Oxide/Epoxy Nanocomposites

DILINI GALPAYA¹, MINGCHAO WANG¹, CHENG YAN^{1,*}, MEINAN LIU², NUNZIO MOTTA¹ and ERIC WACLAWIK¹

¹*School of Chemistry, Physics and Mechanical Engineering, Queensland University of Technology, Brisbane, Australia*

²*i-Lab, Suzhou Institute of Nano-Tech and Nano-Bionics, Chinese Academy of Science, Suzhou, China*

KEYWORDS

Graphene oxide
Epoxy nanocomposites
Mechanical properties

ABSTRACT

Bulk amount of graphite oxide was prepared by oxidation of graphite using the modified Hummers method and its ultrasonication in organic solvents yielded graphene oxide (GO). X-ray diffraction (XRD) pattern, X-ray photoelectron (XPS), Raman and Fourier transform infrared (FTIR) spectroscopy indicated the successful preparation of GO. XPS survey spectrum of GO revealed the presence of 66.6 at% C and 30.4 at% O. Scanning electron microscopy (SEM) and Transmission electron microscopy (TEM) images of the GO showed that they consist of a large amount of GO platelets with a curled morphology containing of a thin wrinkled sheet like structure. Atomic Force Microscopy (AFM) image of the exfoliated GO signified that the average thickness of GO sheets is ~1.0 nm which is very similar to GO monolayer. GO/epoxy nanocomposites were prepared by typical solution mixing technique and influence of GO on mechanical and thermal properties of nanocomposites were investigated. As for the mechanical behaviour of GO/epoxy nanocomposites, 0.5 wt% GO in the nanocomposite achieved the maximum increase in the elastic modulus (~35%) and tensile strength (~7%). The TEM analysis provided clear image of microstructure with homogeneous dispersion of GO in the polymer matrix. The improved strength properties of GO/epoxy nanocomposites can be attributed to inherent strength of GO, the good dispersion and the strong interfacial interactions between the GO sheets and the polymer matrix. However, incorporation of GO showed significant negative effect on composite glass transition temperature (T_g). This may arise due to the interference of GO on curing reaction of epoxy.

© 2013 DEStech Publications, Inc. All rights reserved.

1. INTRODUCTION

Since its discovery in 2004 [1] graphene, an atomically thick sheet of sp^2 -hybridized carbon atoms in a hexagonal two-dimensional lattice has attracted a great attention from research community due to its extraordinary physical and electrical properties. The remarkable properties reported for defect free monolayer graphene include high values of its elastic modulus (~1 TPa), intrinsic strength (~130 GPa), thermal conductivity (~5000 W/mK) and specific surface area ($2630 \text{ m}^2\text{g}^{-1}$) [2,3]. The superior properties of graphene

are reflected in the graphene-incorporated polymer nanocomposites, showing greater mechanical, thermal, electrical, and other properties compared to neat polymer. However, since graphene sheets are inherently stacked in graphite due to the high van der Waals forces between adjacent layers, the exfoliation and incorporation of graphene into polymer matrix to synthesize graphene reinforced polymer is quite difficult. Graphene oxide differs from graphene in that it has oxygen functional groups attached to the graphite backbone. This makes GO sheets are more compatible and easily dispersed in organic polymers. In addition, GO sheets have wrinkles and have a higher surface roughness as compared to pristine graphene [4]. These wrinkled surfaces interlock extremely well with the surrounding polymer material, helping

*Corresponding author. Tel: +61731386630; Fax: +61731381516; Email: c2.yan@qut.edu.au

to boost the interfacial load transfer between GO sheets and the matrix. All these properties combined with fairly high strength of GO sheets (effective Young's modulus 207.6 ± 23.4 GPa) [5] render it as a promising candidate for polymer composites [6].

Several studies have been conducted to improve the properties of polymeric composites with GO based materials [6–8]. Wang *et al.* reported the incorporation of 0.3% of GO into polybenzimidazole (OPBI) enhanced Young's modulus by 17%, tensile strength by 33% and toughness by 88%. Significant toughness and fatigue life improvements through the addition of GO sheets to a thermosetting epoxy system have been established [7]. Because of oxygen functional groups, graphene oxide can be further functionalized which can effectively increase the reactive points on the GO surface, bring extra advantages to improve the dispersion and interactions of GO in polymer matrices. Many studies have reported significant improvement in polymer properties with the incorporation of functionalized GO [9,10]. One study reported that the less oxidized GO was more effective than nearly fully oxidized GO in terms of reinforcing polymers. The better reinforcement effect was attributed to the higher quality of GO with much fewer structural defects [11]. Zhang *et al.* found that polarity matching is crucial in improving the interaction between fillers and matrix and the dispersion of fillers. They have reported that the excessive oxygen groups on graphene disturbed the polarity matching and deteriorate the dispersion quality of GO in PMMA [12].

However, for the time being, a relatively limited number of studies have been reported on evaluating mechanical performance of GO incorporated epoxy nanocomposites. Herein, we report the mechanical and thermal behaviour of epoxy nanocomposites with various weight fractions of GO. Bulk quantity of GO was prepared by chemical oxidation method. Significant enhancement in tensile properties was achieved by incorporating small amounts of GO into epoxy matrix. It was also revealed that GO was significantly influence on epoxy curing reaction thereby reducing the glass transition temperature of epoxy matrix.

2. METHOD

2.1. Materials

Graphite flakes was purchased from Sigma Aldrich (pvt) Ltd, Australia and used as received. Epoxy resin (Araldite GY 191) used for this study is Diglycidyl Ether of Bisphenol A/F (DGEBA/F) and the curing agent(Hardener HY 956) is a low viscosity aliphatic polyamine (Triethylenetetramine/TETA). Both epoxy resin and curing agent were supplied by CG composites, Australia. The other chemicals used such as KMnO_4 , H_2SO_4 , H_3PO_4 , HCl , H_2O_2 , Acetone, Ethanol, Diethyl ether, DMF were purchased from Sigma Aldrich (pvt) Ltd, Australia.

2.2. Preparation and Characterization of Graphene Oxide

GO was prepared by oxidation of graphite flakes according to the method described by Marcano *et al.* [13] and dried in a freeze dryer at -51°C under vacuum for 72h. GO was characterized by X-ray diffraction (XRD, PANalytical Cu MPD) to determine the distance between layers. Raman spectra of bulk graphite and GO were recorded from 1250 to 3000 cm^{-1} on a RENISHAW inVia Raman microscope using a 532 nm edge filter laser beam. FTIR spectra were obtained using FTIR 5700 Nicolet Diamond ATR spectrometer. The spectrum resolution was 4 cm^{-1} in the wave length range from 800 to 4000 cm^{-1} . The 64 scans were performed to get the average spectrum. X-ray photoelectron spectroscopy measurements were performed with a Kratos Axis ULTRA X-ray photoelectron spectrometer (XPS) using monochromatic $\text{AlK}\alpha$ radiation ($h\nu = 1486.6\text{ eV}$). CasaXPS v 2.3.16 software was used to perform curve fitting and to calculate the atomic concentrations.

The microstructural characterizations were performed using a JEOL-7001F field-emission scanning electron microscope (FESEM) operated at 15 kV and a JEOL 1400 transmission electron microscope (TEM) operated at 120 kV. Dry GO powder was used for the FESEM analysis whereas clear solution of GO in DMF was dropped cast onto carbon coated copper TEM grid for TEM analysis. Samples for Atomic force microscope (AFM) imaging were prepared by depositing clear solution of GO in DMF on freshly cleaved mica surface. AFM images were taken using a BMT multiscan AFM with silicon tip. Tapping mode was applied to get the topography of the GO flakes at the scan rate of 1.2 Hz with surface area of $5\text{ }\mu\text{m} \times 5\text{ }\mu\text{m}$.

2.3. Preparation and Characterization of Graphene Oxide/Epoxy Nanocomposites

A homogeneous dispersion of GO in acetone (1 mg/ml) was obtained by employing an ultrasonicator at high amplitude for 1h. Then a certain amount of epoxy resin was added and the mixture was stirred for 15 min on a magnetic stirrer. Acetone was evaporated by stirring the mixture at 40°C for few hours on a hot plate with a magnetic stirrer. The mixture was vacuumed at same temperature overnight for the complete removal of acetone. Stoichiometric amount of hardener was added to the epoxy/GO mixture at room temperature and mixing was carried out in a high speed shear mixer (Thinky planetary mixer) at 2000 rpm for 5 min. The mixture was then poured into Teflon coated moulds after degassing in a vacuum oven for 30 min. Samples were pre-cured at room temperature for 24h and post-cured at 90°C for 6h.

Tensile test was performed according to the ASTM D638-10 standard with Instron tensile machine using dog-bone shaped tensile specimens. The tests were performed at con-

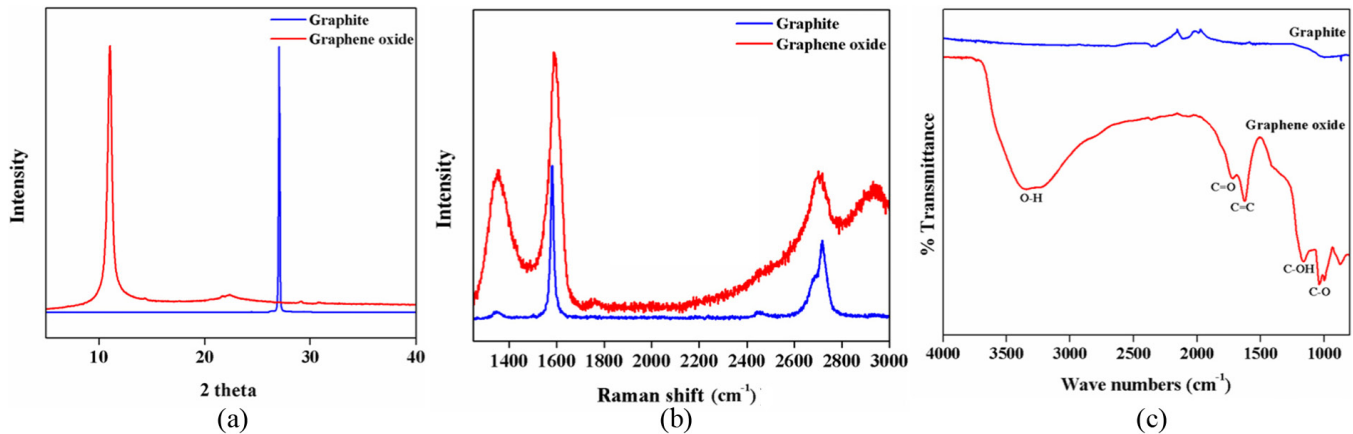


Figure 1. (a) XRD pattern; (b) Raman spectrum; (c) FTIR spectrum of graphite and graphene oxide.

stant loading speed of 0.5 mm/min with the 2 kN load cell at room temperature. At least five specimens were tested from each sample. Transmission electron microscopy specimens were prepared by microtoming nanocomposite samples with thickness of 40–70 nm. The specimens (on Cu grid) were examined with JEOL 1400 TEM using an accelerate voltage of 120 kV. The tensile fractured surfaces of samples were examined using FESEM (JEOL-7001F). The fractured ends of the specimens were mounted on aluminium stubs and sputter-coated with a thin layer of gold to avoid electrostatic charging during examination. Q100 *Chimaera* DSC was used to obtain glass transition temperature (T_g) of neat epoxy and nanocomposites. Experiments were carried out under nitrogen atmosphere at a scanning rate of 10°C/min from 0 to 280°C.

3. RESULTS AND DISCUSSION

3.1. Characterization of Graphene Oxide

GO is highly hydrophilic and is readily dispersible in water and other organic solvent such as DMF,

acetone etc. XRD pattern of GO (as prepared dry powder) and bulk graphite shows in Figure 1(a). A characteristic sharp (002) peak of graphite stacking appeared at $2\theta = \sim 26.5^\circ$ with a corresponding interlayer spacing of $\sim 3.4 \text{ \AA}$. After oxidation of graphite to GO, the peak shifted downward to a lower angle at $2\theta = \sim 11.0^\circ$ with a matching spacing of $\sim 8.0 \text{ \AA}$ which is similar to GO solids reported previously [14,15]. The larger interlayer spacing of GO is due to the large amount of polar groups generated between the layers of graphite during oxidation, in which the oxygen and carbon atoms are covalently bonded, leading to an increase in the graphite's crystal lattice length along axis *c*. The diffraction peak of graphite did not occur in the diffraction spectrogram of GO, indicating that the graphite had been completely oxidized. Raman spectra of graphite and GO are given in Figure 1(b). The bulk graphite shows the two intense bands centered at 1581 cm^{-1} (G band) and 2720 cm^{-1} (2D band). The G band is the response of the in-plane stretching motion of symmetric sp^2 C–C bond. The 2D band is the second order of the D band. A very tiny D band was observed for bulk graphite. This proved the absence of a significant amount of defects in the graphite. In contrast, the ra-

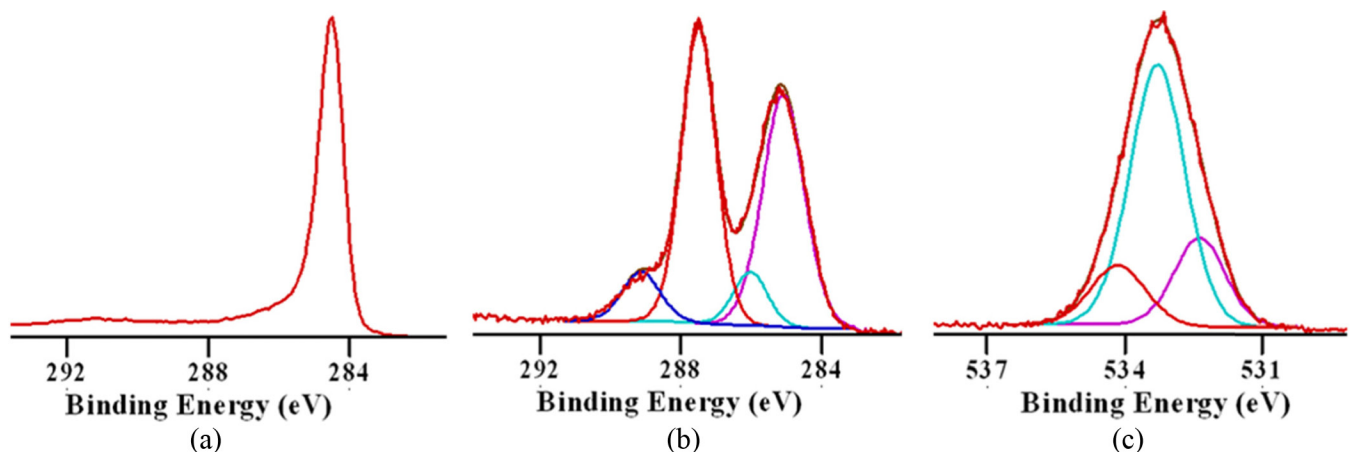


Figure 2. (a) C 1s XPS spectrum of graphite (b) C 1s and (c) O 1s XPS spectra of graphene oxide.

man spectrum of the GO displays an intense D band centred at 1357 cm^{-1} and a G band at 1607 cm^{-1} . The D band arises from the disruption of the symmetrical hexagonal graphitic lattice as a result of internal structural defects, edge defects, and dangling bonds created by the attachment of hydroxyl and epoxide groups on the carbon [16]. D band intensity is directly proportional to the level of defects in the sample and can also be used as a gauge of degree of functionalization when graphene is chemically modified [17]. Chemical and structural changes of graphite upon oxidation were detected from FTIR spectrum of GO [Figure 1(c)]. A broad band at $3000\text{--}3700\text{ cm}^{-1}$ appears in the IR spectrum, which signifies stretching vibration of surface hydroxyls (~ 3400) and water absorption ($\sim 3200\text{ cm}^{-1}$). The peaks are located at ~ 1720

cm^{-1} (C=O stretching) from carbonyl and carboxylic groups, at $\sim 1200\text{ cm}^{-1}$ (C–OH stretching) from carboxylic groups and at $\sim 1050\text{ cm}^{-1}$ (skeletal C–O or C–C stretching) peak from carbonyl, carboxylic and epoxy groups, which confirms the presence of oxygen-containing functional groups [18,19]. The peak at 1620 cm^{-1} can be assigned to the vibrations of the adsorbed water molecules and also the contributions from the skeletal vibrations of un-oxidized graphitic domains [20].

The C1s XPS spectrum of graphite is shown in Figure 2(a). The peak centred at 284.5 eV corresponds to graphitic carbon (non-oxygenated). The atomic composition of GO was obtained from the XPS survey spectrum and revealed the presence of C (66.6 at%) O (30.4 at%) and small amount

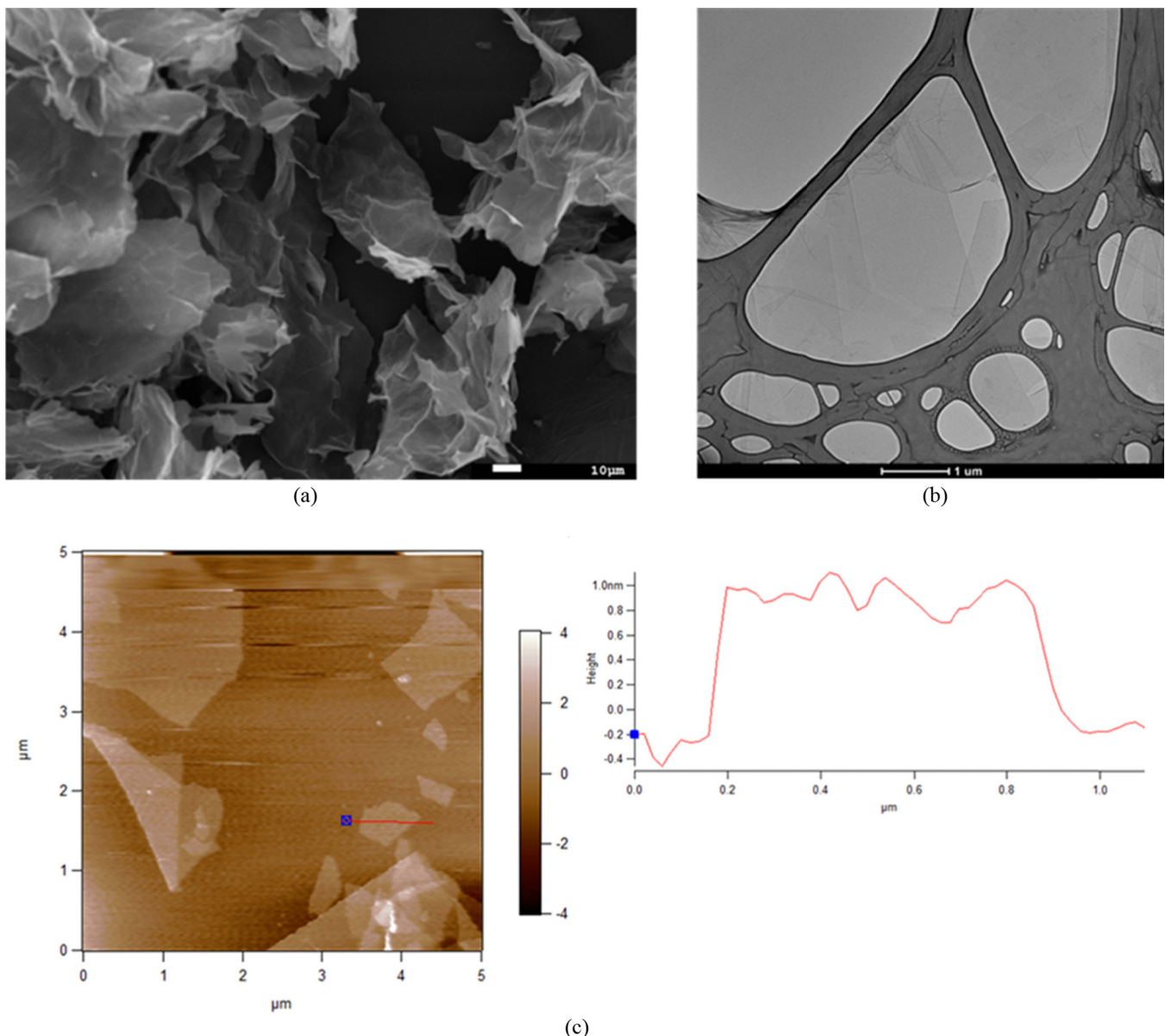


Figure 3. (a) SEM (b) TEM (c) AFM images of graphene oxide.

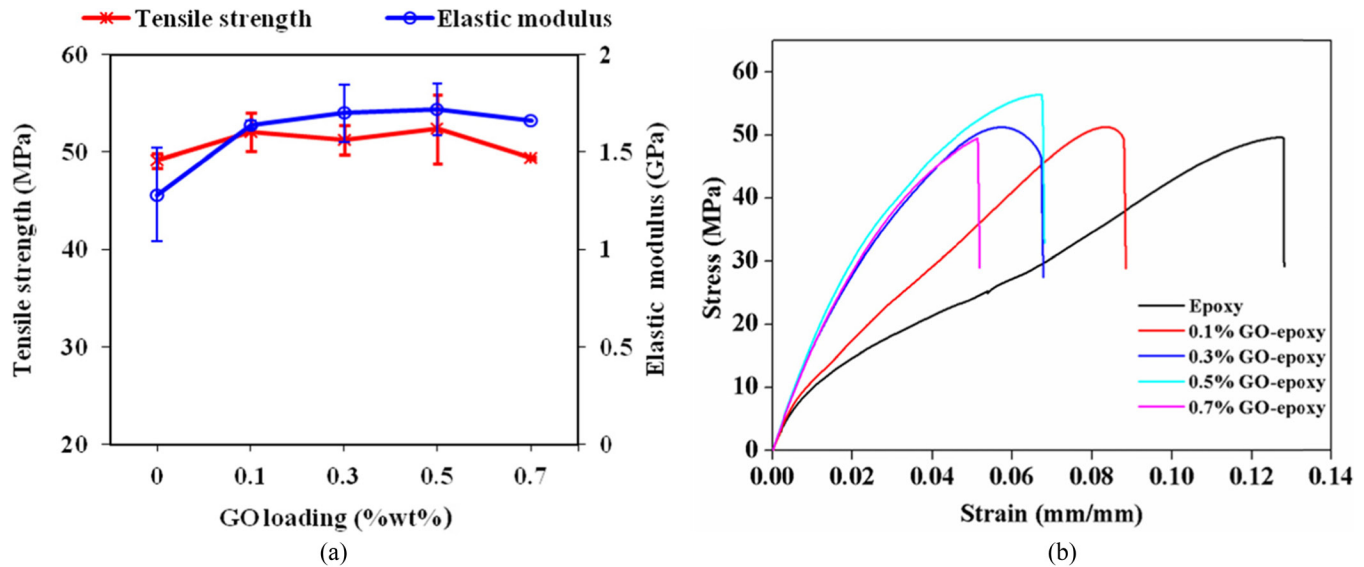


Figure 4. (a) Elastic modulus and tensile strength (b) Tensile stress vs tensile strain curves of graphene oxide-epoxy nanocomposites.

of S, N and P (residual from the acids used for the oxidation process). The chemical composition detected for the GO is very similar to reported data in literature [16,21–23]. The detail spectra C 1s and O 1s spectra of graphene oxide are shown in Figure 2(b) and (c). The C1s XPS data of GO surface clearly displays the presence of four different kinds of carbon atoms such as non-oxygenated carbons (C–C) at 284.7 eV, carbons attached to carboxylic groups (C*–COOH) at 285.8 eV, carbons in carbon-hydroxyl groups (C*–OH) and carbons in epoxy/ether (C*–O) at 287.5 eV, and carboxylate carbons (O–C*=O) at 288.9 eV. The peaks are at 532.4 eV and 533.3 eV in the O1s spectrum of GO [Figure 2(c)] can be assigned to contribution from C=O* and C–O*–C/C–O*–H groups, respectively [16]. The peak at 534.1 eV can be assigned to oxygen from water molecules.

Figure 3(a) illustrates the typical SEM image of GO, indicating randomly aggregated, thin crumpled sheets closely associated with each other which are significantly different from graphite flakes. The platelets have lateral dimensions ranging from several hundred nanometers to several micrometers. The TEM observations further reveal that the GO are likely to be in the form of single or few layer sheets as shown in Figure 3(b). From a tapping mode AFM image of GO on a mica substrate [Figure 3(c)], the average thickness is ~1 nm. This value is very similar to the reported thickness of GO monolayer [24–26]. Compared with the pristine graphene with a thickness of ~0.8 nm [1], the higher thickness of as-made GO is due to the presence of the covalent C–O bonds at both top and bottom surfaces, distorted sp³ carbon lattices and absorbed contaminations [27–29]. All these observations indicate that graphite was completely oxidized and exfoliated to GO sheets upon oxidation and sonication.

3.2. Characterization of Graphene Oxide/Epoxy Nanocomposites

Figure 4(a) shows variation of ultimate tensile strength and elastic modulus of neat epoxy and the nanocomposites with different GO content and Figure 4(b) provides the representative tensile stress-strain curves. From the Figure 4(a), it can be seen that elastic modulus and tensile strength of epoxy matrix increased with GO loading. Elastic modulus and tensile strength of neat epoxy are 1.28 GPa and 49.15 MPa, respectively. At 0.5 wt% GO, the elastic modulus of the nanocomposite was enhanced by ~35% while there was ~7% increase in the ultimate tensile strength. Figure 4(b) shows that as more GO are incorporated, considerably reduced strains at ultimate strength are observed. The decreased tensile strain of nanocomposites with increasing GO content are typical behaviour of composite with enhanced strength and stiffness [30]. It is obvious from the results that GO can significantly improve the tensile strength and stiffness of epoxy at lower filler loading. Improvement can be credited to high elastic modulus and strength of GO [5], better interactions between GO and polymer matrix and uniform dispersion of GO in the epoxy matrix due to abundant functional groups on the GO surface [31]. Further, the wrinkled surface structure of GO may enhance the mechanical interlocking and adhesion of between the epoxy and GO at the filler-matrix interface thus effectively transfer the stress at the interface [32,33].

Figure 5(a) and (b) show the SEM images of cross-section of the tensile fractured surfaces of epoxy and GO/epoxy nanocomposites. However, no significant difference was observed for pristine epoxy matrix and the composites. It was also difficult to observe the distribution of GO in the polymer matrix. This may be by reasons of the use of very

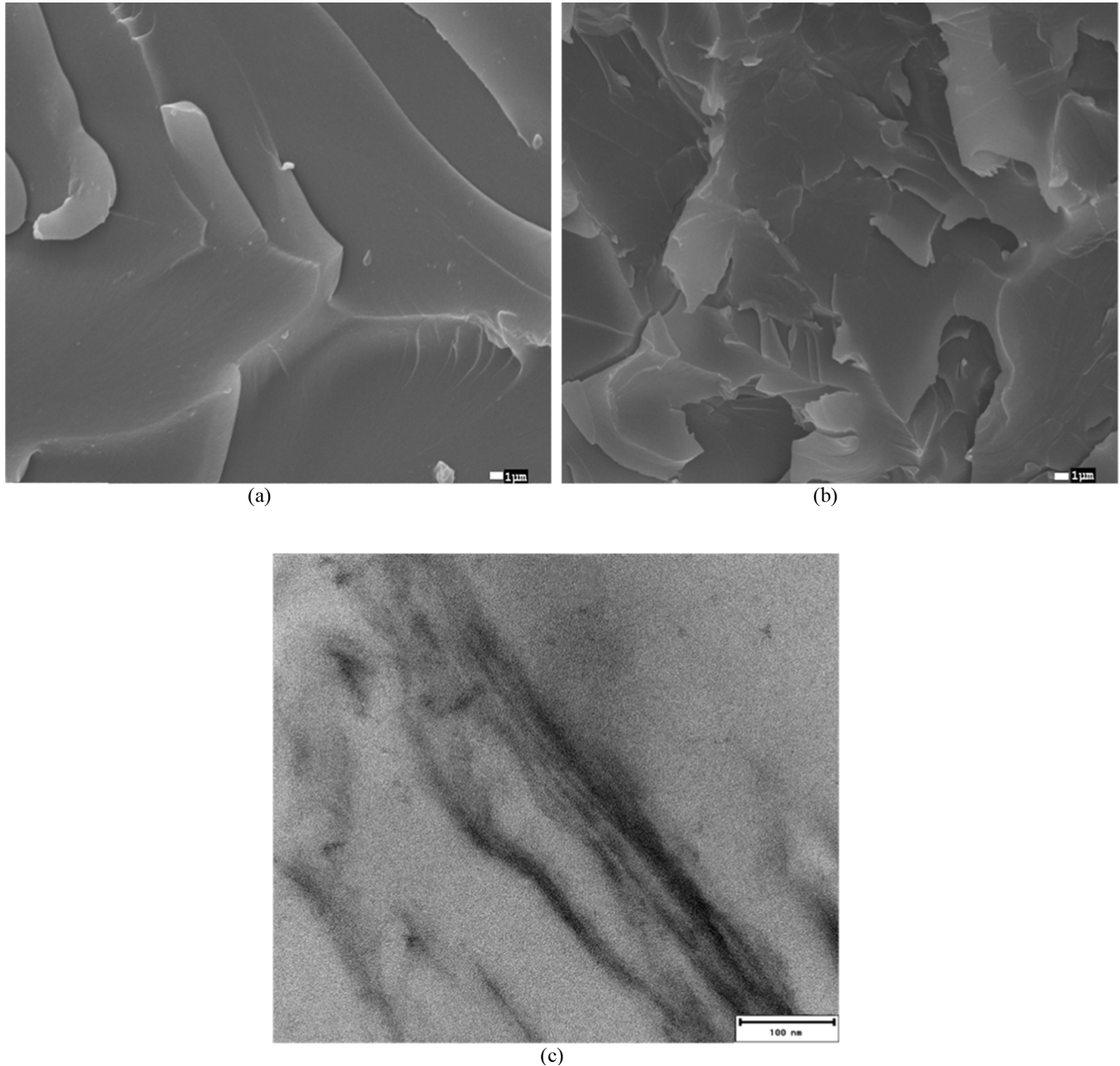


Figure 5. SEM images of tensile fractured surfaces of (a) neat epoxy and (b) 0.7 wt% GO/epoxy nanocomposite, (c) TEM image of 0.7 wt% GO/epoxy nanocomposite.

low content of GO and two-dimensional sheet structure of GO. Then the inner structure of epoxy nanocomposite was examined by TEM [Figure 5(c)] from which we can observe a homogeneous and uniform dispersion of GO. The good dispersion of GO in epoxy matrix is due to the oxygen functional groups in GO which can chemically bonded with epoxy matrix.

Glass transition temperature (T_g) of nanocomposites was obtained by DSC and the values are shown in Table 1. T_g of pure epoxy is approximately 66°C. The T_g of neat epoxy was found to decrease significantly when GO is added to the res-

in and there was ~15°C decrease in the T_g with the addition of 0.5 wt% GO. Generally, the T_g of composites depends on the balance of two effects, influence on reaction conversion and molecular confinement. GO sheets show stiffer modulus than epoxy matrix which could lead to significant confinement on the polymer chains [34]. On the other hand, GO may interfere the epoxy curing reaction. This interference may be arisen due to reaction between curing agent (TETA) and the functional groups of graphene oxide. As a result, the optimized ratio of epoxy and curing agent in curing reaction was impacted. This generally reduces the polymer cross-

Table 1. Glass Transition Temperature of Neat Epoxy and Nanocomposites.

Sample	Glass Transition Temperature, T_g (°C)
Neat epoxy	66.06
0.1% GO-epoxy	52.02
0.3% GO-epoxy	54.35
0.5% GO-epoxy	51.27
0.7% GO-epoxy	50.96

linkage and increase polymer chain mobility. Based on the result, it can be seen that GO significantly obstructs the epoxy curing reaction, leading to positive effect on molecular chain mobility. The less restriction on molecular chain mobility grounds to decrease the T_g [35,36].

4. CONCLUSIONS

Bulk quantity of graphene oxide with ~30% of oxygen atoms was prepared using the modified Hummers method. A series of GO/epoxy nanocomposites was prepared by simple solution mixing technique, varying the amount of GO in the epoxy matrix. The maximum 35% improvement of elastic modulus and 7% improvement of tensile strength were observed for the composite with 0.5 wt % loading of GO. TEM imaging showed the homogeneous dispersion of GO in the epoxy matrix. However, T_g of baseline epoxy considerably decreased with addition of GO. This can be due to incomplete curing of epoxy matrix.

ACKNOWLEDGEMENT

Authors gratefully acknowledge Mr. Marco Notarianni, Queensland university of Technology and Dr. Barry Wood, University of Queensland, Australia for their invaluable help for analysis of TEM and XPS of graphene oxide. We thank Queensland university of Technology for financial support.

REFERENCES

- [1] Novoselov, K. S., Geim, A. K., Morozov, S. V., Jiang, D., Zhang, Y., Dubonos, S. V., Grigorieva, I. V. and Firsov, A. A., "Electric Field Effect in Atomically Thin Carbon Films," *Science*, 306(5696), 666–669 (2004). <http://dx.doi.org/10.1126/science.1102896> PMID:15499015
- [2] Park, S. and Ruoff, R. S., "Chemical methods for the production of graphenes," *Nat Nano*, 4(4), 217–224 (2009). <http://dx.doi.org/10.1038/nnano.2009.58> PMID:19350030
- [3] Singh, V., Joung, D., Zhai, L., Das, S., Khondaker, S. I. and Seal, S., "Graphene based materials: Past, present and future," *Progress in Materials Science*, 56(8), 1178–1271 (2011). <http://dx.doi.org/10.1016/j.pmatsci.2011.03.003>
- [4] Warner, J. H., Schäffel, F., Bachmatiuk, A. and Rummeli, M. H., *Graphene: Fundamentals and emergent applications*, Elsevier, Oxford, UK, 61–127 (2013).
- [5] Suk, J. W., Piner, R. D., An, J. and Ruoff, R. S., "Mechanical Properties of Monolayer Graphene Oxide," *ACS Nano*, 4(11), 6557–6564 (2010). <http://dx.doi.org/10.1021/nn101781v> PMID:20942443
- [6] Wang, Y., Shi, Z., Fang, J., Xu, H. and Yin, J., "Graphene oxide/polybenzimidazole composites fabricated by a solvent-exchange method," *Carbon*, 49(4), 1199–1207 (2011). <http://dx.doi.org/10.1016/j.carbon.2010.11.036>
- [7] Bortz, D. R., Heras, E. G. and Martin-Gullon, I., "Impressive Fatigue Life and Fracture Toughness Improvements in Graphene Oxide/Epoxy Composites," *Macromolecules*, 45(1), 238–245 (2011). <http://dx.doi.org/10.1021/ma201563k>
- [8] Kong, J.-Y., Choi, M.-C., Kim, G. Y., Park, J. J., Selvaraj, M., Han, M. and Ha, C.-S., "Preparation and properties of polyimide/graphene oxide nanocomposite films with Mg ion crosslinker," *European Polymer Journal*, 48(8), 1394–1405 (2012). <http://dx.doi.org/10.1016/j.eurpolymj.2012.05.015>
- [9] Bao, C., Guo, Y., Song, L., Kan, Y., Qian, X. and Hu, Y., "In situ preparation of functionalized graphene oxide/epoxy nanocomposites with effective reinforcements," *Journal of Materials Chemistry*, 21(35), 13290–13298 (2011). <http://dx.doi.org/10.1039/c1jm11434d>
- [10] Cano, M., Khan, U., Sainsbury, T., O'Neill, A., Wang, Z., McGovern, I. T., Maser, W. K., Benito, A. M. and Coleman, J. N., "Improving the mechanical properties of graphene oxide based materials by covalent attachment of polymer chains," *Carbon*, 52(0), 363–371 (2013). <http://dx.doi.org/10.1016/j.carbon.2012.09.046>
- [11] Wang, Y., Shi, Z., Yu, J., Chen, L., Zhu, J. and Hu, Z., "Tailoring the characteristics of graphite oxide nanosheets for the production of high-performance poly(vinyl alcohol) composites," *Carbon*, 50(15), 5525–5536 (2012). <http://dx.doi.org/10.1016/j.carbon.2012.07.042>
- [12] Zhang, H.-B., Zheng, W.-G., Yan, Q., Jiang, Z.-G. and Yu, Z.-Z., "The effect of surface chemistry of graphene on rheological and electrical properties of polymethylmethacrylate composites," *Carbon*, 50(14), 5117–5125 (2012). <http://dx.doi.org/10.1016/j.carbon.2012.06.052>
- [13] Marcano, D. C., Kosynkin, D. V., Berlin, J. M., Sinititskii, A., Sun, Z., Slesarev, A., Alemany, L. B., Lu, W. and Tour, J. M., "Improved Synthesis of Graphene Oxide," *ACS Nano*, 4(8), 4806–4814 (2010). <http://dx.doi.org/10.1021/nn1006368> PMID:20713455
- [14] Liu, F., Song, S., Xue, D. and Zhang, H., "Folded Structured Graphene Paper for High Performance Electrode Materials," *Advanced Materials*, 24(8), 1089–1094 (2012). <http://dx.doi.org/10.1002/adma.201104691> PMID:22271320
- [15] Compton, O. C., Jain, B., Dikin, D. A., Abouimrane, A., Amine, K. and Nguyen, S. T., "Chemically Active Reduced Graphene Oxide with Tunable C/O Ratios," *ACS Nano*, 5(6), 4380–4391 (2011). <http://dx.doi.org/10.1021/nn1030725> PMID:21473647
- [16] Yang, D., Velamakanni, A., Bozkoklu, G., Park, S., Stoller, M., Piner, R. D., Stankovich, S., Jung, I., Field, D. A., Ventrice Jr, C. A. and Ruoff, R. S., "Chemical analysis of graphene oxide films after heat and chemical treatments by X-ray photoelectron and Micro-Raman spectroscopy," *Carbon*, 47(1), 145–152 (2009). <http://dx.doi.org/10.1016/j.carbon.2008.09.045>
- [17] Wall, M., "Raman Spectroscopy Optimizes Graphene Characterization " *Advanced Material and Process*, (April 2012).
- [18] Guo, Y., Sun, X., Liu, Y., Wang, W., Qiu, H. and Gao, J., "One pot preparation of reduced graphene oxide (RGO) or Au (Ag) nanoparticle-RGO hybrids using chitosan as a reducing and stabilizing agent and their use in methanol electrooxidation," *Carbon*, 50(7), 2513–2523 (2012). <http://dx.doi.org/10.1016/j.carbon.2012.01.074>
- [19] Shen, J., Li, T., Long, Y., Shi, M., Li, N. and Ye, M., "One-step solid state preparation of reduced graphene oxide," *Carbon*, 50(6), 2134–2140 (2012). <http://dx.doi.org/10.1016/j.carbon.2012.01.019>
- [20] Si, Y. and Samulski, E. T., "Synthesis of Water Soluble Graphene," *Nano Letters*, 8(6), 1679–1682 (2008). <http://dx.doi.org/10.1021/nl080604h> PMID:18498200
- [21] Becerril, H. A., Mao, J., Liu, Z., Stoltenberg, R. M., Bao, Z. and Chen, Y., "Evaluation of Solution-Processed Reduced Graphene Oxide Films as Transparent Conductors," *ACS Nano*, 2(3), 463–470 (2008). <http://dx.doi.org/10.1021/nn700375n> PMID:19206571

- [22] Fan, X., Peng, W., Li, Y., Li, X., Wang, S., Zhang, G. and Zhang, F., "Deoxygenation of Exfoliated Graphite Oxide under Alkaline Conditions: A Green Route to Graphene Preparation," *Advanced Materials*, 20(23), 4490–4493 (2008). <http://dx.doi.org/10.1002/adma.200801306>
- [23] Murugan, A. V., Muraliganth, T. and Manthiram, A., "Rapid, Facile Microwave-Solvothermal Synthesis of Graphene Nanosheets and Their Polyaniline Nanocomposites for Energy Storage," *Chemistry of Materials*, 21(21), 5004–5006 (2009). <http://dx.doi.org/10.1021/cm902413c>
- [24] Glover, A. J., Adamson, D. H. and Schniepp, H. C., "Charge-Driven Selective Adsorption of Sodium Dodecyl Sulfate on Graphene Oxide Visualized by Atomic Force Microscopy," *The Journal of Physical Chemistry C*, 116(37), 20080–20085 (2012). <http://dx.doi.org/10.1021/jp305717v>
- [25] Imperiali, L., Liao, K.-H., Clasen, C., Fransaer, J., Macosko, C. W. and Vermant, J., "Interfacial Rheology and Structure of Tiled Graphene Oxide Sheets," *Langmuir*, 28(21), 7990–8000 (2012). <http://dx.doi.org/10.1021/la300597n> PMID:22432592
- [26] Sun, Z., Masa, J., Liu, Z., Schuhmann, W. and Muhler, M., "Highly Concentrated Aqueous Dispersions of Graphene Exfoliated by Sodium Taurodeoxycholate: Dispersion Behavior and Potential Application as a Catalyst Support for the Oxygen-Reduction Reaction," *Chemistry—A European Journal*, 18(22), 6972–6978 (2012). PMID:22504902
- [27] Stankovich, S., Dikin, D. A., Piner, R. D., Kohlhaas, K. A., Kleinhammes, A., Jia, Y., Wu, Y., Nguyen, S. T. and Ruoff, R. S., "Synthesis of graphene-based nanosheets via chemical reduction of exfoliated graphite oxide," *Carbon*, 45(7), 1558–1565 (2007). <http://dx.doi.org/10.1016/j.carbon.2007.02.034>
- [28] Mkhoyan, K. A., Contryman, A. W., Silcox, J., Stewart, D. A., Eda, G., Mattevi, C., Miller, S. and Chhowalla, M., "Atomic and Electronic Structure of Graphene-Oxide," *Nano Letters*, 9(3), 1058–1063 (2009). <http://dx.doi.org/10.1021/nl8034256> PMID:19199476
- [29] Cheng, M., Yang, R., Zhang, L., Shi, Z., Yang, W., Wang, D., Xie, G., Shi, D. and Zhang, G., "Restoration of graphene from graphene oxide by defect repair," *Carbon*, 50(7), 2581–2587 (2012). <http://dx.doi.org/10.1016/j.carbon.2012.02.016>
- [30] Lee, J. K., Song, S. and Kim, B., "Functionalized graphene sheets-epoxy based nanocomposite for cryotank composite application," *Polymer Composites*, 33(8), 1263–1273 (2012). <http://dx.doi.org/10.1002/pc.22251>
- [31] Du, J. and Cheng, H.-M., "The Fabrication, Properties, and Uses of Graphene/Polymer Composites," *Macromolecular Chemistry and Physics*, 213(10–11), 1060–1077 (2012). <http://dx.doi.org/10.1002/macp.201200029>
- [32] Rafiee, M. A., Rafiee, J., Wang, Z., Song, H., Yu, Z.-Z. and Koratkar, N., "Enhanced Mechanical Properties of Nanocomposites at Low Graphene Content," *ACS Nano*, 3(12), 3884–3890 (2009). <http://dx.doi.org/10.1021/nn9010472> PMID:19957928
- [33] Ramanathan, T., Abdala, A. A., Stankovich, S., Dikin, D. A., Herrera Alonso, M., Piner, R. D., Adamson, D. H., Schniepp, H. C., Chen, X., Ruoff, R. S., Nguyen, S. T., Aksay, I. A., Prud'Homme, R. K. and Brinson, L. C., "Functionalized graphene sheets for polymer nanocomposites," *Nat Nano*, 3(6), 327–331 (2008). <http://dx.doi.org/10.1038/nnano.2008.96> PMID:18654541
- [34] Wang, S., Tambraparni, M., Qiu, J., Tipton, J. and Dean, D., "Thermal Expansion of Graphene Composites," *Macromolecules*, 42(14), 5251–5255 (2009). <http://dx.doi.org/10.1021/ma900631c>
- [35] Jingjing, Q., Chuck, Z., Ben, W. and Richard, L., "Carbon nanotube integrated multifunctional multiscale composites," *Nanotechnology*, 18(27), 275708 (2007). <http://dx.doi.org/10.1088/0957-4484/18/27/275708>
- [36] Liu, Q., Zhou, X., Fan, X., Zhu, C., Yao, X. and Liu, Z., "Mechanical and Thermal Properties of Epoxy Resin Nanocomposites Reinforced with Graphene Oxide," *Polymer-Plastics Technology and Engineering*, 51(3), 251–256 (2012). <http://dx.doi.org/10.1080/03602559.2011.625381>



Dynamic Behaviour of Debonded GFRP Composite Beams

INDUNIL JAYATILAKE*, WARNA KARUNASENA and WEENA LOKUGE

Centre of Excellence in Engineered Fibre Composites (CEEFC), Faculty of Engineering and Surveying, University of Southern Queensland, Toowoomba, Queensland 4350, Australia

KEYWORDS

Dynamic behaviour
Fibre composites
Debonding
Natural frequency
Vibration modes

ABSTRACT

A new generation composite sandwich made up of glass fibre reinforced polymer (GFRP) skins and high strength phenolic core material has been developed in Australia. Sandwich structure relies on the adhesive bond between the face-sheet and core for its overall stability and consistency. Although perfect bond between the skin and the core is a common assumption, an important issue that needs to be considered in using a composite beam or slab is the development of debonding between the skin and the core, which is a predominant failure mode of these sandwiches. Debonding can happen during fabrication or under service conditions that leads to changes in free vibration behaviour which in turn can result in resonance. Therefore, it is important to make accurate predictions of changes in natural frequencies in such structural elements. This paper investigates the influence of debonding on dynamic behaviour of sandwich beams of different debonding sizes and end conditions. Numerical model is developed with Strand7 finite element software, and the developed model is used for 3D finite element simulation. Free vibration behaviour reported in the literature for composite beams will first be used to compare the analytical results with the fully bonded and debonded beams. Study is extended to depict the effect of debonding on free vibration behaviour of novel composite beams. It is observed that the decrease in natural frequency with the increase in the extent of debonding is more dependent on the width of debonding across the beam than the length along the beam. The end conditions of the beam are also a governing factor dictating which modes are more affected. It is also perceived that full width debonding leads to increased participation of twisting modes in comparison to half-width debonding in clamped-clamped end condition.

© 2013 DEStech Publications, Inc. All rights reserved.

1. INTRODUCTION

The past two decades have witnessed a substantial increase in the demand and use of fibre reinforced composites for structural applications, specifically in the construction of large-scale structures such as fibre composite bridges, due to its high strength, durability and reduced weight. Although the aircraft industry was the first to use fibre composites, now they are increasingly used in civil engineering applications such as flooring, decking, platforms, cladding and roofs. While sandwich composite construction has some

great benefits, the behaviour of sandwich structures containing damage is much more complex and one of the major factors limiting the optimum usage of sandwich structures.

Sandwich structure relies on the adhesive bond between the face-sheet and core for its overall stability and consistency. A region where there is no bond is called a debond. Although perfect bond between the skin and the core is a common assumption, an important issue that needs to be considered in using a composite panel is the development of debonding between the skin and the core. Debonding may arise during fabrication or under service conditions, which may cause changes to the free vibration behaviour in addition to the strength degradation.

*Corresponding author. Tel: 0734704454; Email: Indunil.Jayatilake@usq.edu.au

In the Australian context, there is an ever increasing demand for composites as an alternative to Australian hardwood that have been used for a wide range of applications including piles, railway sleepers and bridge components, due to the increasing cost, shortage and decline in quality of hardwood components.

A new generation composite sandwich made up of glass fibre reinforced polymer (GFRP) skins and high strength phenolic core material have been developed in Australia. The outstanding features of this sandwich material including high strength to weight ratio, good thermal insulation and termite resistance offer this composite panel a wide range of applications in Australian construction industry as structural elements such as beams, slabs, bridge decks and railway sleepers. The Centre of Excellence in Engineered Fibre Composites (CEEFC) at the University of Southern Queensland (USQ) has played a leading role in these developments. According to Aravinthan and Manalo [1], while fibre composites are reaching a point of commercial reality in the Australian construction industry, challenges faced by the structural designer includes, the understanding of the behaviour of the fibre composite materials, its failure modes and applying available design guidelines to the local needs.

The dynamic behaviour of composite structures is an important technological area to be investigated and understood if these materials are to be used efficiently. Although the use of fibre composite and sandwich structures has increased tremendously, there are still several aspects concerning the dynamic behaviour of these materials that are not clearly understood. Free vibration behaviour, and forced vibration behaviour due to probable dynamic loadings of these sandwiches are considered as key aspects to be considered in this context. Although perfect bond between the skin and the core is a common assumption, an important issue that needs to be considered in using a composite beam or slab is the development of debonding between the skin and the core, which is a predominant failure mode of these sandwiches.

According to Burlayenko and Sadowski [2], in addition to reducing the overall stiffness and strength and affecting the dynamic responses, debonding can also propagate and trigger new damage modes such as face sheet wrinkling, face sheet delamination and core shear cracks, as shown in Figure 1.

Although much research has been carried out to investigate dynamic behaviour of fully bonded composites, research on the dynamic behaviour of debonded composites is scarce. Further research is therefore needed into investigation of the dynamic behaviour of debonded composite structural elements to gain wider acceptance of composites particularly by the Australian industry, and more importantly by the wider structural composite field around the globe.

According to Burlayenko & Sadowski [2], although several studies have been reported in the literature on free vibration behaviour of delaminated plates, only few investigations have been conducted on effects of debonding on vibration characteristics. As the debonding of skin from the core in a composite sandwich beam is very similar to delamination in a laminated composite structure, a comprehensive review of literature in the area of free vibration behaviour of delaminated composites is presented.

Kulkarni and Frederick [3] were among the first to examine the problem of delamination in laminated composite structures, and in their study the effect of delamination was considered as a reduction in bending rigidity. However later studies revealed that such modelling overestimates the reduction in bending stiffness due to delamination and hence gives erroneous results [4].

The free flexural vibration of an isotropic beam containing a full width delamination has been studied by several researchers using analytical, experimental and numerical methods in the past as detailed below. Wang *et al.* [5] presented an analytical model, referred to in the literature as 'free model' or 'unconstrained model', consisting of four separate Euler-Bernoulli beam segments joined together

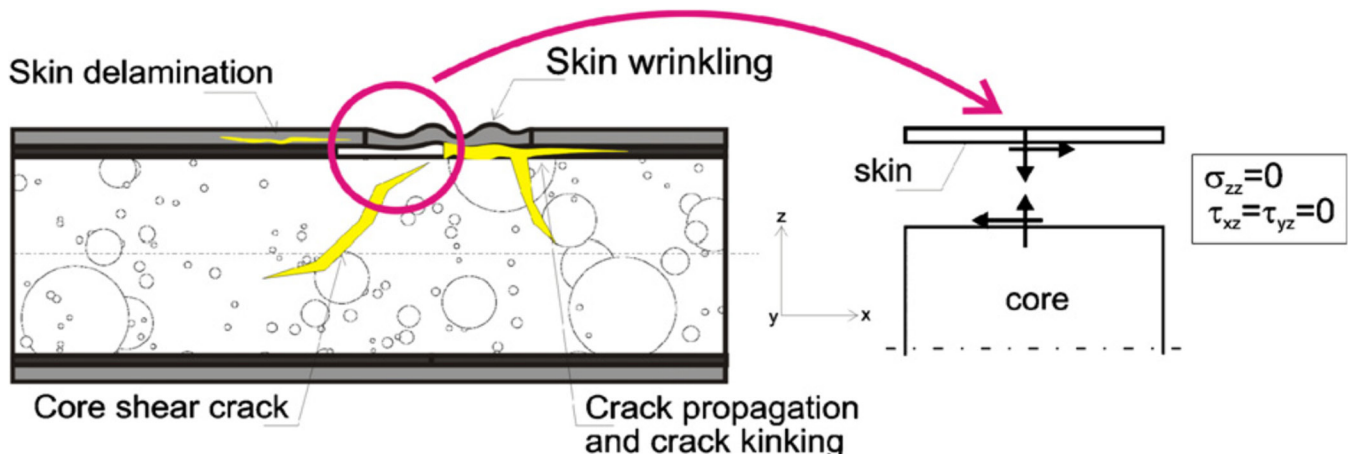


Figure 1. Scheme of a section of a debonded sandwich plate [2].

with appropriate boundary and continuity conditions to get the response of the beam. In their model, it was assumed that delaminated layers deform freely and have different transverse deformations. Although their numerical results were in reasonable agreement with experimental results, they included physically unreal overlapping at the delamination. Later, Mujumdar and Suryanarayan [4] presented 'the constrained model', which is also referred to as 'with-contact model' or 'contact model' in the literature. They did an analytical and experimental study on vibration characteristics of delaminated beams, and assumed that delaminated segments of the beam are constrained to have transverse displacements along the whole length of the beam but are free to slide over each other. Their analytical results were in excellent agreement with experimental results, and it was revealed that the contact model is simple and accurate for analysing vibration characteristics of delaminated beams. Similar analytical model was proposed by Tracey and Pardo [6] to study the effects of delamination. The model proposed by Mujumdar and Suryanarayan [4] was extended by Grouve *et al.* [7] for anisotropic laminated composite beams, to study influence of delamination on the resonance frequencies. Duggan and Ochoa [8] suggested that the natural frequencies are sensitive to the size, location, and shape of delamination in structural components. The contact model was later extended by Hu and Hwu [9] for sandwich beams by including the effects of transverse shear deformations and rotary inertia, and by Shu and Fan [10] for bi-material beams. The models discussed so far, have been adapted by many researchers in different forms to study the behaviour of delaminated beams.

According to Karunasena [11], Modeling and detection of delaminations in composites plates has been studied by researchers mainly with classical lamination theory and first order shear deformation theory (Mindlin Theory). Ju *et al.* [12] carried out a 2D finite element analysis based on the Mindlin theory to investigate the free vibration behaviour of delaminated composite plates. They found that mode shapes are not significantly affected but delamination effects on natural frequencies are mode dependent and some frequencies may be significantly affected. Qiao *et al.* [13] used ANSYS finite element (FE) software to study the dynamic behaviour of delaminated composite beams. They used bilinear contact elements with tension only option for modelling the delamination contact conditions. Chattopadhyay and Gu [14] developed a refined higher order theory (HOT) which was shown to be accurate for delamination modelling in moderately thick composite plates. Later, Chattopadhyay *et al.* [15] further extended this theory where HOT results were compared with experimental results and 3D finite element results using NASTRAN software package. Kim *et al.* [16,17] presented an improved layerwise theory for dynamic analysis of delaminated composites. In their analysis, they used delaminated elements with additional nodal unknowns to model delamination effect. A (3D) FE method to analyse

the dynamic behaviour of delaminated composite plates was presented by Tenek *et al.* [18]. He studied the dynamic behaviour of delaminated composite plates using a 3D finite element method by assuming that the gap between delaminated layers is infinitely small. Krueger and Shell [19] presented a 3D shell modelling technique using ABAQUS finite element software package for analysis of delaminated composite plates. Yam *et al.* [20] proposed a 3D finite element analysis utilizing virtual elements in the region of delamination to prevent element penetration.

Burliayenko and Sadowski [2] investigated influence of debonding on free vibration behaviour of foam and honeycomb cored sandwich plates using finite element code ABAQUS. They found that core types of the sandwich plates strongly affect their dynamic response. Later the same authors [21] reported their findings on dynamic characteristics of honeycomb and PVC foam core sandwich plates containing skin/core debonding by finite element modelling with ABAQUS, and discovered that natural frequencies are poorly sensitive to the number of debonding zones. Newly the same two authors [22] developed a finite element model for analyzing the dynamic response of sandwich plates with partially damaged face sheet and core using three-dimensional finite element model with ABAQUS. It was revealed from the study that, for an accurate simulation of dynamics of debonded sandwich plates, the contact phenomenon within the debonded region need be taken into account.

Generally it was observed that the majority of research carried out has been concerned with delamination of laminated structures whereas skin-core debonding in a single layer beam has received relatively minor attention. This paper reports dynamic analyses of debonded GFRP composite beams using Strand7 finite element code. The effects of debonding on the free vibration characteristics and mode shapes are investigated. This study aims at developing a deeper understanding of the damage behaviour and change in dynamic characteristics of the novel GFRP sandwich beams with regard to debonding.

2. METHODOLOGY

The finite element method (FEM) is today the most powerful numerical tool available for the analysis of structures [23]. Finite element method involves dividing the structure into an equivalent system of finite elements with associated nodes, selecting the most appropriate element type to model closely the actual physical behavior, formulating the equations for each finite element and combining them to obtain the solution of the whole structure [24]. The computer program employed in this research to model, analyze and investigate the dynamic response of debonded composites is the finite element software Strand7. Strand7 is a software package based on the finite element method, and it offers

a visual environment for applying the method to real world engineering problems [23].

2.1. Development of the Model

Dynamic analysis of three dimensional models of structures enables more realistic assessment of their free vibration as well as forced vibration behaviour. Finite element method involves dividing the structure into an equivalent system of finite elements with associated nodes, selecting the most appropriate element type to model closely the actual physical behavior, formulating the equations for each finite element and combining them to obtain the solution of the whole structure [24]. Numerical simulations are carried out using FE code Strand7, using 3D finite element models of the structures. Before the simulations are done, it is needed to develop the numerical model, and then to validate the model with published results for a known problem for the verification of the developed model used in the analyses.

Linear elastic orthotropic top and bottom skins are modelled using 4-noded rectangular (Quad4) plate elements. The plate element mesh for each skin lies at the horizontal plane at the mid-thickness level of the respective skin. Core is modelled using linear elastic orthotropic 3D brick elements (Hexa8). These elements take care of any shear deformations happening in the thick core. Core 3D FE mesh is generated by extruding the Quad4 plate element mesh using the 'extrude' command in strand7. This ensures that a vertical line through corresponding plate nodes in the top and bottom skins will pass through corresponding brick nodes in the core. The structural integrity between top skin and core is assured by connecting plate nodes with corresponding brick nodes at the top surface level of the core through vertical 'rigid link' elements. Rigid link provides restraints to the nodal rotations, in addition to the translational displacements (Strand7 2010).

According to Mujumdar and Suryanarayan [4], in the analysis of dynamics of delaminated beams, 'free model' is of limited significance, and 'contact model' is simple and accurate. Hence master slave links are used in the finite element model to allow for sliding between interfaces of skin and core in the horizontal directions while keeping skins in contact with the

core in the vertical direction to effectively simulate a debonded beam according to 'contact model'. After the FE model has been created, the appropriate eigenvalue problem can be solved to obtain natural frequencies and corresponding mode shapes. As usual in the conventional finite element method, more elements will ensure better convergence and, therefore, appropriate numerical studies are carried out to get a reasonably converged solution by refining the mesh size.

Assumptions made in the FE simulation:

1. Debonding is assumed to be an artificial flaw of zero thickness, embedded between top skin and core.
2. It is assumed that debonding exists before vibration starts and stays constant without propagation during the period of vibration
3. Debonded surfaces (of skin and core) are assumed to be in contact vertically but can slide in the horizontal plane (similar to contact or constrained model).

The mesh size was suitably refined to get the required convergence, to obtain natural frequencies as accurately as possible with the minimum number of elements, to save computational effort. The finally established Finite element mesh consists of 11979 nodes with 1920 plates (8×120 in each of the skins), 7680 bricks ($8 \times 8 \times 120$ in the core) and 2178 links ($2 \times 9 \times 121$ from plate nodes to top and bottom surface nodes in the core).

2.2. Validation of the Model

Initially, the numerical model is verified by comparing model results with published results for a similar scenario. Subsequently, numerical analyses were carried out to obtain natural frequencies and mode shapes of the new generation sandwich composite beams by varying the parameters accordingly.

The links for the sandwich beams are of length $h_{st}/2$ where h_{st} is the thickness of the top skin as shown in Figure 2. These rigid links used for the fully bonded regions ensure that there is no gap or sliding between the top skin and the core. In a similar manner, bottom skin is connected

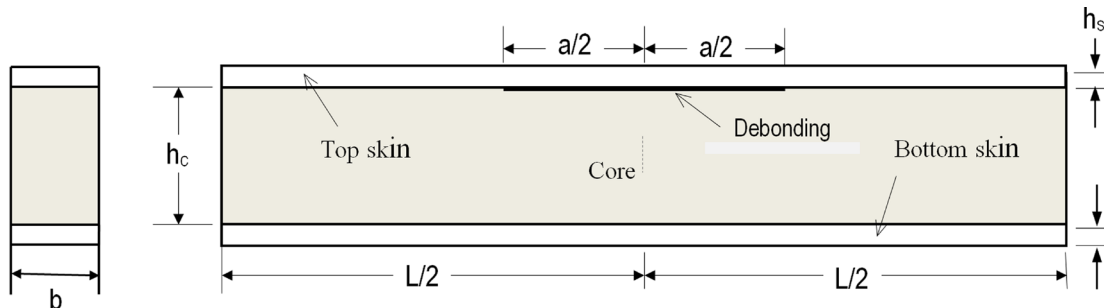


Figure 2. Longitudinal section of the sandwich beam.

to the bottom surface of the core using rigid links of length $h_{sb}/2$ where h_{sb} is the thickness of the bottom skin.

The FE model for the debonded beam is obtained by simply converting the rigid links within the debonded region to 'master slave links' in Strand7 with appropriate degrees of freedoms. A master-slave link defines relations between two nodes so that the displacement of the selected components will be of the same magnitude [23].

The natural frequencies from the proposed model for a foam core sandwich beam are obtained and compared with results reported by Burlayenko and Sadowski [21] and Schwarts *et al.* [25]. Figure 2 shows longitudinal and cross sections of the beam.

The dimensions of the beam used in the verification are,

$$L = 300 \text{ mm}, b = 20 \text{ mm}, a = 20 \text{ mm} \\ h_c = 19.05 \text{ mm}, h_{sb} = 1 \text{ mm} \text{ and } h_{st} = 0.5 \text{ mm}$$

Natural frequencies of intact and debonded beams had been obtained by Burlayenko and Sadowski [21] using Abaqus FE code and by Schwarts *et al.* [25] using a higher order analytical approach. Table 1 gives material properties of the foam core sandwich beam.

3. RESULTS AND DISCUSSION

A comparison of the numerical results of the first five bending natural frequencies from the proposed study with those from literature [21,25] is presented in Table 2 and Table 3. Table 2 gives results for the intact or fully bonded plate whereas Table 3 is for the debonded beam.

It can be clearly seen that the presented results from Strand7 show a good agreement with the results reported in the literature.

3.1. Free Vibration Analysis for the Debonded Novel Composite Sandwich Beams

Free vibration frequencies for the first five modes for the novel composite sandwich beam with full width, half width and various lengths of debonding along the length of the beam are presented graphically in this section. In addition, mode shapes were compared for prominent cases. Three boundary conditions, namely, both ends simply supported

Table 1. Material Properties of Foam Core Sandwich Beam (validation of the model for beams).

Property	Skins	Core
Type	Isotropic	Isotropic
Young's modulus E (MPa)	36000	50
Poisson's ratio, ν	0.3	0.19
Density ρ (kg/m ³)	4400	52

Table 2. First Five Bending Frequencies (Hz) of the Intact Foam Core Sandwich Beam.

Mode Number	ABAQUS [21]	ANSYS [25]	Modified Galerkin Method [25]	Present Analysis with Strand7
1	293.46	290.76	289.18	293.52
2	707.09	710.67	708.29	722.96
3	1106.70	1117.70	1114.24	1139.51
4	1495.80	1515.30	1511.14	1545.91
5	1818.70	1907.09	1902.25	1863.62

(S-S), clamped-clamped (C-C) and clamped-free (C-F) are used in the analysis. The relevant dimensions for the novel composite sandwich beam are (Figure 2):

$$L = 300 \text{ mm}, b = 20 \text{ mm}, h_c = 16 \text{ mm} \text{ and } h_{sb} = h_{st} = 2 \text{ mm}$$

Debonding length 'a' varies from 30 mm to 270 mm in steps of 30 mm.

The debonding is located centrally along the length of the beam and extends through the full width of the beam for case 1, and only middle half width for case 2. Each beam presented here is a new generation sandwich composite structure mentioned in the introduction of this paper and consists of a rigid core bonded to the top and bottom glass fibre composite skins. The effective mechanical properties used in this study for the fibre composite skin and the core material of the sandwich beam are listed in Table 4. In the analysis, the skin is assumed as orthotropic while the core is assumed as an isotropic material.

A typical 3D finite element model created with Strand7 for the beams with C-C end condition is shown in Figure 3.

The frequency variation with the debond length for first five vibration modes are presented graphically for simply supported (S-S), clamped-clamped (C-C) and clamped-free (C-F) end conditions in Figures 4, 5 and 6 respectively.

Table 3. First Five Bending Frequencies (Hz) of the Debonded Foam Core Sandwich Beam.

Mode	ABAQUS [21]	Present Analysis with Strand7
B1	293.07	293.52
L1	433.67	360.81
T1	— ^b	540.79
B2	— ^b	710.75
B3	1093.2	1139.31
T2		1146.32
T3	— ^b	1394.31
B4	— ^b	1520.84
B5	1769.9	1861.72
B6	1948.35	1948.35

^b – Not reported in reference [21].

B – Bending mode; L – Lateral mode; and T – Twisting mode

Table 4. Effective Mechanical Properties for the GFRP Composite Skin and Core.

Property	Skins	Core
Young's modulus along long direction (MPa)	15380	1150
Young's modulus in transverse direction (MPa)	12631	1150
Poisson's ratio	0.25	0.30
Density (kg/m ³)	1366	855

A general reflection through all these variations is that the extent of natural frequency variation with respect to debonding length increases with the order of the natural frequency, giving the least variation for the first frequency.

Another interesting observation is that the change in frequency with change in debonding length is much more significant for all five free vibration frequencies for the full width debonding when compared to half width debonding. This is true for all three end conditions, the change in frequency increasing with the order of the frequency, giving

highest frequency variation for the 5th natural frequency, as clearly seen from Figures 4, 5 and 6.

Frequency results of first three frequencies are presented in a normalized form (Figure 7) for full width debonding with regard to the three end conditions. In the three graphs ω_0 is the frequency of the fully bonded beam for the corresponding mode. It is observed from the comparison of frequency variations for the three end conditions that, first natural frequency has the least effect on debonding for the case of full width debonding shown in Figure 7. It is fascinating to note from Figure 7 that debonding does not have a significant effect on the first frequency when debonding length, a/L , is less than 0.3 for all three end conditions considered in the analysis.

It is interesting to compare some noticeable mode shapes of half width debonding and full width debonding in three end conditions considered in the simulation and analyses. One such comparison is illustrated in Figure 8 for the three end conditions of the beam for full width and half width debonding having 30 mm debond length. It is fascinating to

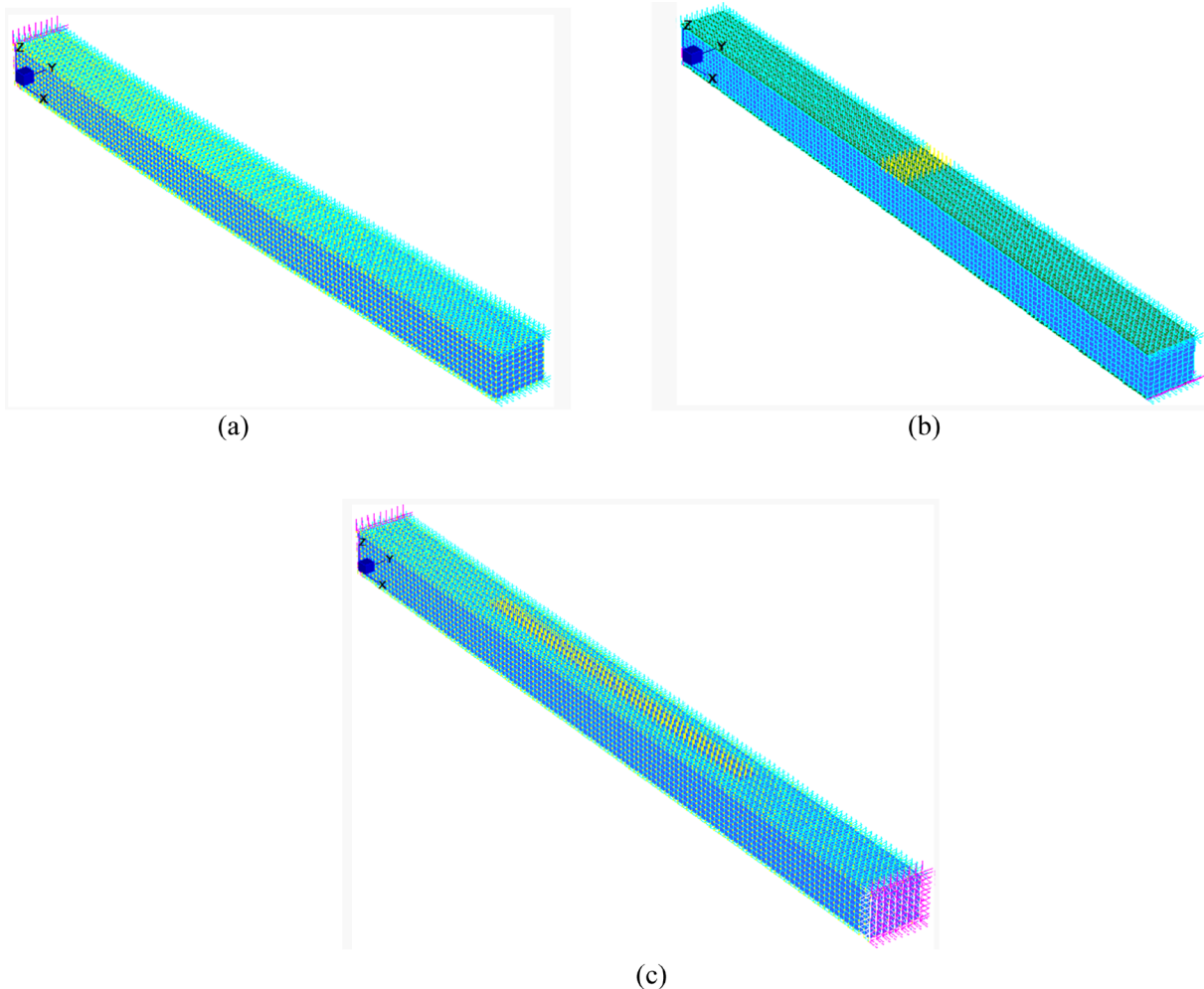


Figure 3. Typical 3D Finite element models of (a) C-F beam (fully bonded), (b) S-S beam 30 mm debond length (full width debonding) and (c) C-C beam 150 mm debond length (half width debonding) beams with Strand7.

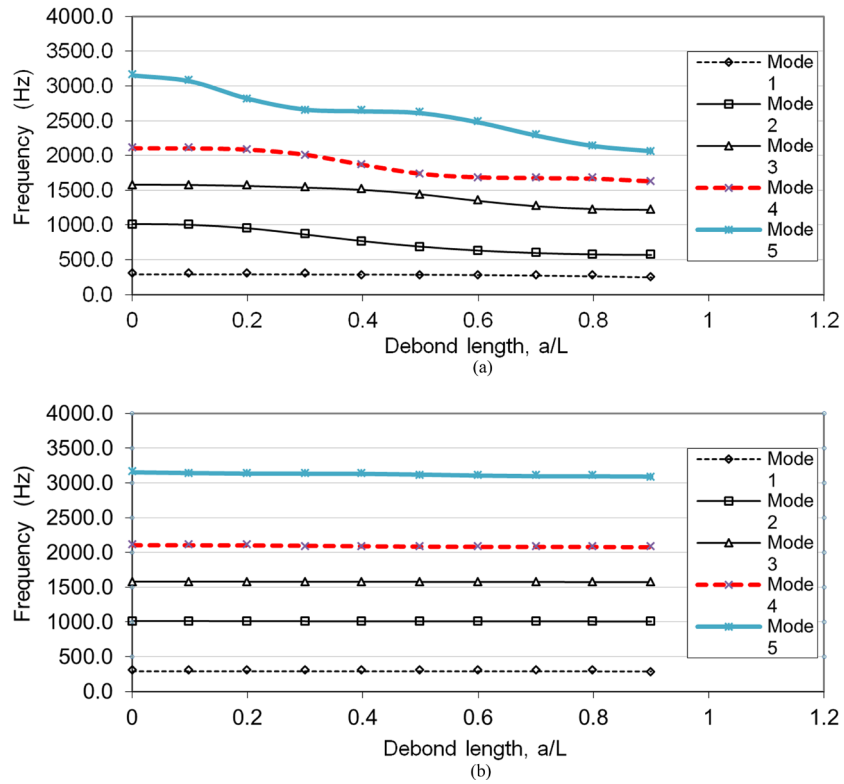


Figure 4. Comparison of natural frequency variation with debonding length for, (a) simply supported beam (full-width debonding) and (b) simply supported beam (half-width debonding) debonding in the simply supported beam.

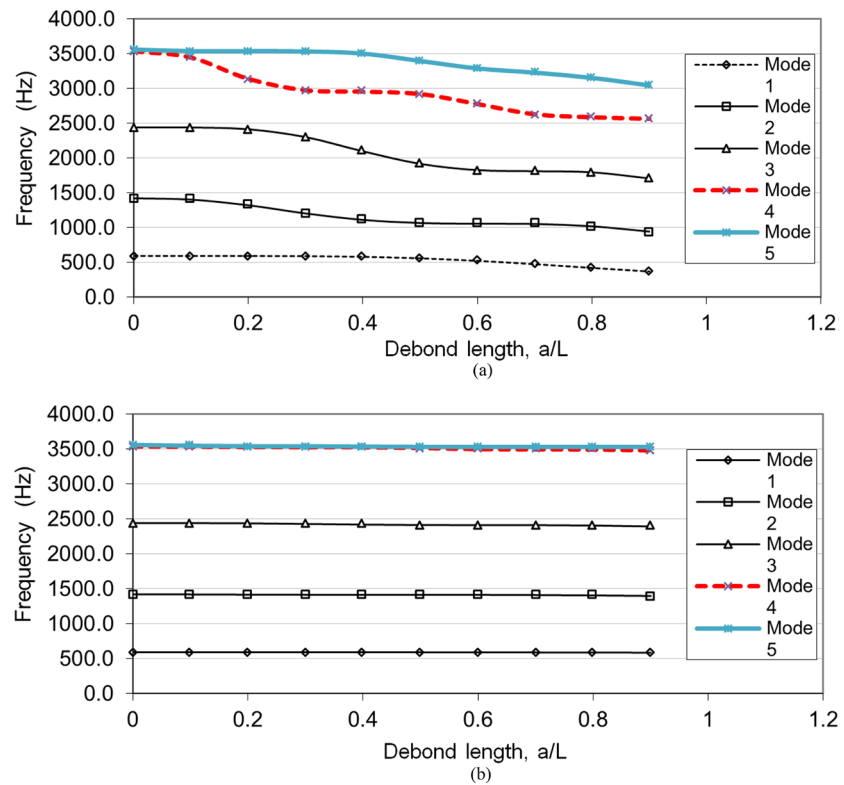


Figure 5. Comparison of natural frequency variation with debonding length for, (a) clamped-clamped beam (full width debonding) and (b) clamped-clamped beam (half width debonding) debonding in the clamped-clamped beam.

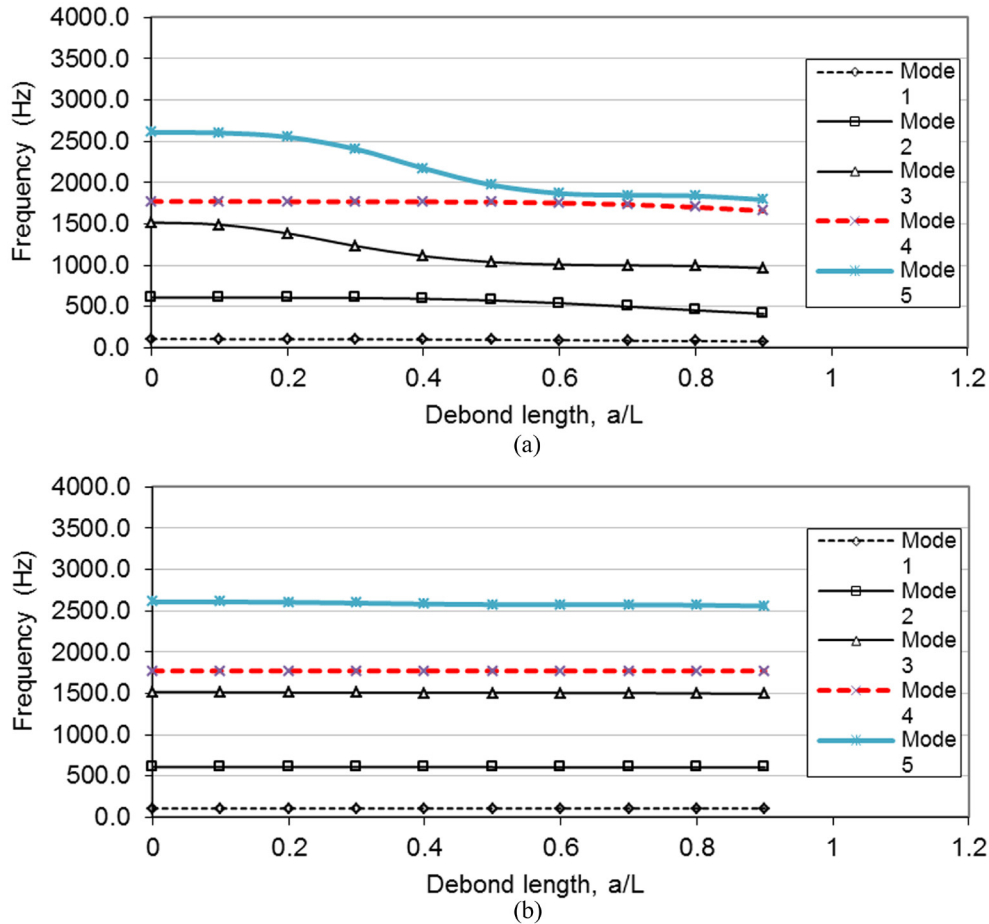


Figure 6. Comparison of natural frequency variation with debonding length for, (a) clamped-free beam (full-width debonding) and (b) clamped-free beam (half-width debonding) debonding in the clamped-free beam.

perceive here that bending modes prevalent in 3rd mode in half width debond case are replaced by twisting modes, in the case of full width debond, only for the C-C end condition. This is attributed to increased participation of rotational or twisting modes in full width debonding case compared to half width debonding situation for the C-C case. This reveals that full width debonding leads to increased participation of twisting modes, compared to half width debonding, specifically for clamped-clamped end condition. Such transition is

not seen in the cases of S-S beam or C-F beam as illustrated in Figure 8.

Similar transition from bending mode to twisting mode was observed in the comparison of mode 6 as well, only in the case of C-C beam (Figure 9).

It is also perceived that the maximum reduction in natural frequencies is close to but always below 50% of virgin beam frequencies for all three end conditions, namely simply supported, clamped-clamped and clamped-free end conditions

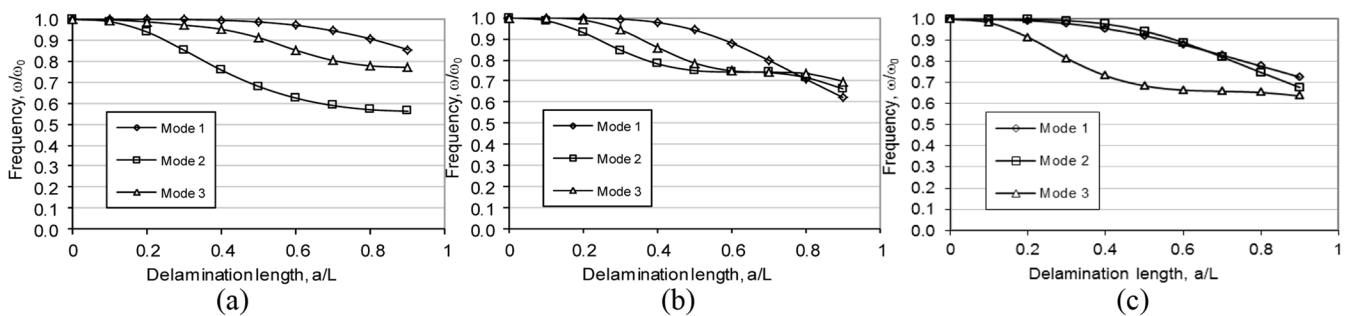


Figure 7. Comparison of frequency variation ω/ω_0 with debonding length for the composite beam with full width debonding for (a) S-S, (b) C-C and (c) C-F end conditions.

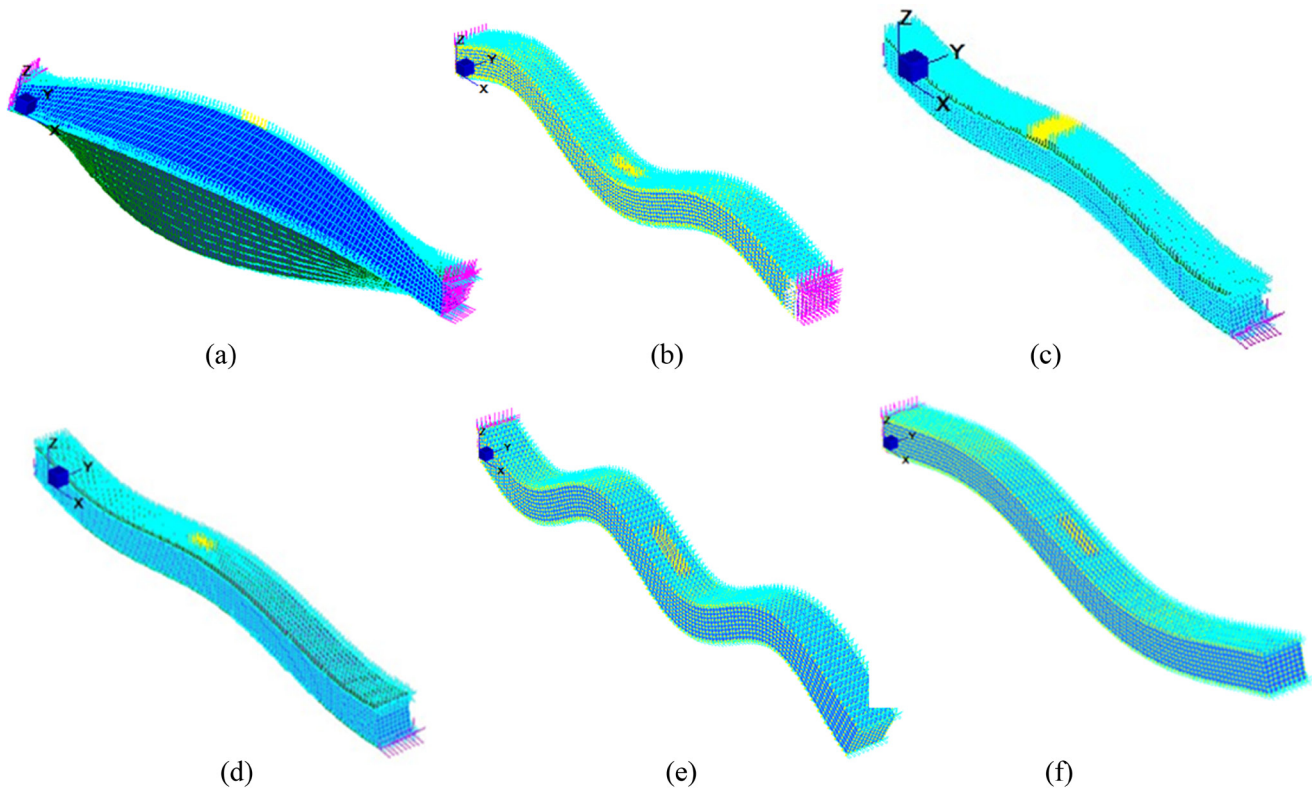


Figure 8. Comparison of prominent mode shapes for (a) Mode 3 (full width debonding for C-C case), (b) Mode 3 (half width debonding for C-C case), (c) Mode 3 (full width debonding for S-S case), (d) Mode 3 (half width debonding for S-S case), (e) Mode 3 (full width debonding for C-F case), (f) Mode 3 (half width debonding for C-F case) end conditions for full-width and half-width debonding (for 30 mm debond length).

even when the debonding is right through the full length of the composite beam. This is of great prominence as this confirms that if the working frequency of the beam is kept away from the range 50% to 100% of the virgin beam there is no possibility of resonance happening due to debonding in the beam.

4. CONCLUSIONS

This paper reports the variation in dynamic characteristics due debonding in a novel composite sandwich beam for simply supported, clamped-clamped and clamped-free end conditions. The numerical analysis was carried out us-

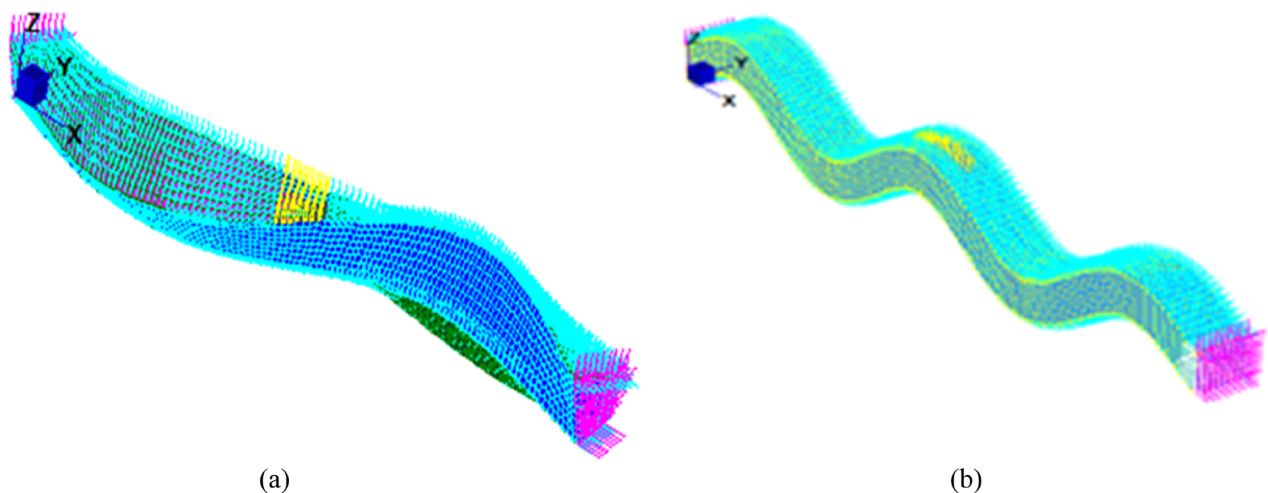


Figure 9. Comparison prominent of mode shapes for C-C beam for (a) Mode 6 (full width debonding) and (b) Mode 6 (half width debonding) debonding (for 30 mm debond length).

ing three dimensional modelling with Strand7 finite element code. The accuracy of the numerical solution was verified by comparing present results with published results for a similar problem. The following conclusions are made from the present study.

1. Generally, debonding reduces the natural frequency in comparison with full bonded composites.
2. Generally, natural frequency decreases more rapidly as the mode number increases giving the least variation for the first natural frequency.
3. Debonding causes some changes to the modes of vibration. These changes are dependent on the mode number and end conditions of the beam.
4. It is also revealed that full width debonding causes increased participation of twisting modes, compared to half width debonding, for clamped-clamped end condition.
5. The end conditions of the beam are also a governing factor dictating which modes are more affected.
6. Finally it is perceived that if the working frequency of the beam is kept away from the range 50% to 100% of the fully bonded beam, there is no possibility of resonance happening due to debonding for the novel composite beams considered in this analysis.

REFERENCES

- [1] Aravinthan, T. and Manalo, F., "Field applications and case studies of FRP in civil infrastructure: the Australian experience," Proceedings of 6th Inter. Conf. on FRP Composites in Civil Engineering (CICE 2012), Rome, Section 11: Field Applications and Case Studies, Paper 210, (2012).
- [2] Burlayenko, V. N. and Sadowski, T., "Influence of skin/core debonding on free vibration behavior of foam and honeycomb cored sandwich plates," *International Journal of Non-Linear Mechanics*, 45 (10), 959–968 (2010). <http://dx.doi.org/10.1016/j.ijnonlinmec.2009.07.002>
- [3] Kulkarni, S.V. and Fredericks, D., "Frequency as a parameter in delamination problem-A preliminary investigation," *Journal of composite materials*, 5, 112–119 (1971). <http://dx.doi.org/10.1177/002199837100500111>
- [4] Mujumdar, P.M. and Suyanarayan, S., "Flexural vibration of beams with delamination," *Journal of Sound and Vibration*, 125, 441–461 (1988). [http://dx.doi.org/10.1016/0022-460X\(88\)90253-2](http://dx.doi.org/10.1016/0022-460X(88)90253-2)
- [5] Wang, J.T.S., Lin, Y.Y. & Gibby J.A., "Vibration of split beams", *Journal of Sound and Vibration*, vol. 84, no. 4, pp. 491–520 (1982). [http://dx.doi.org/10.1016/S0022-460X\(82\)80030-8](http://dx.doi.org/10.1016/S0022-460X(82)80030-8)
- [6] Tracy, J.J. & Pardo, G.C., 'Effect of delamination on the natural frequencies of composite laminates', *Journal of Composite Materials*, vol. 23 no. 12, pp. 1200–1215 (1992).
- [7] Grouve, W.J.B., Warnet L., De Boer, A., Akkerman, R. and Vlekken, J., "Delamination detection with fibre bragg gratings based on dynamic behaviour." *Composite Science and Technology*, 68, 2418–2424 (2008). <http://dx.doi.org/10.1016/j.compscitech.2007.11.007>
- [8] Duggan, M. and Ochoa, O., "Natural frequency behaviour of damaged composite materials," *Sound and Vibration*, 158, 545–551 (1992). [http://dx.doi.org/10.1016/0022-460X\(92\)90424-V](http://dx.doi.org/10.1016/0022-460X(92)90424-V)
- [9] Hu, J.S. & Hwu, C., 'Free vibration of delaminated composite sandwich beams', *AIAA Journal*, vol. 33, no. 10, pp. 1911–1918 (1995).
- [10] Shu, D. & Fan H., 'Free vibration of a bimaterial split beam', *Composites: Part B*, vol. 27, no. 1, pp. 79–84 (1996). <http://dx.doi.org/10.2514/3.12745>
- [11] Karunasena, W., 'The effect of debonding on the natural frequencies of laminated fibre composite sandwich plates' *Proceedings of 6th Australasian Congress on Applied Mechanics*, ACAM 6, 12–15 December 2010, Perth, Australia (2010).
- [12] Ju F, Lee HP & Lee, KH, 'Free vibration of composite plates with delamination around cutouts', *Composite Structures*, vol. 31, pp. 177–183 (1995). [http://dx.doi.org/10.1016/0263-8223\(95\)00016-X](http://dx.doi.org/10.1016/0263-8223(95)00016-X)
- [13] Iao P, Lestari W, Shah, MG & Wang J, 'Dynamics-based Damage Detection of Composite Laminated Beams using Contact and Noncontact Measurement Systems', *Journal of Composite Materials*, vol. 41, no. 10, pp. 1217–1252 (2007). <http://dx.doi.org/10.1177/0021998306067306>
- [14] Chattopadhyay, A, Gu, H., 'A new higher order plate theory in modelling delamination buckling of composite laminates', *AIAA Journal*, vol. 32, No. 8, pp. 1709–1718 (1994). <http://dx.doi.org/10.2514/3.12163>
- [15] Chattopadhyay, A, Radu, AG & Dragomir-Daescu, D, 'A higher order plate theory for dynamic stability analysis of delaminated composite plates', *Computational Mechanics*, vol. 26, pp. 302–308 (2000). <http://dx.doi.org/10.1007/s004660000174>
- [16] Kim, HS, Chattopadhyay, A & Ghoshal, A, 'Dynamic analysis of composite laminates with multiple delamination using improved layerwise theory', *AIAA Journal*, vol. 41, no. 9, pp. 1771–1778 (2003a). <http://dx.doi.org/10.2514/2.7295>
- [17] Kim, HS, Chattopadhyay A & Ghoshal A, 'Characterisation of delamination effect on composite laminates using a new generalised layerwise approach', *Computers and Structures*, vol. 81, pp. 1555–1566 (2003b). [http://dx.doi.org/10.1016/S0045-7949\(03\)00150-0](http://dx.doi.org/10.1016/S0045-7949(03)00150-0)
- [18] Tenek, LH, Henneke, EG & Gunzburger, MD, 'Vibration of Delaminated Composite plates and Some Applications to Nondestructive Testing', *Composite Structures*, vol. 23, no. 3, pp. 253–262 (1993). [http://dx.doi.org/10.1016/0263-8223\(93\)90226-G](http://dx.doi.org/10.1016/0263-8223(93)90226-G)
- [19] Krueger R & Shell, A, '3D modeling technique for delaminations in composite laminates', *Proceedings of American Society of Composites*, pp. 843–852 (1999).
- [20] Yam LH, Wie Z, Cheng Z & Wong WO, 'Numerical analysis of multi-layer composite plates with internal delamination', *Computers and Structures*, vol. 82, pp. 627–637 (2004). <http://dx.doi.org/10.1016/j.compstruc.2003.12.003>
- [21] Burlayenko, V. N. and Sadowski, T., "Dynamic behaviour of sandwich plates containing single/multiple debonding," *Computational Materials Science*, 50 (4), 1263–1268 (2011). <http://dx.doi.org/10.1016/j.commatsci.2010.08.005>
- [22] Burlayenko, V. N. and Sadowski, T., "Finite element nonlinear dynamic analysis of sandwich plates with partially detached facesheet and core," *Finite Elements in Analysis and Design*, 62, 49–64 (2012). <http://dx.doi.org/10.1016/j.finel.2012.08.003>
- [23] Strand7. Strand7 finite element analysis FEA software, Release 2.4.1, Sydney, Australia (website: www.strand7.com), (2010).
- [24] Logan, D.L., [A first course in the finite element method], 5th edn, Cengage Learning, Stamford, USA (2012).
- [25] Schwarts-Givil, H., Rabinovich, O. and Frostig, Y., "Free vibrations of delaminated unidirectional sandwich panels with a transversely flexible core-a modified Galerkin approach," *Journal of Sound and Vibration*, 301, 253–277 (2007). <http://dx.doi.org/10.1016/j.jsv.2006.10.006>



Investigation of Mechanical and Physical Properties of PET Nanofiber Hollow Yarn

L. JAVAZMI^{1,*}, J. EPAARACHCHI² and S. A. HOSSEINI RAVANDI¹

¹Department of Textile Engineering, Isfahan University of Technology, Isfahan, 84156, Iran

²Dept. of Mechanical Engineering, University of Southern Queensland, Toowoomba QLD 4350, Australia

KEYWORDS

PET nanofiber
Hollow yarn
Core-sheath yarns
PVA multifilament
Physical and mechanical properties

ABSTRACT

In this study, mechanical and physical properties of polyethylene terephthalate (PET) nanofiber hollow yarn in various concentrations of PET polymeric solution were investigated. First, five different concentrations (18, 21, 24, 27, and 30% w/v) of PET solutions were prepared in (TFA) / (DCM) mixtures (70: 30 v/v), and then the electrospinning was done for each concentration in a way that to put PVA multifilament in the core and to twist PET nanofibers onto multifilament yarn as a sheath simultaneously, followed by dissolving PVA yarn in hot water, PET nanofiber hollow yarn was produce. The surveys of mechanical properties of PVA multifilament yarn, core-sheath yarns and hollow yarns showed that the PVA multifilament yarn and nanofiber hollow yarn in concentrations of 30% w/v PET polymeric solution had the highest and lowest average strength respectively. Also surveys of elongation showed that PVA multifilament yarn, core-sheath yarns and hollow yarns did not have any significant difference on average extension. Regarding physical properties, the wicking property of hollow yarns in different concentrations of polymeric solution were surveyed. Results showed that the PET nanofiber hollow yarn in concentration of 24% w/v PET polymeric solution had the highest coefficient wicking. More the regain moisture of hollow yarns were surveyed and concluded that the PET nanofiber hollow yarn in concentrations of 18% w/v PET polymeric solution had the most regain moisture.

© 2013 DEStech Publications, Inc. All rights reserved.

1. INTRODUCTION

Electrospinning has attracted a lot of interest as a technique that is very simple and inexpensive to manufacture sub-micron fibers and nanofibers from polymer solutions or melts [1]. In a typical process, an electrical potential is applied between droplet of a polymer solution, or melt, held at the end of a capillary tube and a grounded target. When the applied electric field overcomes the surface tension of the droplet, charged jet of polymer solution is ejected. The trajectory of the charged jet is controlled by the electric field. The jet exhibits bending instabilities due to repulsive forces between the charges carried with the jet. The jet extends

through spiraling loops, as the loops increase in diameter the jet grows longer and thinner until it solidifies or collects on the target [2,3].

Polymer nanofibers provide a platform for a number of diverse applications, including drug encapsulation, biosensing, filtration and electronics [4]. For the last decade, hollow nanostructures with a controlled pore volume and shell thickness have emerged as an important class of nanomaterials. These hollow nanostructures have much higher surface to volume ratio compared to the solid counterparts with the same sizes, which would be beneficial for applications including catalysis, energy storage and conversion, and biomedicine [5].

Many advanced processing techniques, such as template synthesis, self assembly, and electrospinning have been employed to make hollow, core/sheath, porous fibers and tubes

*Corresponding author. Tel: +983113912425; Fax: +983113912444;
Email: l.javazmi@tx.iut.ac.ir

from natural and synthetic polymers [6]. Coaxial electrospinning has been extensively exploited as a simple technique to generate hollow and core/sheath nanofibers. Many researchers have employed different methods such as electrified coaxial liquid jets, co-electrospinning, and electrospinning with a two-capillary spinneret to generate hollow and core/sheath nanofibers [7].

To the best knowledge of the researcher, up until now, a few research projects attempted to obtain hollow yarn by using the electrospinning process. In a recent work, for example, Bhargava by a hollow rotating metal rod with attached hollow metal hemisphere at one end and two different polymer solutions could electrospin a core-sheath yarn. More by removing the inner core yarn (PVA electrospinning yarn) in boiling water, hollow nanofiber yarn could be obtained [8].

In present work, various concentration of PET polymeric solutions were prepared in (TFA) / (DCM) mixtures, and then the electrospinning was done in a way that to put PVA multifilament in the core and to twist PET nanofibers onto multifilament yarn as a sheath simultaneously, followed by dissolving PVA yarn in hot water, PET nanofiber hollow yarn was produced. More mechanical and physical properties such as strength, regain moisture and wicking of PET hollow nanofiber yarns in different concentrations were surveyed.

2. APPROACH

2.1. Materials

Five different concentrations (18, 21, 24, 27, and 30% w/v) of PET (Shahid Tondgooian Petrochemical Company, Iran) solutions were prepared in trifluoroacetic acid (TFA)/ dichloromethane (DCM) mixtures (70: 30 v/v) at room temperature for two hours. The solvents were purchased from Merck (Germany). A 488/144 denier (54.4 tex) PVA multifilament yarn was used as the core.

2.2. Electrospinning set-up

The schematic setup for electrospinning is shown in Figure 1. It consists of a high voltage-power supply, two

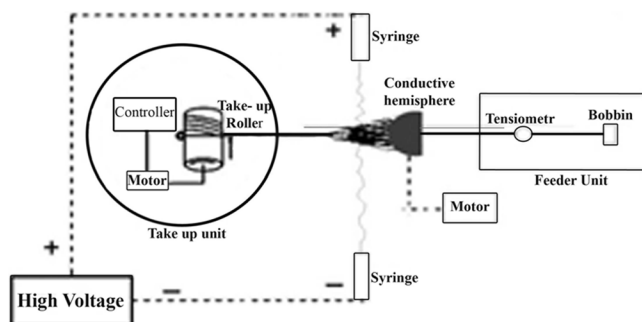
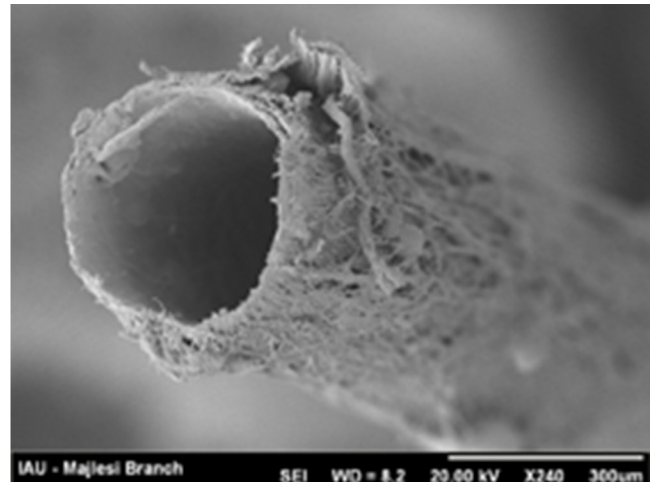
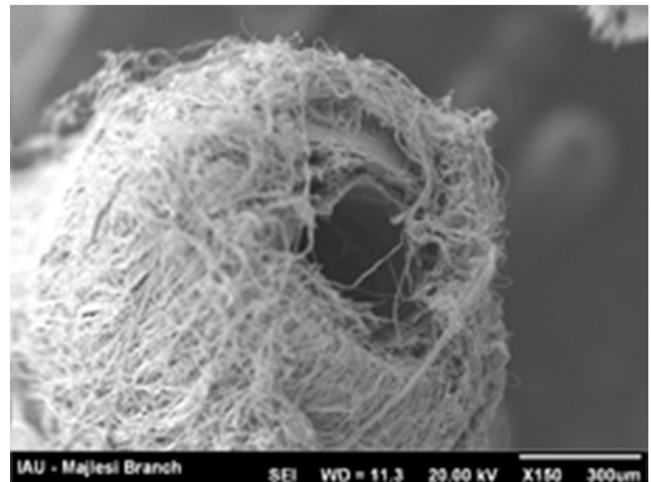


Figure 1. Schematic illustration of electrospinning setup to produce hollow nanofiber yarn.



(a)



(b)

Figure 2. SEM image of the cross-section area of PET hollow nanofiber yarn at concentration of (a) 18% and (b) 30% w/v polymeric solution.

syringe needles, a conductive hemisphere, a feeder unit and a take up unit. The hemisphere diameter was 8 cm. The syringe needles were located 2 cm from the hemisphere and 21 cm from take up unit, and 15 cm from each other. Electrospinning was done between two syringe needles, then electrospun nanofibers collected on hemisphere surface and twisted by rotating the hemispherical collector. In order to produce core-sheath yarn, a PVA multifilament was fed as the core from feeder unit to take up unit by hollow metal rod that attached to the hemispherical collector. PET nanofibers were twisted onto the PVA yarn as the sheath, and then core-sheath yarn was drawn and collected on take up roller. Hollow yarn was obtained by removing the PVA yarn in water at 60°C for 24 hours. Figure 2(a) and 2(b) show SEM image of the cross-section area of PET hollow nanofiber yarn at concentration of 18% and 30% w/v polymeric solution, respectively.

3. RESULTS AND DISCUSSION

3.1. Mechanical Properties

The statistical analysis of the results of the ratio of inner to outer average diameter of hollow yarn at different concentrations showed that there are two different groups. First group and second group included hollow and core-sheath yarns with concentrations of 18%, 21% and 24%, 27%, 30% polymeric solution, respectively. So mechanical properties only were considered for hollow and core-sheath yarns with concentration of 18% and 30% polymeric solution. The results from tensile testing of the hollow and core-sheath yarns were summarized in Table 1. Observes showed that while a core-sheath yarn was extended, the fibers were strained and first of all, the fiber with lowest strength broke. The results from Table 1 showed the average strength of the PVA multifilament yarn was more than the strength of hollow and core-sheath yarns; moreover, hollow nanofiber yarns at concentration of 30% had the lowest strength. Results showed that the strength of core-sheath yarn at 18% concentration was more than the strength of core-sheath yarn at concentration of 30% polymeric solution. Obviously, the core-sheath yarn's strength depended on the weaker component strength, and the PET nanofibers were the weaker portion. Hence, when the polymeric solution concentration increased from 18% to 30%, core-sheath yarn's strength decreased. The results of the statistical analyses showed that the difference in the strength of PET hollow nanofiber yarns in various concentrations of polymeric solution weren't significant. Also, the results of the breaking elongation of the core-sheath yarns and hollow yarns were about same as the PVA multifilament yarn elongation, and the results of a statistical Tukey-test of significance showed no meaningful differences in the elongation of PVA, core-sheath and hollow yarn.

3.2. Physical Properties

3.2.1. Wicking

Figure 3 on the basis of Lucas-Washburn's equation showed the the capillary rate coefficient of hollow yarn in concentration of 24% was the highest because the sheath of

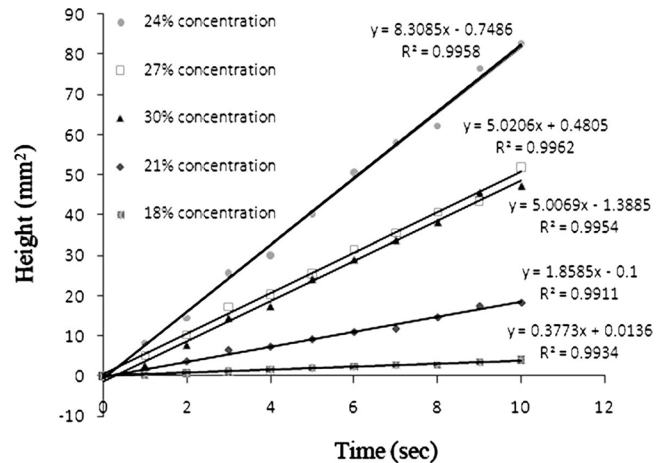


Figure 3. The capillary rise of colored liquid into hollow yarns as a function of time at polymeric solution concentration of (a) 18%, (b) 21%, (c) 24%, (d) 27%, and (e) 30% (w/v).

hollow yarn in concentration of 24% was more thick than hollow yarns in concentration of 18% and 21%, so the capillary spaces among PET nanofibers in sheath of 24% hollow yarn was more than hollow yarn at concentration of 18% and 21% polymeric solutions. On the other hand, the efficiency of extracting the PVA multifilament from PET hollow nanofiber yarn decreases with increasing concentrations. Therefore, the inner spaces of 24% hollow yarn was more than hollow yarns at concentrations of 27% and 30% and the colored liquid could rise into hollow yarn at 24% concentration more than 27% and 30% concentrations.

3.2.2. Regain Moisture

Table 2 showed that the regain moisture of hollow yarn at different concentrations of polymeric solution. The results indicated that the regain moisture of PET hollow nanofiber yarns decreased with increasing concentration. Because the efficiency of extracting the PVA multifilament from PET hollow nanofiber yarns decreased with increasing concentration, there were more spaces and air into hollow yarn in lower concentrations. Moreover, due to the low regain moisture of PET, so the air into hollow yarn had the main role in holding regain moisture.

Table 1. Mechanical Properties of the Core-sheath, Hollow and PVA Yarns.

Property	No. of Test	Stress at Break		Strain at Break		Work Up to Break		E-modulus	
		Mpa	Cv%	%	Cv%	Nmm	Cv%	Gpa	Cv%
PVA yarn	10	383.37	7.46	29.05	12.39	94.13	11.45	7.23	9.93
Core-sheath yarn (18% w/v)	10	289.12	9.87	29.60	14.39	97.38	16.38	3.26	29.48
Core-sheath yarn (30% w/v)	10	125.10	11.07	30.11	20.59	116.07	25.47	1.91	24.54
Hollow yarn (18% w/v)	10	89.98	16.56	25.27	19.46	24.68	36.38	2.23	31.4
Hollow yarn (30% w/v)	10	63.62	29.06	27.61	31.54	73.76	26.22	1.20	27.94

Table 2. The Regain Moisture of Hollow Nanofiber Yarns at Different Concentrations.

Polymeric Solution Concentration (w/v%)	Regain Moisture (%)
18%	6.39 ± 0.02
21%	3.89 ± 0.01
24%	2.72 ± 0.01
27%	2.46 ± 0.02
30%	2.09 ± 0.02

4. CONCLUSIONS

In this study, five different concentrations (18, 21, 24, 27, and 30% w/v) of PET solutions were prepared in (TFA)/(DCM) mixtures (70:30 v/v), and then the electrospinning was done for each concentration in a way that to put PVA multifilament in the core and to twist PET nanofibers onto multifilament yarn as a sheath simultaneously, followed by dissolving PVA yarn in hot water, PET nanofiber hollow yarn was produce. In surveying the strength and moduls value of PVA multifilament yarn, core-sheath yarns and hollow yarns, results showed that the PVA yarn and nanofiber hollow yarn in concentrations of 30% w/v PET polymeric solution had the highest and lowest strength respectively. Also observes showed that PVA multifilament, core-sheath yarns and hollow yarns did not have any significant different on average extension. Regarding physical properties, results showed that the PET nanofiber hollow yarn in concentration of 24% w/v PET polymeric solution had the highest coefficient wicking, and the PET nanofiber hollow yarn in concentrations of 18% w/v PET polymeric solution had the most regain moisture.

ACKNOWLEDGEMENTS

The authors are grateful to Farzad Dabirian and Abbas Tabibi (Research Center of Fiber Science and Technology, Textile Engineering Department, IUT) for their help in electropun yarn production.

REFERENCES

- [1] Li, D. Xia. and Y. N., "Electrospinning of Nanofibers Reinventing the Wheel?," *Advanced Materials*. 16(14), 1151–1170(2004). <http://dx.doi.org/10.1002/adma.200400719>
- [2] Reneker. D.H., Yarin A.L., Fong H. and Koombhongse S., "Bending Instability of Electrically Charged Liquid Jets of Polymer Solutions in Electrospinning," *Appl. Phys.* Vol. 87, 4531–4547(2000).
- [3] Shin, Y. M., "Experimental Characterization of Electrospinning: The Electrically Forced Jet and Instabilities," *Polymer*. Vol. 42, 9955–996(2001). [http://dx.doi.org/10.1016/S0032-3861\(01\)00540-7](http://dx.doi.org/10.1016/S0032-3861(01)00540-7)
- [4] Zhong, X. H., Kim, K.S., Fang, D.F., Ran, S. F., Hsiao, B.S. and Chu. B., "Structure and Process Relationship of Electrospun Bioabsorbable Nanofiber Membranes," *Polymer*. Vol. 43, 4403–4412(2002). [http://dx.doi.org/10.1016/S0032-3861\(02\)00275-6](http://dx.doi.org/10.1016/S0032-3861(02)00275-6)
- [5] Lou, X. W., Archer, L. A. and Yang, Z., "Hollow Micro-/Nanostructures: Synthesis and Applications," *Advanced Materials*. 20(21), 3987–4019(2008). <http://dx.doi.org/10.1002/adma.200800854>
- [6] Bognitzki, M., Hou, H. Q., Ishaque, M., Frese, T., Hellwig, M., Schwarte, C., Schaper, A., Wendorff, J. H. and Greiner, A., "Polymer metal, hybrid nano and mesotubes by coating degradable polymer template fibers," *Advanced Materials*. 12(9), 637–640(2000). [http://dx.doi.org/10.1002/\(SICI\)1521-4095\(200005\)12:9<637::AID-ADMA637>3.0.CO;2-W](http://dx.doi.org/10.1002/(SICI)1521-4095(200005)12:9<637::AID-ADMA637>3.0.CO;2-W)
- [7] McCann, J. T., Li, D. and Xia, Y. N., "Electrospinning of nanofibers with core-sheath, hollow, or porous structures," *Mater. Chem*. 15(7), 735–738(2005). <http://dx.doi.org/10.1039/b415094e>
- [8] S. Bhargava, "Submicron size structures, electrospinning and filters", The Graduate Faculty of The University of Akron (2007).



Experimental Investigation and Control of Magnetorheological Damper towards Smart Energy Absorption based Composite Structures for Crashworthiness

SHEN HIN LIM*, B. GANGADHARA PRUSTY, ANN LEE and GUAN HENG YEOH

School of Mechanical and Manufacturing Engineering, University of New South Wales, Sydney, NSW, 2052, Australia

KEYWORDS

MR damper
Crashworthiness
Controller

ABSTRACT

This paper presents an extended experimental investigation and efficient control of magnetorheological (MR) damper towards smart energy absorption based composite structures for systems for crashworthiness. While the experimental evaluation of an existing MR damper based on the damping force was successful in our earlier work, the MR damper capability can be further examined with the wider range of velocities. Using two arms configuration, an experimental test rig is designed to enable the MR damper to be investigated throughout its full velocity range capability. A MR damper compatibility study to an existing composite tube was also conducted and showed promising quality to improve composite structures as systems for crashworthiness. A controller was then developed based on the MR damper investigation to provide automated variable control of induced current with a set crushing force and available data of composite tube crushing force. Numerical analysis on the proposed controller conveyed that MR damper was successfully controlled to provide consistent crushing force despite oscillation from the composite tube crushing force.

© 2013 DEStech Publications, Inc. All rights reserved.

1. INTRODUCTION

In the recent years, lightweight and crashworthy composite materials have been integrated into new helicopters and aircrafts design. Hence, they are strong candidate for retrofit technologies suitable for aged helicopters such that newer helicopter crashworthy standards are met [1]. Extensive research has been conducted for understanding the crushing behaviour of composite structures to achieve successful application of retrofit technologies. The advantages of the composite structures can also be extended by integration of a different material that can be controlled in active or passive mode. Magnetorheological (MR) fluids rheological behaviour has allowed easy and accurate control of these fluids based systems by an external magnetic field [2]. The low power requirement also allows MR fluids based system to be operated independent of other systems. Thus, MR fluids have been applied as semi-active damping systems in civil

engineering structures for earthquake mitigation [3–5] and effective energy absorbers for crashworthy seats [6–7].

The easy controllability of MR fluids has led to a large number of research work and its application were focused on developing an effective control of this highly nonlinear device and multiple MR damper applications [3–4]. A clipped-optimal control strategy based on acceleration feedback is developed by Dyke *et al.* [3] and when compared to an active linear control system, the peak displacements of a building are reduced by the implementation of this strategy. Large-scale MR damper systems have also been successfully applied using dynamic modelling proposed by Yang *et al.* [4–5]. The potential of MR fluids in other applications in different areas such as aerospace and automobile industry, which include those restricted in size and weight is realised following the success from the intensive modelling exercise of MR dampers in civil engineering structures.

In crashworthy seats, magnetorheological energy absorbers (MREAs) are developed to be an alternative to the conventional energy absorbers. The load-stroke profile is also

*Corresponding author

capable to be adapted as a function of occupant weight or real-time crash load levels. Investigations conducted by Choi and Wereley [6] found that MREAs are superior to conventional passive hydraulic seats under vibration and shock loads created from normal and crash landing situations. Similar results were also reported by Hiemenz *et al.* [7]. A subsequently study was conducted to measure the performance of the current MREAs based on vibration isolation and crashworthiness conditions and showed that the weight of the MREAs is a major issue for satisfactory performance in these conditions simultaneously. While current MREAs development showed limited applications, removing the MREAs limitations could escalate MR fluids application into other areas of crashworthiness systems.

In our earlier work [8], the damping force of an existing MR damper from LORD Corporation [9] was evaluated experimentally within the investigation of the MR fluids compatibility to enhancement of structures energy absorption. While the experimental investigation was successful, the MR damper can be further evaluated within its full velocity range capability. This paper presents two designs; where the first designs an experiment test rig using two arms configuration with ten to one length ratio to enable the MR damper investigation in the full velocity range capability. The assessment of MR damper based on this rig was then utilised to construct the controller design for automated variable control of induced current with the set crushing force and the crushing force obtained from composite tube.

An overview of the earlier work and limitations of the experiment configuration setup are first detailed in this paper. This is followed by design of experimental test rig and assessment of MR damper throughout its full velocity range capability in Section 3. The controller design and numerical investigation are presented in Section 4. Finally, Section 5 covers the conclusion and future work.

2. PRELIMINARY INVESTIGATION OF MR DAMPER

The preliminary investigation of MR damper was aimed to evaluate the damping force as a measure of compatibility to composite structures. Figure 1 shows the schematic of

the experimental setup, where the existing MR damper RD-8041-1 and manual controller device called a Wonderbox that controlled the induced current I were purchased from the LORD Corporation [9]. The MR damper was tested on hydraulic uniaxial testing machines (Instron) and the tests were conducted using cyclic loading with variations of velocity v_0 , which are controlled by the Instron machine and induced current I . The velocity v_0 was varied between 0 and 20 mm/s while the induced current I was varied between 0 and 1.68A. The cyclic loading is set to travel in a trapezoidal wave with the peak to peak distance of 40 mm. The outputs of the test, which are the damping force F_D and displacement, were recorded by the data acquisition system associated with the Instron testing machine. For each test, the maximum damping force was used for the analysis of experimental results.

The damping force distribution based on the cyclic loading tests is shown in Figure 2. The data extracted from the manufacturer's (LORD) [9] specification sheet is depicted by the dotted lines at $I = 0A$, $I = 0.5A$ and $I = 1A$. The results from the cyclic loading test matched to those obtained from the manufacturer's specification and agreed with the rheological behaviour of MR fluids. The maximum damping force was compared to the crushing force of a 38.1 mm diameter and 2 mm thickness composite tube and showed that MR damper is capable to achieve 38% of the composite tube crushing force. Irregularities of the force distribution, however, were noted within the set Instron velocity range, as the tested velocity range covered only a tenth of the velocity operational capability of the MR damper. Higher velocity was not tested as the velocity limitation of the Instron machine is 20 mm/s. The evaluation of MR damper within its full velocity range capability is required to develop a simulated MR damper utilised for the controller design.

3. DESIGN OF EXPERIMENTAL TEST RIG AND INVESTIGATION OF MR DAMPER BASED ON MODIFIED EXPERIMENTAL CONFIGURATION SETUP

Using the two arms configuration, the experiment test rig was developed to amplify the velocity from the Instron machine by a factor of ten such that the MR damper can be

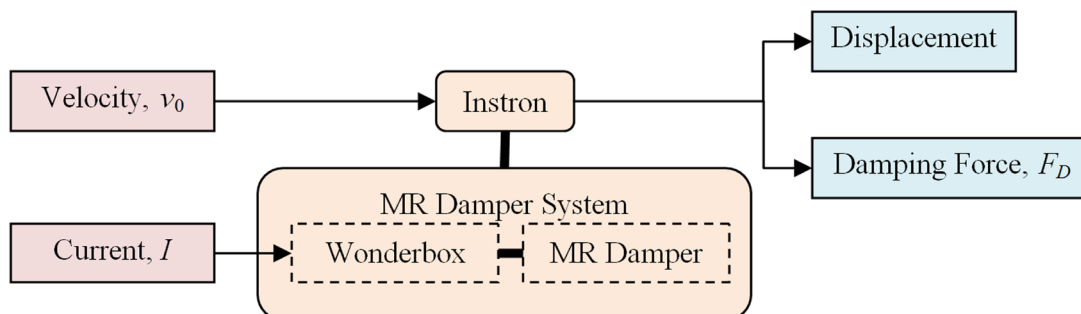


Figure 1. The schematic of the experimental configuration setup.

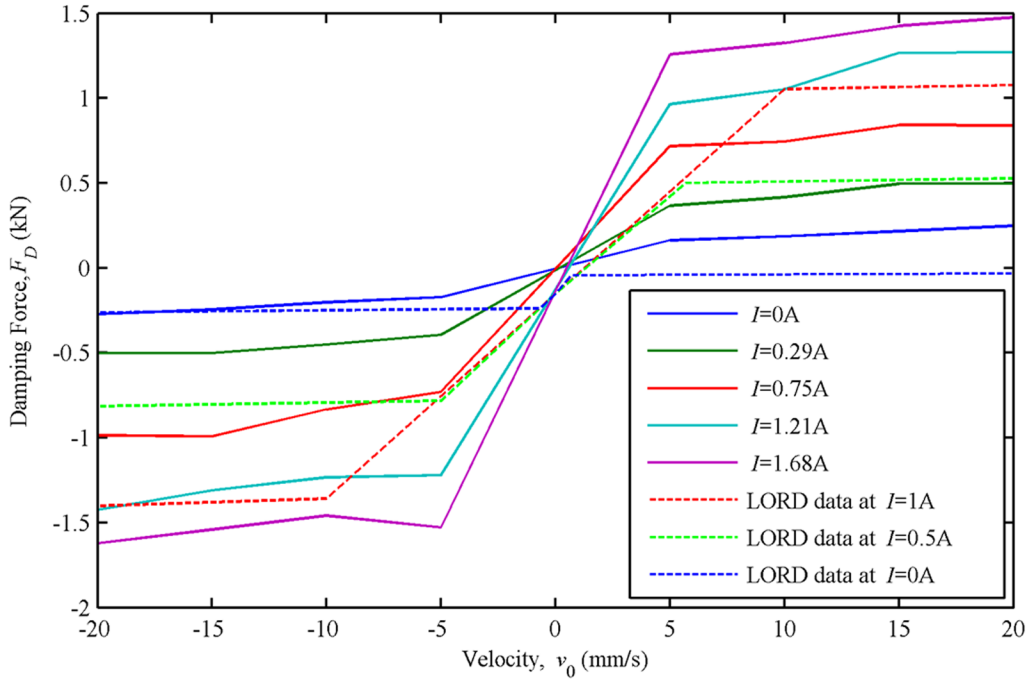
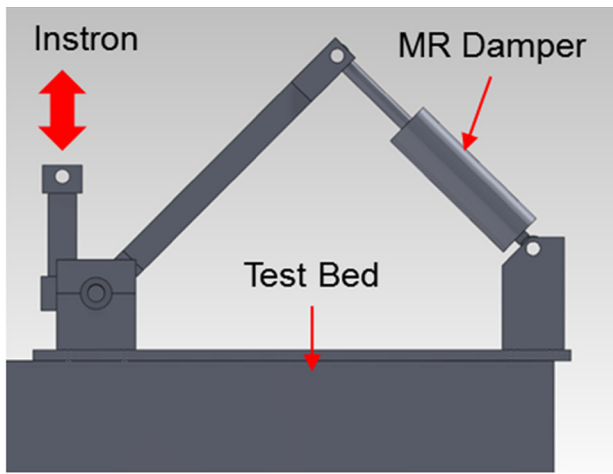


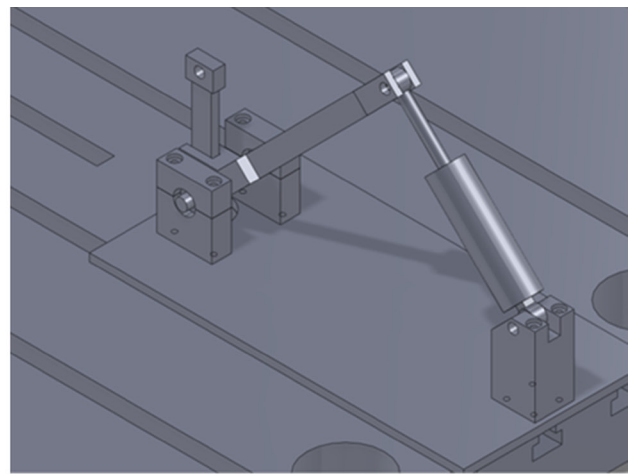
Figure 2. Damping force-velocity profile of the existing MR damper based on the experimental test (solid line) and data extracted from LORD specification sheet [9] (dotted line).

evaluated within its velocity full range capability. The rig was also designed to fit in the limited space of the Instron machine test bed. The design of the experimental test rig is shown in Figure 3, where Figure 3(a) illustrates the corresponding position of the Instron machine and MR damper while Figure 3(b) depicts the position of the experimental test rig with respect to the test bed of the Instron machine. In this design, the vertical line of force action of the Instron machine is retained and the force being applied to the MR damper is always perpendicular to the long arm length during the test.

The experimental setup with the design experimental test rig implementation is shown in Figure 4. As compared to the previous experimental configuration setup, the inputs to initiate the tests were frequency and amplitude of sinusoidal waves. This change was required to compensate the setback of the stroke governed by the Instron machine, which was reduced by a factor of ten to retain the 40 mm peak to peak stroke distance of the MR damper. The variations of the induced current I were the same as the previous experimental configuration setup. The displacement of the MR damper will be measured by the attached Linear Variable Differen-



(a)



(b)

Figure 3. The overall design of the experimental test rig with highlighted position of Instron and MR damper.

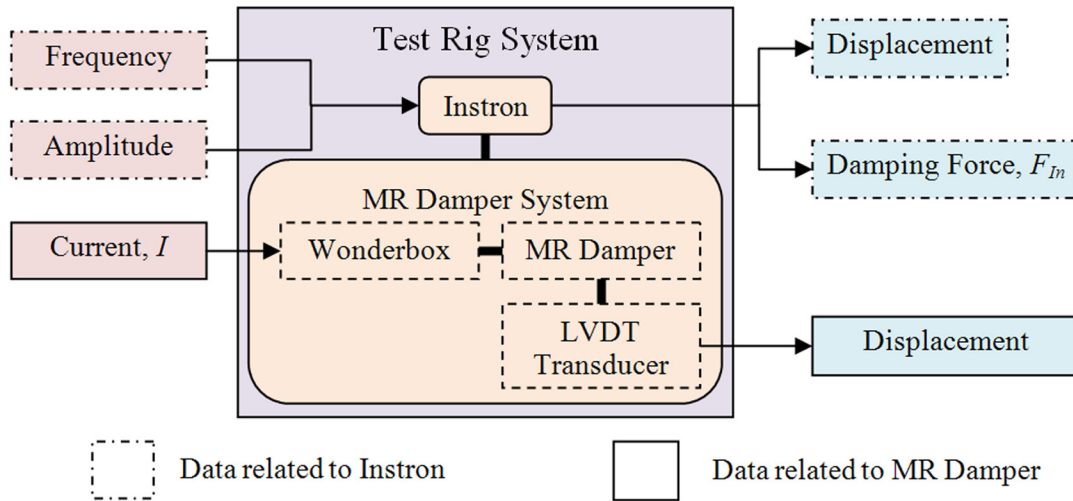


Figure 4. The schematic of modified experimental configuration setup.

tial Transformer (LVDT) transducer. The force required by the Instron machine F_{In} to operate the MR damper and its corresponding stroke distance were measured by the data acquisition associated within the Instron machine.

These outputs from Instron and LVDT transducer were then utilised to obtain their respective velocities and the ratio between the velocities and the force F_{In} were then applied to calculate the damping force of the MR damper F_D . The damping force distribution based on the modified experiment configuration setup and the variations of the induced current I is conveyed in Figure 5. The damping force of from

this experiment setup correlates well with the data extracted from LORD specification sheet and further support the findings reported by the results of the previous configuration setup. The irregularities of the damping force that exist in the previous configuration setup are diminished in this current experiment configuration setup.

The damping force F_D from the loading tests of the experiment was further evaluated in this section to measure the compatibility of the MR damper to composite structures energy absorption quantitatively. In this assessment, these forces were compared to experimental data obtained from

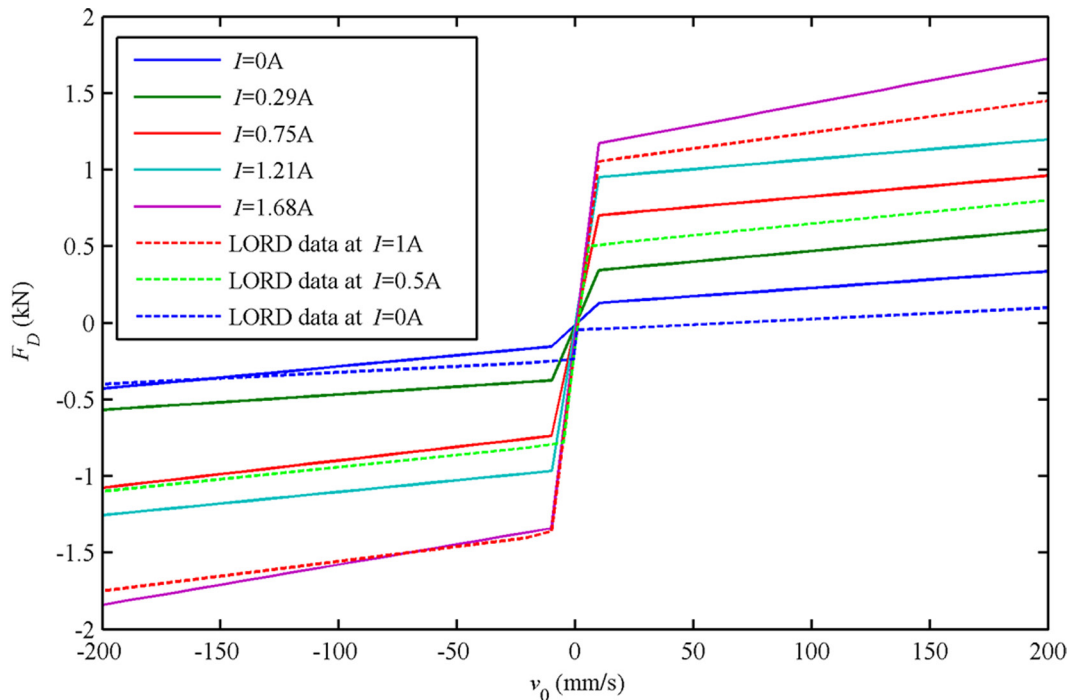


Figure 5. Damping force-velocity profile of the existing MR damper based on the modified experimental test (solid line) and data extracted from LORD specification sheet [9] (dotted line).

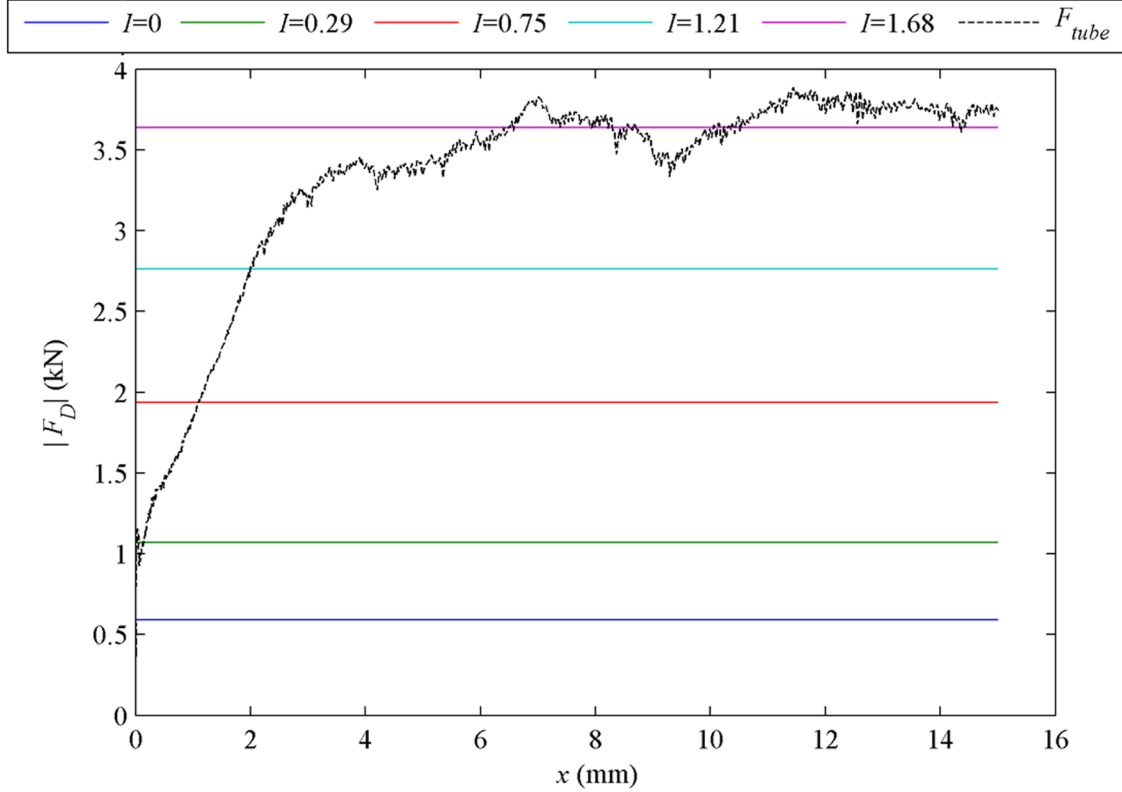


Figure 6. Force distribution based on 15 mm stroking distance with five different magnetic field strengths at 150 mm/s in full cyclic loading cases.

an investigation of a composite tube energy absorption and behaviour using different variety of triggering radius [10] as part of a composite crashworthy system development. The composite tube has a similar diameter to the MR damper and thus allowed the direct comparison. The composite tube was manufactured by Exel Composites and was a fabric pre-preg ($0^\circ/90^\circ$ layup), 38.1 mm inner diameter, 1mm thickness and 120 mm height. The experimental data was the force, F_{tube} and its corresponding displacement during a quasi-static crushing experiment with a 6mm triggering radius [10]. The variations of current with total cyclic loading at 150 mm/s is shown in Figure 6. The maximum damping force produced by the MR damper in a full cyclic loading case was equivalent to the mean of F_{tube} and thus was capable to double the crushing performance of the F_{tube} while maintaining the stability of specific energy absorption when appropriate control of the MR damper can be applied. The required parameters for the controller design were extracted from these results and are detailed in the next section.

4. CONTROLLER DESIGN

The experimental damping force-velocity profile achieved in the previous section was modelled using force Bingham model, where the model is governed by two parameters that are the damping coefficient and the shear force

and the inputs that are the velocity and induced current. Both the parameters were obtained with respect to the positive and negative velocity regions. These parameters were referred as $C^{(.)}$ and $F_{D^{(.)}}$, where $(.)$ is either p or n based on the positive or negative velocity regions respectively. The damping coefficient of each region was attained by averaging the gradients extracted from the lines of the induced current variations given by data shown in Figure 5. The shear force of each region, meanwhile, was dependent on the value of the induced current and thus, was acquired using the force and induced current relationship based on the results in the previous section. The relationship gradient and constant were referred as $\alpha_{(.)}$ and $\beta_{(.)}$. The parameter values are summarised in Table 1.

The aim of this controller design is to regulate the current to produce the equivalent MR damper damping force such that a constant force is achieved throughout the crushing stroke distance of the composite tube. The schematic

Table 1. The Parameter Values for Controller Design.

Positive			Negative		
C_p (Ns/m)	α_p (N/A)	β_p (N/A)	C_n (Ns/m)	α_n (N/A)	β_n (N)
1610.2	618.2	159.2	1679.3	-685.2	-160.2

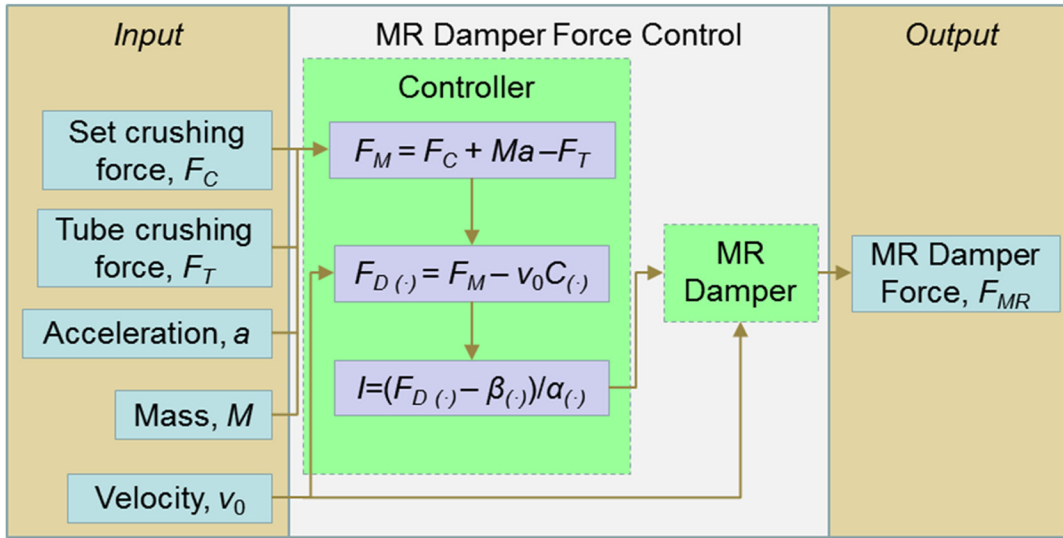


Figure 7. The schematic of MR damper force controller.

of the proposed controller design is illustrated in Figure 7. The inputs for the controller are the required minimum set crushing force to be achieved by the composite system F_C , the force response of the composite tube F_T , the acceleration and the mass of the passenger M and a , and the velocity v_0 . The minimal force required to be achieved by the MR damper F_{MR} is first determined using F_C , F_T and the respective M and a , and is followed by computing shear force $F_{D(\cdot)}$

requirements using the damping coefficient $C(\cdot)$ and velocity v_0 . The required current I is then calculated by utilising the force and induced current relationship gradient and constant $\alpha(\cdot)$ and $\beta(\cdot)$. In this controller design the induced current is set with a maximum and minimum limit of 1.68A and 0A. The resultant MR damper force F_{MR} based on the regulated induced current is then computed using the MR damper force Bingham model. This controller is designed using Simulink.

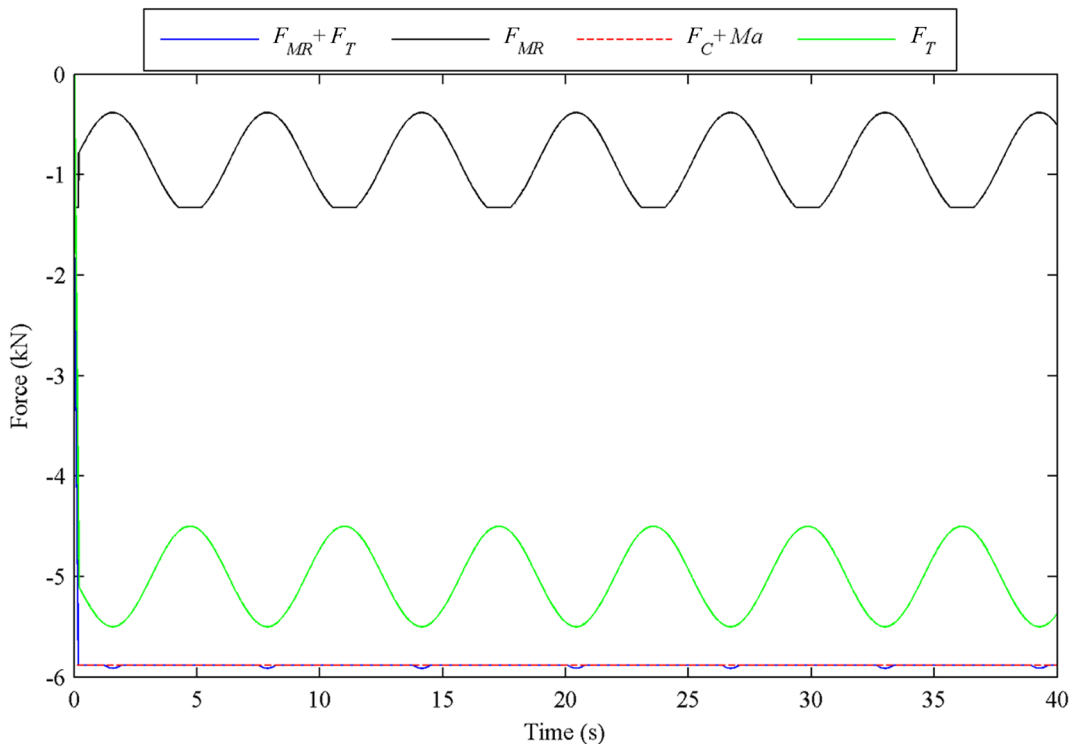


Figure 8. Force distribution based on the controller design, where F_{MR} is the resultant damping force, F_T is the tube crushing force, F_C is the required minimum set crushing force, M is the mass of the passenger and seat and a is the acceleration of the passenger and seat.

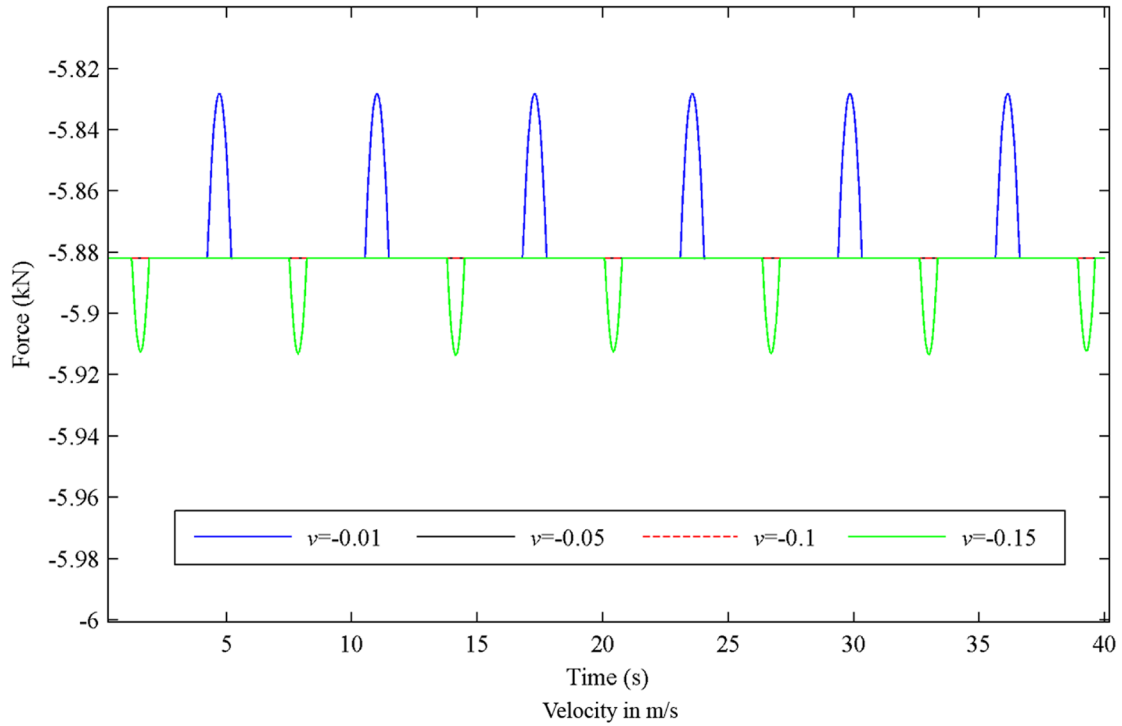


Figure 9. Force distribution based on the velocity set at -0.01 , -0.05 , -0.1 and -0.15 m/s.

A numerical example was set up to investigate the performance of the controller. The set crushing force F_C was set at -5 kN, where the sign indicated the compressive force. The tube crushing force was set to oscillate in sinusoidal wave at the mean of 5 kN with frequency and amplitude of 1 Hz and 500 N. The remaining inputs were set to be constant, where the acceleration was -9.8m/s^2 and the mass of the passenger was 90kg and the velocity was -0.15m/s . Figure 8 shows the force distribution of the numerical example. The controller managed to regulate the tube crushing force to be constant and achieved required minimum set crushing force. There exist tiny humps on the resultant crushing force of the combined composite tube and MR damper force as the required induced current is less than zero.

Another numerical example was set up by modifying the velocity to -0.02 , -0.05 , -0.1 and -0.15 m/s while maintaining other initial parameters. The resultant crushing force distribution based on the different set velocities is illustrated in Figure 9. Tiny humps also occur at the resultant crushing force when the velocity was set at -0.01 m/s as the required induced current exceeded the maximum limit set in the controller. The ideal resultant crushing force was achieved when the velocity was at -0.05 and -0.1 m/s and set the upper and lower boundary velocity limits for the controller to achieve optimal MR damper control. This further shows that the controller was limited by the capability of the MR damper and would not be able to provide efficient force regulator if the required minimum set crushing force exceeds the maximum MR damping force.

5. CONCLUSION

The designs of an experimental test rig and controller have been presented in this paper. The experimental test rig was developed using two arms configuration with ten to one length ratio to further investigate the MR damper within its full range of velocity capability. The modified experiment configuration setup that implemented the experimental test rig has showed that the existing MR damper has promising quality to improve composite structures as systems for crashworthiness. A better representation of the force velocity profile of the existing MR damper has been achieved using this modified experimental setup. This profile has been modelled using force Bingham model and the corresponding damping coefficient as well as the parameters based on the force and induced current have been determined. The controller is designed based on these parameters and the numerical example showed that the controller managed to regulate the oscillating force from the composite tube and achieved the minimum set crushing force. The controller, however, was limited by the capability of the existing MR damper. The concept of the controller shows promising potential to increase the crushing force capability of the composite structures while capable to minimise the oscillation of the composite structures crushing force.

An investigation on feedback control to be adapted to the current design controller is required to provide a more stable discrete controller and subsequently, the controller is required to be evaluated experimentally.

ACKNOWLEDGEMENTS

This work is part of the research program of the Cooperative Research Centre for Advanced Composite Structures P2.1 Systems for Crashworthiness. The authors wish to acknowledge Dane Wassell.

REFERENCES

- [1] Joosten, M.W., Dutton, S., Kelly, D., Thomson, R. and Johnson A. F., "Developing crashworthy composite helicopter structures: A building block approach," 14th Australian International Aerospace Congress (2010).
- [2] Felt, D. W., Hagenbuchle, M. and Liu J., "Rheology of a magnetorheological fluid," *Journal of Intelligent Material Systems and Structures* 7, 589–593 (1996). <http://dx.doi.org/10.1177/1045389X9600700522>
- [3] Dyke, S. J., Spencer, B. F., Sain, M. K. and Carlson, J. D., "Modeling and control of magnetorheological dampers for seismic response reduction," *Smart Materials and Structures* 5, 565–575 (1996). <http://dx.doi.org/10.1088/0964-1726/5/5/006>
- [4] Yang, G., Spencer, B. F., Carlson, J. D. and Sain, M. K., "Large-scale MR dampers: Modeling and dynamic performance considerations," *Engineering Structures* 24, 309–323 (2002). [http://dx.doi.org/10.1016/S0141-0296\(01\)00097-9](http://dx.doi.org/10.1016/S0141-0296(01)00097-9)
- [5] Yang, G., Spencer, B. F., Jung, H. and Carlson, J. D., "Dynamic modeling of large-scale magnetorheological damper systems for civil engineering applications," *Journal of Engineering Mechanics* 130, 1107–1114 (2004). [http://dx.doi.org/10.1061/\(ASCE\)0733-9399\(2004\)130:9\(1107\)](http://dx.doi.org/10.1061/(ASCE)0733-9399(2004)130:9(1107))
- [6] Choi, Y. and Wereley, N. M., "Biodynamic response mitigation to shock loads using magnetorheological helicopter crew seat suspensions," *Journal of Aircraft* 42 (5), 1288–1295 (2005). <http://dx.doi.org/10.2514/1.6839>
- [7] Heimenz, G. J., Hu, W. and Wereley, N. M., "Investigation of MR dampers for enhanced crashworthiness and vibration isolation of helicopter crew seats," *American Helicopter Society 63rd Annual Forum*, 1187–1202 (2007).
- [8] Lim, S. H., Prusty, B. G. Pearce, G., Kelly, D. and Thomson, R., "Directional enhancement of composite structures energy absorption using magnetorheological fluids," *28th International Congress of the Aeronautical Sciences* (2012).
- [9] LORD corporation, [http://www.lord.com/Products-and-Solutions/Magneto-Rheological-\(MR\)/MR-Store.xml](http://www.lord.com/Products-and-Solutions/Magneto-Rheological-(MR)/MR-Store.xml)
- [10] Hou, T., Pearce, G., Prusty, B. G., Lim, S. H., Kelly, D., Thomson, R., "Experimental development and analysis of an active crushing element using pressurised composite tubes," *28th International Congress of the Aeronautical Sciences* (2012).



Damage in Hybrid Composite Laminates[†]

HALEH ALLAMEH HAERY* and HO SUNG KIM

*Mechanical Engineering, School of Engineering, Faculty of Engineering and Built Environment,
The University of Newcastle, Callaghan, NSW 2308, Australia*

KEYWORDS

Fatigue
Damage
Composite
Laminate
Fibre
Hybrid
Systems approach
Complexity
Mechanisms
Relative damage sensitivity
factor

ABSTRACT

Hybrid laminates consisting of woven glass fabric/epoxy composite plies and woven carbon fabric/epoxy composite plies are studied for fatigue damage and residual strength. A theoretical framework based on the systems approach is proposed as a guide to deal with the complexity involving uncertainties and a large number of variables in the hybrid composite system. A relative damage sensitivity factor was developed for quantitative comparisons between non-hybrid and hybrid composites, which may be useful for developing inexpensive composites with low damage sensitivity. Hypotheses derived from the theoretical framework were tested and verified using evidence from both micro- and macro-scopic damage patterns. The first hypothesis was that the difference between two different sets of properties produces shear stress in interface between carbon fibre reinforced plastics (CRP) and glass fibre reinforced plastics (GRP), and eventually become a source for CRP/GRP interfacial delamination or longitudinal cracking. The second hypothesis was that inter-fibre bundle delamination occurs more severely to CRP sub-system than GRP sub-system.

© 2013 DEStech Publications, Inc. All rights reserved.

1. INTRODUCTION

Composite is a structure consisting of two or more constituents having interfaces. It has been widely used as laminates in the aerospace industry and to a lesser extent in the automotive industry. Numerous research studies have been conducted to improve the behavior of composites under various loading conditions. They have shown that the composites made of one type of fibre reinforcement can be further improved by hybridizing for the optimum performance [1,2]. The hybrid laminates may be designed with two or more different types of fibre reinforcement. They are usually used when combination of properties of different types of fibres is required or when longitudinal as well as lateral mechanical performances are to be achieved [2,3]. Cost reduction of composite can also be achieved by incorporating laminates of low-cost but high performance fibres without

much reduction of the mechanical properties of the original composite [4]. Hybrid laminates reinforced with glass and carbon fibres have indeed been found to be useful in practice, especially in automotive and aerospace industries [5–7]. The recent structural applications of hybrid composites have been even more extended by focusing efforts on energy reduction since the glass and carbon fibre reinforced polymer matrix proved to be significantly effective [9].

As the engineering structures are frequently subjected to fatigue loading, the fatigue analysis plays an important role in the design of structural components. The fatigue in composites has been recognized as a complex phenomenon compared to that of monolithic-materials. There have been numerous studies investigating the fatigue performance of glass/epoxy, carbon/epoxy, and their hybrid composites for the effect of cyclic loading on residual properties [10–20]. However, most of them have focused on non-hybrid composites such as unidirectional, multidirectional, and woven fabric, composites. Ozturk and Moore [16] investigated the tensile fatigue behavior of woven carbon/carbon laminates

[†]Part of this article was presented in [3].

*Corresponding author. Email: haleh.allamehhaery@uon.edu.au

without notch as a function of stress level and found that, as a result of fatigue loading up to 106 cycles, residual strength and modulus in the on-axis direction were not significantly reduced.

Yoshioka and Seferis [19,20] conducted tension–tension fatigue tests on two different composite systems consisting of epoxy and phenolic matrices, respectively, reinforced with plain weave carbon fabric. They found that the residual strength of the epoxy laminates containing a hole after being fatigue damaged for a wide range of load cycles (1500 to 5×10^5) is even higher than undamaged ones. A mechanism responsible for the increase is such that the concentrated stress around a hole relieves and, as a result, is redistributed due to the fatigue damage. As such, a geometry variation has been found to be another factor affecting the residual strength.

Recently, Allameh Haery *et al.* [21] studied the effect of hybridization on tensile strength of laminates with a hole and found considerable benefits. This paper as continuation of the previous work [21] focuses on the effects of interply hybridization on residual tensile strength after fatigue damage for notched laminates. The main objective is two-fold - one was to develop a new theoretical framework for developing hybrid composites in general and the other was to test hypotheses derived from the theoretical framework.

2. FATIGUE MICRO-DAMAGE MECHANISMS IN WOVEN FABRIC REINFORCED COMPOSITES IN THE LITERATURE

It is important to understand the damage mechanisms for improving fatigue performance of composites. Various fatigue micro-damage mechanisms for woven glass fabric reinforced composites have been suggested in the literature. The sequence of events, however, has not been agreed among researchers in the absence of solid evidence or generality of its nature for fatigue crack initiation point. Tanimoto and Amijima [10] studied woven glass fabric reinforced polyester composites with glass volume fractions of 29, 40 and 54 % for micro-damage mechanisms without notch. They proposed three stages of damage process: (a) the first stage (up to 2% of its life span) was characterised such

that the number of cracks initiate and form perpendicular to loading direction in resin-rich phase near transverse fibre bundles (weft) and remain in the matrix but no significant decrease in static strength; (b) at the second stage (2 to 50% of its life span), the cracks propagate through resin matrix surrounding the transverse fibres up to the adjacent longitudinal fibres and, as a result, residual strength continuously decreases with the cyclic loading; and (c) at the third stage (50 to 100%), the rate of decrease in static strength is reduced until the final failure. The sequence of the three stages is illustrated in Figure 1.

Fujii and Amijima [11] investigated fatigue micro-damage behavior of the similar laminates with a glass volume fraction of 33%. They also proposed three different stages of damage process but with difference sequence of events: (a) the first stage (up to 10% of its life span) was delineated with the crack initiation within the weft bundle (cracking of which is perpendicular to loading direction)—crack density after this stage did not increase significantly; (b) in the second stage (10 to 98% of its life span), debonds between weft and warp were formed leading to meta-delaminations at cross-over points before the final failure (as the third stage). Pandita *et al.* [18] also investigated the similar composite with epoxy matrix for a glass volume fraction of 50% for the same topic. They proposed essentially the same sequence as those by Fujii and Amijima [11]. Further, Gao *et al.* [27] reported more meaningfully with evidence on carbon woven fabric reinforced polyimide with a fibre volume fraction of 60%. They observed that the crack initiation frequently took place in the weft bundle. Their finding appears to be in agreement with Fujii and Amijima [11] for the initiation. Nonetheless, there always seems to be uncertainty to some degree regarding the nature of micro-damage mechanism and crack initiation position.

3. A THEORETICAL FRAMEWORK FOR FATIGUE DAMAGE PROCESS

Understanding of the fatigue damage process is important for developing new composites. The sequence for fatigue damage mechanisms coupled with a relevant description

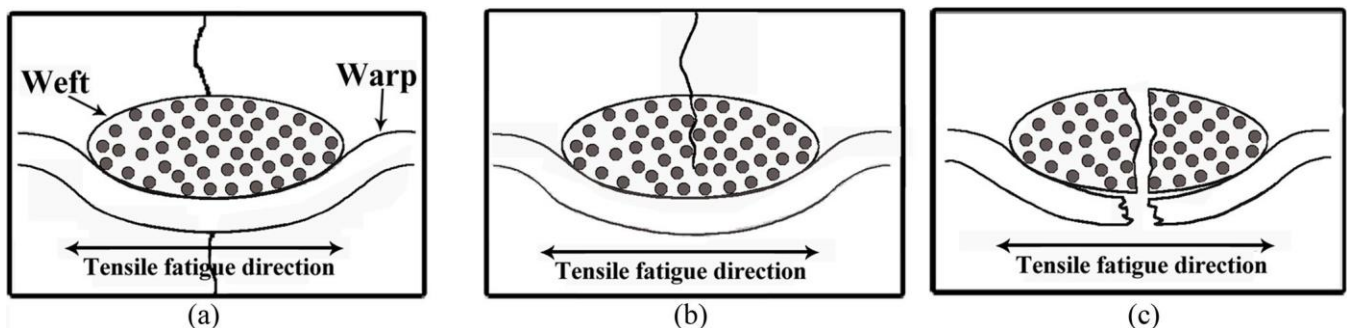


Figure 1. Schematic representation of the tensile fatigue damage development in laminated glass composite laminate: (a) first stage (cracks remain in the resin phase); (b) second stage (transverse crack in the bundle yarn); (c) final failure.

leading to the final failure is the core of the process for a series of events. Various experimental techniques including in-situ and/or post-damage observation using microscopes [22], x-radiography [13], image processing algorithm [15], acoustic emissions [18] or c-scan [12] may be useful in conjunction with the post-damage analysis for collecting direct information. However, it is difficult to observe internally hidden in-situ damage mechanisms and its behaviour at a particular point does not necessarily represent all other points because of the inherent uncertainties originated from various sources such as in-homogeneity in both constituent materials and composite micro-structure due to the imperfect composite fabrication technology. For this reason, the post-damage analysis may be also useful for inferences of the damage mechanisms. More importantly, the facts based on the observations are about particular composite systems at a particular moment and therefore not necessarily applicable to other parts of composite system or other composite systems. For wider applications and better understanding, the post-damage analysis requires a theoretical framework for various interpretations and for navigating of collected/processed information towards the applications for improving design, performance, and optimized uses, of the composites in general. Most studies in the literature have focused on a limited number of parameters applicable to particular composites for fatigue damage let alone hybrid composites. Therefore, the following theoretical framework is proposed here for extending usefulness of limited data and observational facts.

3.1. Complexity and Systems Approach

The fatigue process of a monolithic-material as a constituent of a composite consists of commonly two stages—namely crack initiation and propagation prior to the final failure. The crack initiation is affected by a set of properties and is susceptible to the inherent defects in the material while the crack propagation is affected by another set of properties. Further, when different constituent materials are combined for a composite system, the fatigue behaviour of a constituent material is affected by other constituent material properties such as stiffness, strength, and relativity between properties of a composite system. The relativity is dependent on how much they are different from each other. The constituent materials as system elements within a composite system constrain each other during the damage process. Also the fatigue damage behaviour is affected by the interface conditions (e.g. bonding) between different materials [12]. They are further affected by large scale design factors such as geometrical variation (e.g. notch) and hybridization. The theoretical stress analysis and failure criteria [34,35] for the geometrical variation may be useful but their applications are limited to the cases of certain geometries prior to the fatigue damage.

When composites are hybridized for inter-ply of a laminate using woven fabric, three or more different constituent materials may be used, e.g. carbon fibre, glass fibre, and epoxy. For three different constituent materials, the locations of possible fatigue crack initiation points include: (a) matrix, (b) interface between fibre filaments within glass fibre bundle, (c) interface between fibre filaments within carbon fibre bundle (d) interface between matrix and glass fibre bundle, (e) interface between matrix and carbon fibre bundle, (f) glass fibre filament, (g) carbon fibre filament, (h) cross-over point for meta-delamination for carbon fabric, (i) cross-over point meta-delamination for glass fabric, (j) interface between glass-glass composite plies, (k) interface between carbon-carbon composite plies, and (l) interface between glass-carbon composite plies. Thus, twelve different locations are possible for a crack to initiate and propagate or to link with other crack grown from other locations. Accordingly, the number (N_f) of possibilities for different sequential patterns of damage events in terms of, at least, damage initiation locations are given by:

$$N_f = n_f! \quad (1)$$

where n_f is the number of possible locations of fatigue crack initiation. For example, $N_f = 12! = 479,001,600$ for the inter-ply hybrid laminates described above. If they are non-hybrid laminates e.g. glass reinforced plastic (GRP) laminates, the locations listed above, '(a)', '(b)', '(d)', '(f)', '(h)', and '(j)' may be applicable and the number of possible locations for initiation reduces to 720 (= 6!). Accordingly, a mechanism associated with a crack initiation within a transverse glass fibre bundle suggested by Pandita *et al.* [18] or Fujii and Amijima [11], or another similar mechanism associated with the initiation within resin-rich area outside glass fibre bundles (see Figure 1) suggested by Tanimoto and Amijima [10] in a deterministic manner may be one of 720 possible ones.

The way to reduce the complexity due to the uncertainty with a large number of possibilities for hybrid composites may be based on the systems approach. In general, there may be two different systems i.e. open and closed systems [25]. The open system consisting of input and output with system elements may be useful for understanding of the hybrid composite system damage. We may consider different size scale sub-systems within the open system, given that a large scale system behaviour in terms of damage (or cracking) is caused by small scale system behaviours. A small scale system behaviour is in turn caused by even smaller system behaviours. Thus, output from a small system constitutes input of a large system. Output from a large system is the manifestation of what has most likely taken place in the small scale system. Thus, as the system scale size becomes larger and larger, the uncertainty in damage behaviour decreases and accordingly stochastic process turns into more and more deterministic process. A hybrid composite is a relatively large system con-

sisting of sub-systems including interfaces. Each sub-system consists of constituent materials as system elements. Each constituent material may be regarded as the smallest system consisting of defects responsible for damage origin (or initiation). For example, a GRP laminate is one sub-system consisting of glass fibres, matrix and interfaces, and a carbon reinforced plastic (CRP) laminate is another sub-system consisting of carbon fibres, matrix and interfaces, for a hybrid system consisting of CRP laminates, GRP laminates (to be referred to as 'CGRP hybrid system') and interfaces. A certain type of loading (e.g. static loading, fatigue loading) or geometry variation (e.g. due to a notch) is an input to the system and damage is an output. One of the keys to understanding of hybrid system damage behaviour is to find differences between sub-systems provided sub-systems are well defined. The major differences may be found near or at interface zone between two different sub-composite systems. The reason is that the damage behaviour near or at interface zone is influenced by the difference between two sub-composite systems and hence is different from those of sub-composite systems.

In the systems approach, the identification of damage pattern(s), if any, according to crack initiation location at least and cracking direction for inferences of mechanisms in relation with expected behaviour may be useful. The main reason for this is that the damage pattern at a larger scale represents an output of the most probable damage mechanisms at a smaller scale. Therefore, the description of microscopic damage mechanisms without identification of the damage pattern at a larger scale may be not much useful.

The damage patterns generated by fatigue loading for brittle materials such as CRP may be expected to be similar to those by static loading. The reasons are that: (a) similar stress distributions are created by similar geometric variations; (b) the damage patterns are very closely associated with crack initiation sites and crack propagation; (c) the crack initiation sites and crack propagation are created by stress concentration caused by micro-and macroscopic-variation in geometry. Also, the strain at failure is expected to be similar as reported by Kim and Zhang [26]. The similarities in damage between static and fatigue loading are useful not only for reduction of complexity but also for theoretical formulation of residual properties [26].

The damage as system output created as a result of fatigue loading may be quantified in terms of stiffness or residual strength [26]. Two sets of constituent material properties for respective pre-and post- fatigue damages may be used as the characteristics of a composite system. The number of possible relative conditions for the initial constituent material properties of interest prior to damage ($N_{E,pr}$) can be worked out as:

$$(N_{E,pr}) = n_e! \times N \quad (2)$$

where N is a number of different properties, n_e is a number

of different constituent materials. For example, if the hybrid system consisting of three different materials are used ($N_{E,pr}$) is found to be 18 ($= 3! \times 3$) for three different properties. An example of relative conditions applicable prior to fatigue damage is given by:

$$E_E < E_G < E_C \quad (3)$$

$$\sigma_{EU} < \sigma_{GU} < \sigma_{CU} \quad (4)$$

$$\varepsilon_{CU} < \varepsilon_U < \varepsilon_{EU} \quad (5)$$

where E_C = stiffness of carbon fibre, E_G = stiffness of glass fibre, E_E = stiffness of epoxy, σ_{Cu} = ultimate stress of carbon fibre, σ_{Eu} = ultimate stress of epoxy, σ_{Gu} = ultimate stress of glass fibre, σ_{Gu} = ultimate strain of glass fibre, σ_{Cu} = ultimate strain of carbon fibre, and σ_{Eu} = ultimate strain of epoxy.

If we consider two sub-composite systems (i.e. CRP-sub system and GRP-sub system in the current work), a number of different constituent materials (n_e) in Equation (2) is replaced with a number of different sub-systems, for the number of possible relative conditions ($N_{E,pr}$). An example relative condition applicable prior to fatigue damage is

$$E_{GRP} < E_{CRP} \quad (6)$$

$$\sigma_{GRPU} < \sigma_{CRPU} \quad (7)$$

$$\varepsilon_{CRPU} < \varepsilon_{GRPU} \quad (8)$$

$$\nu_{CRP} < \nu_{CRP} \quad (9)$$

where E , σ , ε , and ν denote stiffness, stress, strain and Poisson's ratio, respectively, and capital subscripts indicate different sub-systems, and subscript u stands for 'ultimate'. Consequently, the total number of possible damage patterns (N_T) characterized by crack initiation location, property numbers, and material/sub-system numbers leading to the residual properties is found to be

$$N_T = N_f \times (N_{E,pr}) = n_f! \times N \times n_e! \quad (10)$$

Accordingly, the total number of relative damage conditions for the hybrid system (N_T), in general, is calculated to be $8.94^9 (= 479,001,600 \times 3 \times 6)$ when three constituent materials are considered, or it is $5.74^9 (= 479,001,600 \times 2 \times 6)$ when two sub-composite systems instead of materials are considered. Thus, the residual static properties, in general, are the ones obtained under one of the possible relative material property conditions. The possible number of combinations for residual property inequalities after fatigue ($N_{E,po}$) would be equal to those before fatigue ($N_{E,pr}$):

$$(N_{E,po}) = (N_{E,pr}) = n_e! \times N \quad (11)$$

Therefore, the total number of possible damage patterns (N_T) after fatigue in terms crack initiation site, number of properties, and number of material constituents/sub-systems is also equal to those prior to fatigue loading.

If a composite specimen has a geometrical variation (e.g. notch), the initial set of homogenous properties turn into in-homogeneous ones as an output as the damage progresses under fatigue loading. As a result of damage, the properties at the maximum stress point on a specimen are different from those at any other points. The damage, thus, can be in general characterized by in-homogeneity distribution of resultant material properties at an appropriate scale. A hybrid composite system prior to fatigue damage may be regarded as being homogenous including woven fabric at an appropriate scale, (knowing that a woven fabric is not homogeneous, for example, at a smaller scale because a set of properties at a cross-over point of woven fabric are different from those of other points) but, as the damage progresses, in-homogeneity is created and more and more widely distributed. Such conditions given by Equations (3) to (5) or (6) to (9), thus, will be rearranged depending on the location at a specimen. The initial strength following the fatigue damage is then altered for the resultant residual properties for a given geometry condition.

3.2. Relative Damage Sensitivity Factor for Comparing Two Different Composite Systems[‡]

Design of complex (or hybrid) composites for improvement can be an evolutionary process unless a creative process is adopted. In other words, existing composites may be modified and compared in a process of decision making. If the modification is made by replacing part of an existing composite with new one, comparisons should be made. Two different ways for making comparisons may be considered. One way is to compare damage results (e.g. residual strength) directly from two different composite systems for absolute damage. The other way is to find, and compare for, a relative change rate of damage in its own composite system for the common variation of geometry or/and loading conditions between two different composite systems. It would be, however, implicit and its benefit would not much be known without a quantitative description despite the fact that such comparisons may be useful for a low cost hybrid composite development. The following procedure is proposed for a relative damage sensitivity factor which will be useful in such a situation.

If we choose and consider two particular composite systems for comparing residual properties, we need to define the residual (structural) strength reduction rate or increase rate—for conventional composite system (e.g. GRP system)

(R_o), and hybrid composite system (e.g. CGRP hybrid system) as a large new system (R_n):

$$R_o = \frac{S_{ng}^{oc}}{S_{og}^{oc}} \quad (12)$$

and

$$R_n = \frac{S_{ng}^{nc}}{S_{og}^{nc}} \quad (13)$$

where S_{ng}^{oc} is an apparent residual strength for new geometry (e.g. due to a different notch size or creation of a hole) and original (or conventional) composite system, S_{og}^{oc} is an apparent residual strength for original geometry and original composite system, S_{ng}^{nc} is an apparent residual strength for new geometry and new composite system (or hybrid), and S_{og}^{nc} is an apparent residual strength for original geometry and new composite system.

It is possible for the two different composite systems i.e. original (or conventional) composite system (CCS) and new hybrid system (NHS) to have the following cases as a result of damage:

Case 1; $R_n > 1$, $R_o > 1$, $R_n > R_o$ —both CCS and NHS strengthened,

Case 2; $R_n > 1$, $R_o > 1$, $R_n < R_o$ —both CCS and NHS strengthened,

Case 3; $R_n > 1$, $R_o < 1$ —CCS weakened but NHS strengthened,

Case 4; $R_n < 1$, $R_o > 1$ —CCS strengthened but NHS weakened,

Case 5; $R_n < 1$, $R_o < 1$, $R_n < R_o$ —both two composite systems weakened, and

Case 6; $R_n < 1$, $R_o < 1$, $R_n > R_o$ —both two composite systems weakened.

For relative damage sensitivity for two different composite systems (CCS and NHS), the following factor, q , (this factor will be referred to as “relative damage sensitivity factor”) can be found to be applicable for all the possible Cases:

$$q = \frac{R_o}{R_n} \quad (14)$$

According to Equation (14), q is found as follows: $q < 1$ for Case 1; $q > 1$ for Case 2; $q < 1$ for Case 3; $q > 1$ for Case 4; $q > 1$ for Case 5; and $q < 1$ for Case 6. In general, q approaches one if no difference in properties of both composite systems is caused by any change in input (e.g. fatigue loading), or $q < 1$ if a NHS is less sensitive to damage than CCS,

[‡]The relative damage sensitivity factor has been reformulated into a different form as the previous one was inaccurately done for strengthening cases in reference [31].

or $q > 1$ if NHS is more sensitive to damage than CCS. For developing a new composite system, the smaller q the better. Thus, Equation (14) is a generalized criterion indicating a relative damage sensitivity useful for comparing two different composite systems for the same variation of geometry or/and loading condition. Equations (12)–(14) may be applicable to static cases also in the absence of fatigue damage. If the residual strength (S) is replaced with the residual stiffness, the same principle is applicable for the residual stiffness comparison for two different systems.

4. EXPERIMENTAL DETAILS

The experimental details given here are adopted from the previous papers [21,31] for part of the current experimental work to provide self-sufficient information.

4.1. Structure of Woven Fabric

The structure of a woven fabric is characterized by the following parameters: inter-crimp length, bundle width at crimp region, crimping length, and bundle thickness. The inter-crimp length is the distance between two neighboring crimps while the crimping length is the one for the undulating region. The bundle width at the crimp is the one for the transverse bundle, and the bundle thickness is the average thickness of the longitudinal (or horizontal) bundles [27]. The characteristic measurements for the architecture of carbon and glass woven fabric are shown in Table 1.

4.2. Specimen Preparation

Plain weave C-glass fibre fabric or plain weave 3K-carbon fibre fabric were used for fabricating CGRP plies with a matrix of D.E.R. 331 epoxy resin which is uniformly mixed with a Jointmine hardener, type (905-3S), with a 2:1 ratio by weight. The laminates consisting of twelve plain weave plies were fabricated with the hand lay-up method for both glass reinforced composite (GRP) system as the control and CGRP hybrid system for specimen dimensions given in Figure 2.

The CGRP hybrid system manufactured consisted of six GRP plies in the middle between CRP plies at top and bot-

Table 1. Characteristic Measurements for Fibre Architecture of Carbon and Glass Woven Fabric.

	Carbon Fibre	Glass Fibre
Inter-crimp Length (mm)		
Average	3.70	2.860
CV (%)	1.338	2.084
n	9	9
Bundle Width at Crimp Region (mm)		
Average	1.739	1.942
CV (%)	2.787	3.073
n	9	9
Crimping Length (mm)		
Average	2.425	2.452
CV (%)	2.950	3.929
n	9	9
Bundle Thickness (mm)		
Average	0.109	0.104
CV (%)	1.79	3.56
n	9	9

1. CV is the coefficient of variation

2. n is the number of specimens

tom symmetrically. The outer CRP plies are intended for a relatively high tensile strength and stiffness but low fracture strain while inner GRP plies are for a relatively low cost and thermal conductivity but for high impact strength [28]. The properties of woven fabric C-glass and woven fabric 3K-carbon plies used here were taken from the previous studies by Zahari *et al.* [29] and Allameh Haery [21] are given in Table 2. The measured volume fractions were 51% for glass fibre in GRP, 66% for carbon fibre in CRP, and the volume fraction of both fibres in hybrid CGRP is 59%.

A symmetrical stacking sequence, $[0/90]_{3s}$ was chosen for both GRP and CGRP hybrid systems by considering warp as 0° and weft as 90° directions. The specimens, 210 mm long, 40 mm wide, and 3 mm thick, for fatigue tensile tests were cut from 250×350 mm plates using a CNC tooling machine. A circular hole with a diameter of 5 mm or 10 mm was drilled at the center of each specimen to give a notch effect. Figure 2.

4.3. Mechanical Testing and Damage Examination

The manufactured specimens were loaded for fatigue

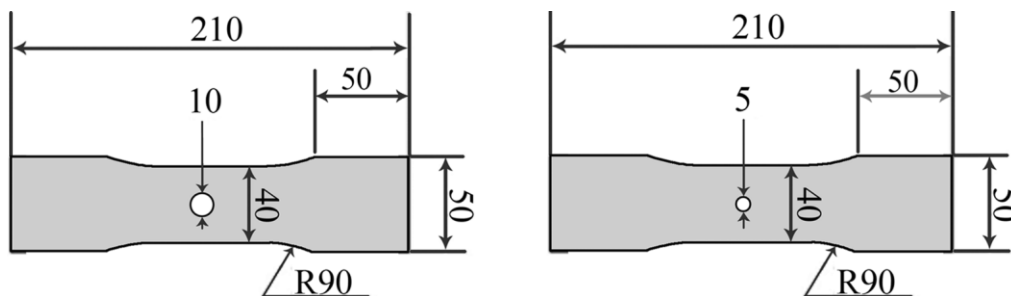


Figure 2. Specimens used for two different hole sizes of 5 mm and 10 mm.

damage using an Instron 8802 servo-hydraulic testing machine. A constant crosshead speed of 1 mm/min was chosen for the static tensile test at room temperature. For tension-tension fatigue tests, two load ratios (R = minimum load/maximum load), 0.1 and 0.25, with a sinusoidal frequency of 10 Hz, were also chosen. The maximum load for the fatigue was fixed to be a 70% of ultimate tensile load for each composite system (i.e. control GRP and CGRP hybrid). Each fatigue testing was stopped at 4×10^4 cycles for a subsequent static tensile test for measuring the residual strength. The number of cycles (4×10^4) was chosen considering that it is within a range of some beneficial effects which are expected due to the stress redistribution for similar composite systems in the literature [20]. At least five specimens were tested for each case.

For all the microscopic examinations, a position approximately 10 mm above or below a straight line crossing the minimum ligament section of the specimen was taken to view thickness area surface. Loading of each specimen shown in all the images is in the horizontal direction.

5. RESULTS AND DISCUSSION

5.1. Residual Strength Prior to Fatigue Damage

The ultimate tensile loads without fatigue damage for control GRP system and CGRP hybrid system obtained previously [21] are given in Table 3. It is seen that the apparent strength decreases as expected with increasing hole size from 5 mm to 10 mm in both GRP and CGRP hybrid systems. The reduction rate (R_o) due to the hole size increase for GRP system [see Equation (12) for $R_o = S_{ng}^{oc}/S_{og}^{oc}$] is found to be 24% while R_n [see Equation (13)] is found to be 10% for CGRP hybrid system. As a result, the relative damage sensitivity factor (q) becomes 0.844 [< 1 —see Equation (14)] indicating that damage in CGRP hybrid system is less sensitive than GRP system to the hole size increase.

Table 2. Mechanical Properties for C-glass/epoxy and 3k-carbon/epoxy Plies—Elastic Modulus for Warp Direction (E_{11}), Weft Direction (E_{22}), Poisson's Ratio (ν_{12}), Shear Modulus (G_{12}), Ultimate Strength for Warp Direction (σ_1^T)ult, Weft Direction (σ_2^T)ult, and Shear Strength (σ_{12})ult.

Properties	C-glass/epoxy (200 g/m ²)	3k-carbon/epoxy (200 g/m ²)
E_{11}	12.246 (GPa)	68.95 (GPa)
E_{22}	11.339 (GPa)	65.22 (GPa)
ν_{12}	0.158	0.0494
G_{12}	2.340 (GPa)	6.550 (GPa)
(σ_1^T) ult	181.552 (MPa)	454.364 (MPa)
(σ_2^T) ult	172.462 (MPa)	428.164 (MPa)
(σ_{12}) ult	39.626 (MPa)	105.489 (MPa)

Table 3. Average Ultimate Tensile Loads Obtained from Static Tensile Tests (without fatigue damage). The Reduction Rates Due to Hole Size Change from 5 to 10 mm are Given in Parenthesis.

	GRP System		CGRP Hybrid System	
	5 mm hole	10 mm hole	5 mm hole	10 mm hole
Ultimate Tensile Load (kN)	11.86	8.98 ($R_o = 76\%$)	21.48	19.32 ($R_n = 90\%$) $q = 0.844$

5.2. Residual Strength After Fatigue Damage

A summary of ultimate tensile loads obtained at two different load ratios for two different hole sizes and two different composite systems is given in Table 4. Each value in parenthesis is a reduction rate (R_o or R_n) due to fatigue damage with reference to the corresponding static ultimate load. The load ratios and hole sizes were intended to provide a wide range of different damage conditions.

5.3. Hypotheses and Damage Examination for CGRP Hybrid Systems

Some complexity in deformation leading to damage may be caused by the woven fabric cross-over points. The expected deformation, though, causing damage due to differences between constituent materials may be useful for setting up a hypothesis. An illustration for the deformation is introduced in Figure 3. It may be similar to those of a non-hybrid laminate given by Desai and McGarry [30], and Shuler *et al.* [22] but is for more specific deformation and is different in relation with the hybrid composite system. The longitudinal tensile loading straightens the longitudinal fibre bundles and simultaneously the following events take place at around the cross-over point [Figure 3(a)]: (i) bending of transverse fibre bundles and increasing of contact pressure; (ii) bending of longitudinal fibre bundle (which is straightening); and (iii) increasing of distance between transverse and longitudinal fibre bundles along the longitudinal fibre bundle but decreasing along the transverse fibre bundle (due to the contact pressure and bending of transverse fibre bundle). The last event would create a source for delamination between longitudinal and transverse fibre bundles. The bending in the other events is accompanied by not only normal stress but also shear stress. The maximum bending of either longitudinal or transverse fibre bundle takes place at the cross over point. The shear stress is, therefore, likely responsible for the longitudinal cracking within a transverse fibre bundle or a longitudinal fibre bundle if happens. Otherwise, transverse cracking in transverse fibre bundle is expected due to either the principle stress in the longitudinal loading direction or a

Table 4. Average Ultimate Tensile Loads Obtained from Static Tensile Tests After Being Fatigue Damaged. The Strength Reduction Rates Due to Fatigue Damage are Given in Parenthesis.

	GRP System		CGRP Hybrid System	
	5 mm hole	10 mm hole	5 mm hole	10 mm hole
Ultimate Tensile load (kN) ($R = 0.1$)	10.18 ($R_0 = 85.9\%$)	7.55 ($R_0 = 84.1\%$)	18.53 ($R_n = 86.3\%$) $q = 0.995$	15.14 ($R_n = 88.3\%$) $q = 1.074$
Ultimate Tensile load (kN) ($R = 0.25$)	9.12 ($R_0 = 77.0\%$)	6.54 ($R_0 = 72.9\%$)	15.80 ($R_n = 73.5\%$) $q = 1.048$	13.40 ($R_n = 69.3\%$) $q = 1.052$

splitting force when width is much larger than thickness of transverse fibre bundle (weft).

When GRP sub-system is interfaced with CRP sub-system for hybridization as illustrated in Figure 3(b), the following may be considered: the carbon fibre bundles are stronger and stiffer [see Inequalities (3) and (4)] but lower in Poisson's ratio than glass fibre bundles. The localized (bending and shear) deformation of longitudinal glass fibre bundles of GRP system near CRP ply is, thus, relatively compliant to the straightening of longitudinal carbon fibre bundles. The carbon fibre bundles of CRP system has hence more straightened than glass fibre bundles because their high stiffness as illustrated in Figure 3(b). Therefore, the bending with shear deformation (causing a longitudinal cracking) of the trans-

verse carbon fibre bundles would take place more near the interface than those far away and surrounded by CRP plies. More importantly, such compliant behaviour of longitudinal glass fibre bundles with respect to the longitudinal carbon fibre bundle produces a difference in transverse elongation between two dissimilar plies despite the external iso-strain loading. Also, more obviously the difference in Poisson's ratio between two different sub-composite systems (see Table 2) produces different internal force directions as illustrated in Figure 3(c)—a larger lateral contraction of glass fibre bundles and a relatively smaller lateral contraction of carbon fibre bundles. Accordingly, it can be hypothesized (to be referred to as the First Hypothesis) that the difference between two different sets of properties produces shear stress

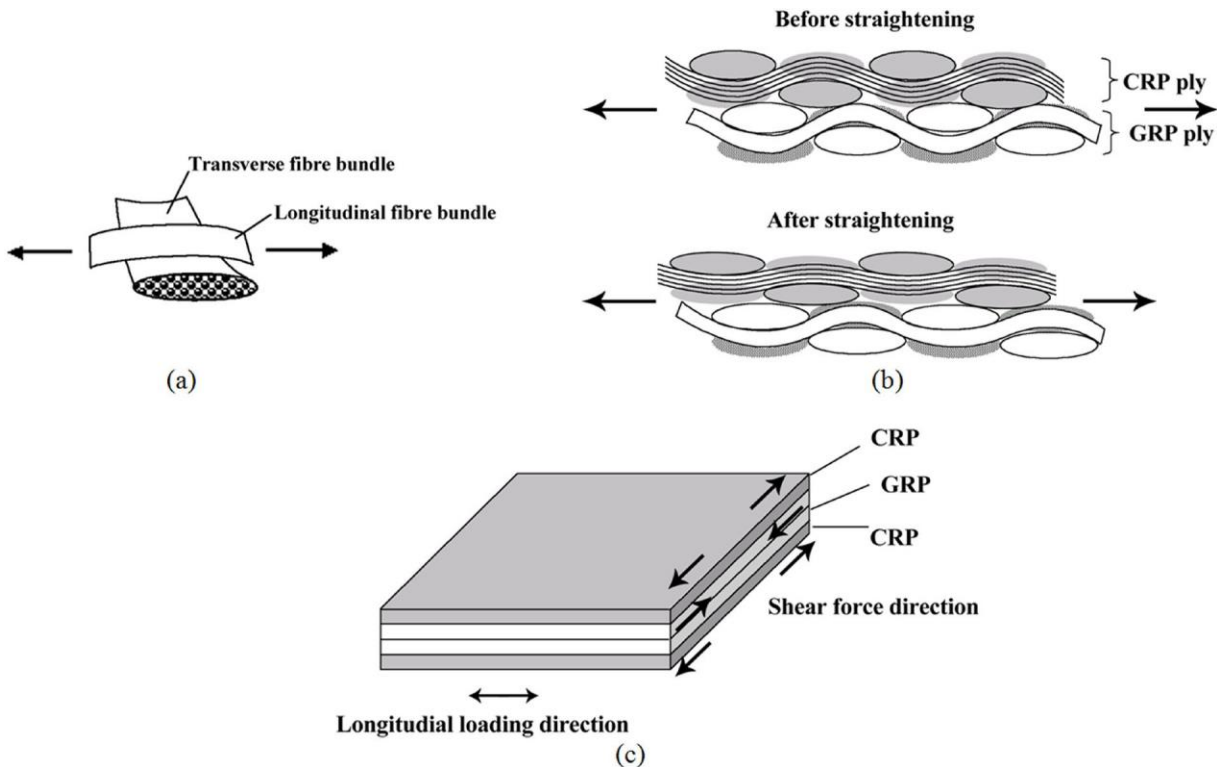


Figure 3. Schematic representation: (a) loading direction with cross-over point; (b) longitudinal and transverse fibre bundles near CRP/GRP interface before and after longitudinal tensile loading; and (c) shear force directions in CRP/GRP interface due to difference in Poisson's ratio. Note that the contact points between transverse fibre bundles in '(b)' and '(c)' are in reality at random.

in CRP/GRP interface, and eventually become a source for CRP/GRP interfacial delamination or longitudinal cracking. Further, two sub-systems can be compared at a large scale for general macroscopic fatigue damage with the benefit of discussion here and the initial material conditions given in Inequalities (3)–(5). Then, the likelihood that the three events, ‘(i)’, ‘(ii)’ and ‘(iii)’, described above take place more intensively in CRP sub-system than in GRP sub-system allowing us to hypothesize (to be referred to as the Second Hypothesis) that inter-fibre bundle delamination occurs more severely to CRP sub-system than GRP sub-system.

Fatigue micro-cracking near CRP/GRP interface observed are shown for some typical ones in Figure 4. The dashed lines and dotted lines were superimposed on images along cracks indicate crack locations for longitudinal and transverse cracks, respectively. Figure 4 shows a crack formed for an interfacial delamination and then branched out at the multiple points to turn into transverse cracking in the transverse carbon fibre bundle. Also, a long longitudinal crack in a longitudinal carbon fibre bundle cross-joined with one of the transverse cracks originated from the CRP/GRP interfacial delamination is seen. The crack branching tends to be in the transverse direction, indicating that it is affected by the longitudinal principle stress eventually. The crack opening magnitudes indicate that the crack branching is evidently emanated from the interfacial delamination. Therefore, the evidence here supports the First Hypothesis set up above.

However, the observations are not sufficient conditions but necessary for the possibility that the interface is the most probable damage initiation site constituting a macroscopic damage pattern.

At a larger scale, it is commonly observed that the inter-fibre bundle delamination occurs more in CRP sub-system than GRP sub-system as shown in Figure 5. The macroscopic damage pattern along with the micro-cracking (Figure 4) appears to be sufficient to support both the First and Second

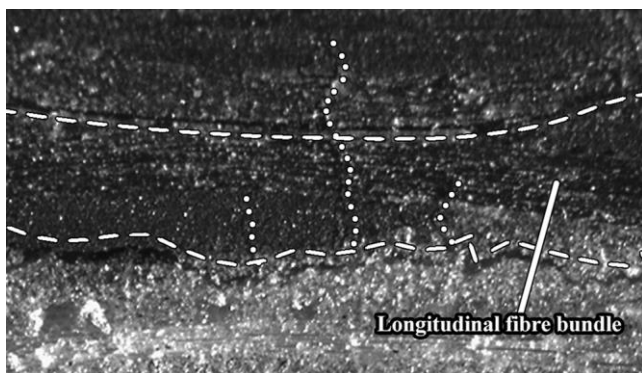


Figure 4. Damage near CRP/GRP interface with transverse cracking in a longitudinal carbon fibre bundle, and longitudinal cracking near GRP/CRP interface causing cross-over point delamination near GRP/CRP interface. The dashed and dotted lines indicate longitudinal and transverse cracking, respectively [31].

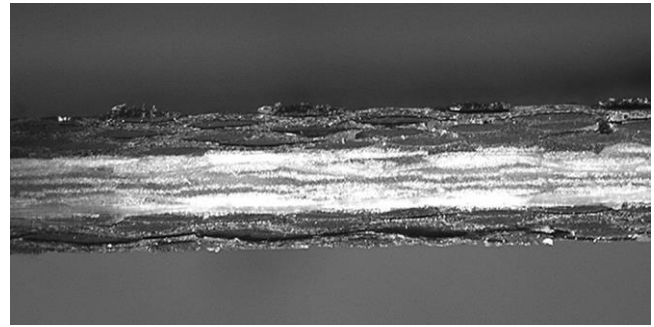


Figure 5. Inter-fibre bundle delamination at a large scale on thickness area of test specimen with a hole diameter of 5 mm after the fatigue damage at $R = 0.1$. (The inter-fibre bundle delamination appears as the darkest colour and gaps in contrast with undamaged CRP plies) [31].

Hypotheses. Figure 6 shows the macroscopic damage pattern under static loading. It appears similar to that under fatigue loading (Figure 5) to support the similarities between static and fatigue loading discussed under the theoretical framework.

5.4. Other Patterns of Micro-damage

Other patterns of micro-damage in terms of crack initiation location and cracking direction were observed and summarised in Figure 7. As expected and discussed under Section 3, many different patterns were found even though some of those were not eventuated for observable macroscopic damage patterns. They include: transverse cracking initiated from delamination [Figure 7(a), (b)]; inter-ply delamination [Figure 7(c)]; longitudinal crack in transverse carbon fibre bundle [Figure 7(d)]; cavity in transverse carbon fibre bundle [Figure 7(e)]; GRP/CRP interface delamination and transverse cracking [Figure 7(f)]; cavity in transverse glass fibre bundle and longitudinal cracking [Figure 7(g)]; transverse cracking between two cavities in transverse glass fibre bundles [Figure 7(h)]; transverse cracking through both transverse and longitudinal fibre bundles [Figure 7(i)]; transverse cracking originated from interface [Figure 7(j)]; and longitudinal cracking in transverse glass fibre bundle [Figure 7(k)]. The damage initiation locations discussed un-

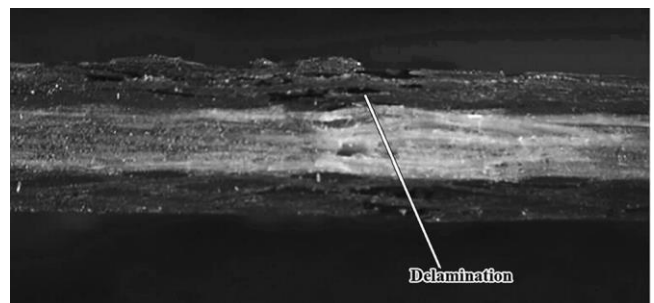


Figure 6. Inter-fibre bundle delamination at a large scale on thickness area of test specimen with a hole diameter of 10 mm.

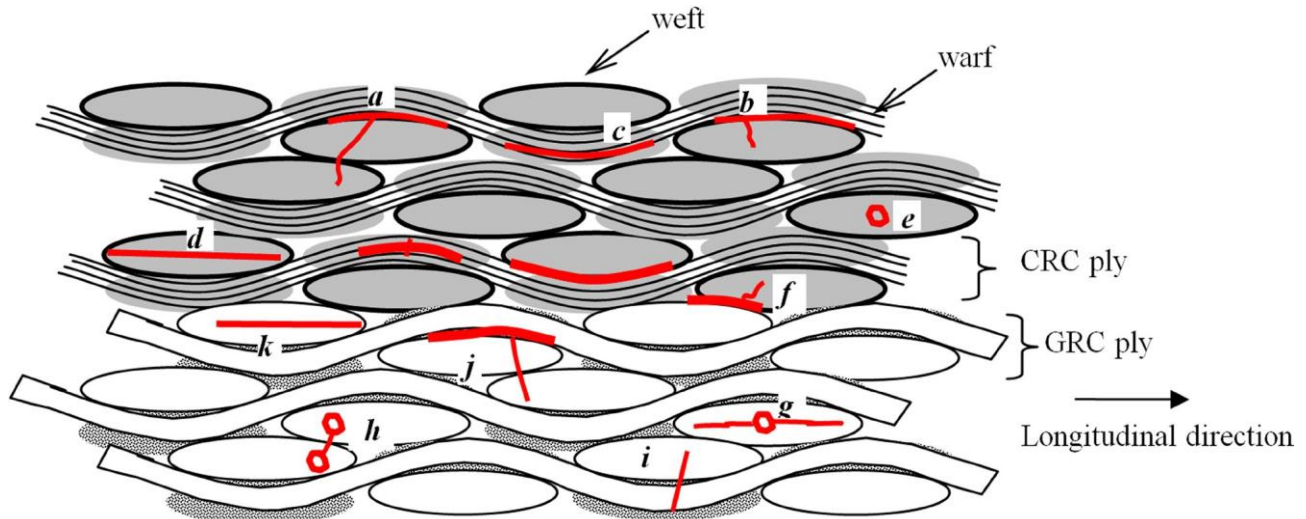


Figure 6. Schematic summary of various fatigue damage patterns in terms of crack initiation location and cracking direction in CGRP hybrid: (a)-(b) transverse cracking initiated from delamination; (c) inter-ply delamination; (d) longitudinal crack in transverse carbon fibre bundle; (e) cavity in transverse carbon fibre bundle; (f) GRP/CRP interface delamination and transverse cracking; (g) cavity in transverse glass fibre bundle and longitudinal cracking; (h) transverse cracking between two cavities in transverse glass fibre bundles; (i) transverse cracking through both transverse and longitudinal fibre bundles; (j) transverse cracking originated from interface; and (k) longitudinal cracking in transverse glass fibre bundle.

der Section 3 appears to be in line with these observations although some smaller scale ones were not confirmed (e.g. initiation within fibre filament).

6. CONCLUSIONS

- A theoretical framework is proposed as a guide to deal with the complexity involving uncertainties and a large number of variables in the hybrid composite systems.
- A relative damage sensitivity factor has been developed for the quantitative comparison between non-hybrid and hybrid composite systems.
- New damage mechanisms of hybrid laminates due to the dissimilarity between GRP and CRP systems were hypothesized and tested to be valid with the evidence based on macroscopic and microscopic examinations.
- The most probable initiation site of micro-fatigue damage mechanisms has been deduced.

ACKNOWLEDGEMENTS

The authors gratefully acknowledge the financial support for UNIPRS and UNRS from the University of Newcastle.

REFERENCES

- [1] Pandya, K. S., Ch, V., and N. K., N., "Hybrid composites made of carbon and glass woven fabrics under quasi-static loading," *Materials & Design*, 32(7), 4094–4099 (2011). <http://dx.doi.org/10.1016/j.matdes.2011.03.003>
- [2] Daniel, I. M., and Ishai, O., *Engineering mechanics of composite materials*. Oxford University Press, New York and Oxford (1994).
- [3] Gururaja, M. N., and Hari Rao, A. N., "A review on recent appli-

cations and future prospectus of hybrid composites," *International Journal of Soft Computing and Engineering (IJSCE)*, 1(6), 352–355 (2012).

- [4] Rotem, A., "Residual strength after fatigue loading," *International Journal of Fatigue*, 10(1), 27–31 (1988). [http://dx.doi.org/10.1016/0142-1123\(88\)90018-7](http://dx.doi.org/10.1016/0142-1123(88)90018-7)
- [5] Phua, Y. J., Mohd Ishak, Z. A., and Senawi, R., "Injection molded short glass and carbon fibers reinforced polycarbonate hybrid composites: Effects of fiber loading," *Journal of Reinforced Plastics and Composites*, 29(17), 2592–2603 (2010). <http://dx.doi.org/10.1177/0731684409358282>
- [6] Zhang, J., Chaisombat, K., He, S. *et al.*, "Hybrid composite laminates reinforced with glass/carbon woven fabrics for lightweight load bearing structures," *Materials & Design*, 36(0), 75–80 (2012). <http://dx.doi.org/10.1016/j.matdes.2011.11.006>
- [7] Jeon, K.-W., Shin, K.-B., and Kim, J.-S., "Evaluation of tension-compression and tension-tension fatigue life of woven fabric glass/epoxy laminate composites used in railway vehicle," *International Journal of Precision Engineering and Manufacturing*, 12(5), 813–820 (2011). <http://dx.doi.org/10.1007/s12541-011-0108-6>
- [8] Summerscales, J., and Short, D., "Carbon fibre and glass fibre hybrid reinforced plastics," *Composites*, 9(3), 157–166 (1978). [http://dx.doi.org/10.1016/0010-4361\(78\)90341-5](http://dx.doi.org/10.1016/0010-4361(78)90341-5)
- [9] Das, S., *The cost of automotive polymer composites: a review and assessment of DOE's lightweight materials composites research*. Technical Information Center Oak Ridge Tennessee (2001).
- [10] Tanimoto, T., and Amijima, S., "Progressive nature of fatigue damage of glass fiber reinforced plastics," *Journal of Composite Materials*, 9(4), 380–390 (1975). [http://dx.doi.org/10.1016/0010-4361\(78\)90341-5](http://dx.doi.org/10.1016/0010-4361(78)90341-5)
- [11] Fujii, T., Amijima, S., and Okubo, K., "Microscopic fatigue processes in a plain-weave glass-fibre composite," *Composites Science and Technology*, 49(4), 327–333 (1993). [http://dx.doi.org/10.1016/0266-3538\(93\)90063-M](http://dx.doi.org/10.1016/0266-3538(93)90063-M)
- [12] Afaghi-Khatibi, A., Ye, L., and Mai, Y. W., "An experimental study of the influence of fibre-matrix interface on fatigue tensile strength of notched composite laminates," *Composites Part B: Engineering*, 32(4), 371–377 (2001). [http://dx.doi.org/10.1016/S1359-8368\(01\)00012-9](http://dx.doi.org/10.1016/S1359-8368(01)00012-9)
- [13] Dimant, R. A., Shercliff, H. R., and Beaumont, P. W. R., "Evalua-

- tion of a damage-mechanics approach to the modelling of notched strength in KFRP and GRP cross-ply laminates,” *Composites Science and Technology*, 62(2), 255–263 (2002). [http://dx.doi.org/10.1016/S0266-3538\(01\)00201-9](http://dx.doi.org/10.1016/S0266-3538(01)00201-9)
- [14] Goto, K., Furukawa, Y., Hatta, H. et al., “Fatigue behavior of 2D laminate C/C composites at room temperature,” *Composites Science and Technology*, 65(7–8), 1044–1051 (2005). <http://dx.doi.org/10.1016/j.compscitech.2004.09.031>
- [15] Ambu, R., Aymerich, F., and Bertolino, F., “Investigation of the effect of damage on the strength of notched composite laminates by digital image correlation,” *Journal of Strain Analysis for Engineering Design*, 40(5), 451–461 (2005). <http://dx.doi.org/10.1243/030932405X16106>
- [16] Ozturk, A., and Moore, R. E., “Tensile fatigue behaviour of tightly woven carbon/carbon composites,” *Composites*, 23(1), 39–46 (1992). [http://dx.doi.org/10.1016/0010-4361\(92\)90284-2](http://dx.doi.org/10.1016/0010-4361(92)90284-2)
- [17] Kawai, M., and Taniguchi, T., “Off-axis fatigue behavior of plain weave carbon/epoxy fabric laminates at room and high temperatures and its mechanical modeling,” *Composites Part A: Applied Science and Manufacturing*, 37(2), 243–256 (2006). <http://dx.doi.org/10.1016/j.compositesa.2005.07.003>
- [18] Pandita, S. D., Huysmans, G., Wevers, M. et al., “Tensile fatigue behaviour of glass plain-weave fabric composites in on- and off-axis directions,” *Composites Part A: Applied Science and Manufacturing*, 32(10), 1533–1539 (2001). [http://dx.doi.org/10.1016/S1359-835X\(01\)00053-7](http://dx.doi.org/10.1016/S1359-835X(01)00053-7)
- [19] Yoshioka, K., and Seferis, J. C., “V Tension-tension fatigue of resin transfer molding composites,” *International SAMPE Symposium and Exhibition (Proceedings)*, 46 I, 1079–1085.
- [20] Yoshioka, K., and Seferis, J. C., “Modeling of tensile fatigue damage in resin transfer molded woven carbon fabric composites,” *Composites Part A: Applied Science and Manufacturing*, 33(11), 1593–1601 (2002). [http://dx.doi.org/10.1016/S1359-835X\(02\)00109-4](http://dx.doi.org/10.1016/S1359-835X(02)00109-4)
- [21] Haery, H. A., Zahari, R., Kuntjoro, W. et al., “Tensile strength of notched woven fabric hybrid glass, carbon/epoxy composite laminates,” *Journal of Industrial Textiles*, (2012). <http://dx.doi.org/10.1177/1528083712456055>
- [22] Shuler, S. F., Holmes, J. W., Wu, X. et al., “Influence of loading frequency on the room-temperature fatigue of a carbon-fiber/SiC-matrix composite,” *Journal of the American Ceramic Society*, 76(9), 2327–2336 (1993). <http://dx.doi.org/10.1111/j.1151-2916.1993.tb07772.x>
- [23] Konish, H. J., and Whitney, J. M., “Approximate stresses in an orthotropic plate containing a circular hole,” *Journal of Composite Materials*, 9(2), 157–166 (1975). <http://dx.doi.org/10.1177/002199837500900206>
- [24] Awerbuch, J., and Madhukar, M. S., “Notched strength of composite laminates: predictions and experiments—A review,” *Journal of Reinforced Plastics and Composites*, 4(1), 3–159 (1985). <http://dx.doi.org/10.1177/073168448500400102>
- [25] Bertalanffy, L. V., *General system theory: foundations, development, applications*. George Braziller, (1968).
- [26] Kim, H. S., and Zhang, J., “Fatigue damage and life prediction of glass/vinyl ester composites,” *Journal of Reinforced Plastics and Composites*, 20(10), 834–848 (2001). <http://dx.doi.org/10.1177/073168401772678959>
- [27] Gao, F., Boniface, L., Ogin, S. L. et al., “Damage accumulation in woven-fabric CFRP laminates under tensile loading: Part I. Observations of damage accumulation,” *Composites Science and Technology*, 59(1), 123–136 (1999). [http://dx.doi.org/10.1016/S0266-3538\(97\)00231-5](http://dx.doi.org/10.1016/S0266-3538(97)00231-5)
- [28] Belingardi, G., Cavatorta, M. P., and Frasca, C., “Bending fatigue behavior of glass-carbon/epoxy hybrid composites,” *Composites Science and Technology*, 66(2), 222–232 (2006). <http://dx.doi.org/10.1016/j.compscitech.2005.04.031>
- [29] Zahari, R., Azmee, A. H., Mustapha, F. et al., “Prediction of progressive failure in woven glass/epoxy composite laminated panels,” *Jurnal Mekanikal*, 25, 80–91 (2008).
- [30] Desai, M. B., and McGarry, F. J., “Failure mechanisms in glass fibre reinforced plastics,” *ASTM Bulletin No. 239*, 76, (1959).
- [31] Haery, H. A., Kim, H. S., Zahari, R. et al., “Tensile strength of notched carbon/glass/epoxy hybrid composite laminates before and after fatigue loading,” *Journal of Industrial Textiles*, (2013).



Towards the Standardized Fabrication of CNT-Cement Based Composites for Structural Health Monitoring: An Application-Oriented Literature Survey

CARLO RAINIERI^{1,*}, D. GARGARO¹, YI SONG², GIOVANNI FABBROCINO¹, MARK J. SCHULZ² and VESSELIN SHANOV²

¹Structural and Geotechnical Dynamics Laboratory, Via Duca degli Abruzzi, 86039 Termoli, Italy

²Dept. of Mechanical Engineering, University of Cincinnati, 598 Rhodes Hall, Cincinnati, OH, USA 45221-0072

KEYWORDS

Carbon nanotubes
Plasma functionalization
Piezoresistivity
Self-sensing materials
Structural Health Monitoring
Embedded sensors
Structural neural systems

ABSTRACT

Civil structures always experience degradation phenomena over their lifespan. The recent advances in nanotechnology and sensing allow to monitor the behaviour of a structure, assess its performance and identify damage at an early stage. The availability of innovative, high performance sensing tools gives the opportunity to carry out maintenance actions in a timely manner, and this definitely enhances the structural reliability and safety. Several Structural Health Monitoring (SHM) applications reported in the literature are traditionally performed at a global level, with a limited number of sensors distributed over a relatively large area of a structure. The main drawback with those systems is related to the possibility of detecting only major damage conditions. A recent progress in the field of civil SHM concerns the development of dense sensor networks and innovative structural neural systems. The latter reproduce the structure and the function of the human nervous system and provides interesting opportunities to overcome the typical limitations of SHM related to the poor spatial resolution of measurements. Miniaturization and embedment are key requirements for the successful implementation of structural neural systems. In this context carbon nanotubes (CNTs) play an attractive role in the development of embedded sensors and smart structural materials. In fact, they can provide to traditional cement based materials both structural capability and measurable response to applied stresses, strains, cracks and other flaws. As a result, cement based sensors can be developed and embedded, ensuring the maximum compatibility and minimum interference with the hosting structure. In this paper investigations about CNT/cement composites and their self-sensing capabilities are summarized and critically revised. The literature review has provided the informative basis for a rational analysis of published experimental results and theoretical developments. The result is an application oriented survey of the literature about CNT/cement composites for SHM. It provides useful design criteria for the standardized fabrication of CNT/cement composites optimized for SHM applications in civil engineering. Specific attention is paid to the opportunities provided by new RF plasma technologies for the functionalization of CNTs in view of sensor development and SHM applications.

© 2013 DEStech Publications, Inc. All rights reserved.

1. INTRODUCTION

Structural Health Monitoring (SHM) aims at a timely detection of damage or degradation phenomena affecting

civil structures, so that condition-based maintenance can be carried out to improve structural reliability and safety, and reduce down time, inspection and maintenance costs. Traditional strategies for SHM act at a global level [1], with a limited number of sensors distributed over a relatively large area of a structure. As a consequence, only major damage conditions are detectable. The development of dense wire-

*Corresponding author. Tel: +39 0874 404-959; Fax: +39 0874 404-952;
Email: carlo.rainieri@unimol.it

less sensor networks has given an interesting opportunity to overcome this drawback. However, the conventional engineering practice in SHM is still based on adaption of commercial off-the-shelf sensing technologies to the particular application. This represents a limitation to the integration of sensors in the hosting structure. An innovative approach consists in the integrated design and implementation of SHM systems, so that the implemented system can tackle the issues related to hardware robustness, sensor embedment and operation autonomy (including energy harvesting) even through the fabrication of customized solutions. In this framework the development of innovative structural neural systems for integrated health management provides interesting opportunities [2].

Neural systems mimic the structure and the functions of the human nervous system. They are based on the deployment of a high number of distributed sensors and nerves, and the implementation of parallel data processing procedures [3]. A successful implementation of such systems requires sensor miniaturization and embedment. Sensor embedment provides several advantages, including detection capabilities in otherwise unreachable locations. However, structural modifications to physically accommodate SHM hardware are often necessary. For their compatibility with the hosting structure, smart materials with sensing capabilities have recently gained increasing attention.

Carbon nanotube (CNT) based sensors represent a very promising alternative in this context, since a “bottom-up” design approach can be adopted to develop embedded sensors and smart structural materials characterized by both structural capability and measurable response to applied stresses, strains, cracks and other flaws.

Carbon nanotubes, first discovered by Iijima [4] in 1991, consist of carbon atoms bonded in a helical crystalline structure. They may appear in the form of both single wall (SWCNT) and multi-wall (MWCNT) carbon nanotubes. From a geometrical point of view, SWCNTs consist of one cylindrical lattice of carbon atoms while MWCNTs are characterized by multiple helical concentrically positioned lattices. The wall of a SWCNT looks like a wrapped sheet of carbon atoms in a periodic hexagonal arrangement, with thickness equal to a single atom and diameters ranging from 0.4 to 3 nm; MWCNTs appear as multiple concentric SWCNTs, with diameters ranging from 1.4 to 100 nm. The length of CNTs can be up to centimeters, leading to very high aspect ratios.

CNTs are usually produced by a growth process, the so-called Chemical Vapor Deposition, in the presence of a catalyst. The synthesis is achieved under precisely controlled conditions.

From a mechanical standpoint, CNTs exhibit an elastic behavior, a very high stiffness ($E \approx 1$ TPa). Their hexagonally-bonded carbon honeycomb structure is responsible for the high tensile strength (20–60 GPa, with maximum strain up to 10%). The excellent mechanical properties represent

one of the reasons for the increasing interest towards CNTs. Most recent research studies have focused on the properties of CNT–polymer composites, but an increasing number of studies is focusing the attention on the potential of CNTs to enhance the performance and properties of ordinary Portland cement (OPC)-based binders. OPC is a hydraulic cement manufactured by burning together, in a kiln, a mixture of limestone and clay to form a clinker rich in calcium silicates. Then the clinker is grounded into a fine powder with a small proportion of gypsum that assists in regulating the rate of setting when the cement is mixed with water. OPC is a brittle material, characterized by low tensile strength. A wide variety of reinforcing fibers have been used in the last three decades to enhance the performance of the material under tensile load. They include steel, glass, carbon and synthetic materials. CNTs have the potential to become an effective reinforcement for OPC because bridging of micro-cracks can take advantage of the small dimensions (associated with high aspect ratio) and excellent mechanical properties of CNTs. The higher strength and stiffness (by order of magnitudes) of CNTs with respect to cement allow to share large loads from the cement matrix without the problem of tube fracture. Another advantage in using CNTs as reinforcement in cement is their low density (typically, less than 1500 kg/m³, about 80% lighter than steel). Thus, as a result of the high aspect ratio and low mass density, CNTs can be promising reinforcements for cement thanks to the large contact area and the reduced weight penalty.

From the electrical point of view, the orientation of the carbon atoms in the lattice structure of the tubes determines the classification of CNTs as conductors or semi-conductors. The high strength and stiffness and the high thermal and electrical conductivities of CNTs make them promising for the development of a lot of applications, including new, high performance smart composite materials for SHM [5]. In fact, the conductivity of CNTs leads to the enhancement of both conductivity and piezoresistive response of cement. In particular, the piezoresistive response is relevant to develop intrinsically self-sensing materials. In this perspective, CNT/cement composites become themselves sensors and they can be integrated into the hosting structures for civil SHM purposes. The piezoresistive (pressure-sensitive) response of CNT/cement composites is associated with complex electrical properties including resistance, capacitance and impedance characteristics. This is the result of two types of electrical conduction in CNT/cement composites: electronic conduction and ionic conduction. Electrons move freely within CNT, while ion movement mainly occurs in the pore solution of hydrated cement. Several research studies have been initiated in recent years aimed at the development and characterization of CNT based composites for a number of different applications. In particular, several studies have focused their attention on the definition of the most appropriate technique for the functionalization of carbon nanotubes in view of a certain application.

In this paper investigations about CNT/cement composites and their self-sensing capabilities are summarized and critically revised. The literature review has provided the informative basis for a rational analysis of published experimental results and theoretical developments. The result is an application-oriented survey of the literature about CNT/cement composites for SHM which provides useful design criteria for the standardized fabrication of CNT/cement composites optimized for SHM applications in civil engineering. Attention is focused on CNTs dispersed in cement paste; dispersion of CNTs in mortar or concrete is out of the scope of the paper, since additional issues, such as double percolation, arise as a consequence of the presence of aggregates [6]. Specific attention is devoted to the opportunities offered by new RF plasma technologies for the functionalization of CNTs in view of sensor development and SHM applications.

The paper is organized as follows. In Section 2, after the analysis of different options for CNT functionalization, innovative RF plasma technologies are briefly illustrated, pointing out the advantages that make them the ideal solution for the functionalization and dispersion of CNTs in cement paste. In Section 3 the recommended concentration of CNTs in cement paste and techniques for an effective dispersion of CNTs are discussed as a result of a literature review. Finally, additional issues concerning sensor fabrication are analyzed in Section 4. Even if these different aspects of fabrication of CNT/cement composites for SHM applications are separately discussed for the sake of clarity, they are strongly interdependent. As a final result, the present study is intended as a contribution to the definition of specific guidelines for a standardized fabrication of CNT/cement based sensors for SHM of civil structures.

2. APPROACHES TO CNT FUNCTIONALIZATION

Piezoresistivity is the property of CNT/cement composites that plays a fundamental role in the development of self-sensing materials. The electrical resistance of a piezoresistive material changes in response to the applied strain. The piezoresistive behavior of CNT/cement composites is a result of the dispersion of CNTs in the cement matrix. In fact, the high electrical conductivity of CNTs and the electrical tunneling through the matrix [7] increase the conductivity of the cement paste. The contribution of electrical tunneling mainly depends on the physical characteristics of CNTs, tunneling gap and conductive properties of the matrix filling this gap. The electrical resistance of the composite under applied loads changes as a result of both the changes in length and diameter of CNTs and, above all, in the tunneling gap. An effective dispersion of CNTs in the cement matrix is therefore critical to ensure the piezoresistive behavior of the composite.

Dispersion of CNTs in aqueous media is usually very difficult because of the strong Van der Waals forces, which cause agglomeration of CNTs. Dispersion technologies usually take advantage of both mechanical agitation and chemical treatment approaches [8]. The final selection of the dispersion methodology also depends on the required characteristics for the composite. Mechanical methods, such as ultrasonication, lead to a temporary dispersion of CNTs. Agglomeration of CNTs after sonication can be prevented by applying ultrasonication in combination with functionalization. This can consist of either chemical (covalent) or physical (non-covalent) treatments. In the first case functionalization of CNT surfaces is obtained by means of neat acids, such as H_2SO_4 and HNO_3 [5,9]. The acid treatment leads to a reaction between the oxygen atoms from the acids and the carbon atoms in those locations where the latter are more reactive, namely on the ends, curvatures and defects of the nanotubes [10]. As a result of the oxidation, negatively charged carboxylic groups are bonded to the CNT surface (covalent surface modification). The electrostatic repulsion force between the negative charges allows for the dispersion of CNTs in water without any surfactant and make them less prone to agglomeration. However, acid functionalization may cause structural defects. They have a detrimental effect on the electrical conductivity of the individual nanotubes [9]. Nevertheless, the better dispersion of the functionalized CNTs with respect to the untreated ones is still effective in determining an overall piezoresistive behavior of the composite. In particular, the achieved effective dispersion leads to a high sensitivity of the composite, since contact points and distances among tubes noticeably vary with the variation of applied force.

In the case of non-covalent treatment, the dispersing chemical groups are physically attached onto the CNT surface without disturbing the strong covalent bonds of the tube lattice [11]. Non-covalent functionalization is definitely attractive for those applications requiring a preservation of the properties and purity of CNTs. For this reason the combined use of surfactants and mechanical agitation has become fairly popular. However, surfactants might not represent an effective solution for the functionalization of CNTs when the piezoresistive response of the CNT/cement composite is of interest. A comparative assessment of the piezoresistive responses of two composites characterized by different fabrication methods is reported in [5], where the effect of surfactants and acid treatment on the sensitivity of the composite to the applied loads has been investigated in detail. In a first case, CNTs have been dispersed in water by covalent treatment. MWCNTs were treated with a mixture of 98% H_2SO_4 and 66% HNO_3 (3:1 ratio). Acid-treated MWCNTs were dispersed in water and then mixed with Portland cement without adding sand or aggregate; the water/cement (w/c) ratio was 0.45 and the concentration of MWCNTs was 0.1% weight of cement. In a second case, CNTs were wrapped

by surfactants, dispersed in an aqueous solution and mixed with cement. The w/c ratio and CNT concentration were the same as before. Compression tests have shown that covalent treatment leads to a stronger piezoresistive response and a higher signal-to-noise ratio than the non-covalent method. This can be addressed to the different nanotube to nanotube interfaces. In fact, the use of surfactants preserves the electrical and mechanical properties of CNTs, but tunneling and, therefore, the piezoresistive response of the composite are negatively affected. On the other hand, the acid treatment decreases the electrical conductivity of individual CNTs [9], but it does not prevent tunneling, thus resulting in a better piezoresistive response of the composite at the macro-scale [5]. Untreated CNTs or non-covalent treatments can be, instead, recommended when the objective of doping is a reduction of the electrical resistance of the cement paste or an improvement of its mechanical properties.

The above reported discussion points out that the adopted functionalization method obviously affects also the mechanical properties of the composite. In spite of their excellent mechanical properties, untreated CNTs show poor adhesion with the matrix and that causes sliding [12]. Moreover, since they are prone to agglomeration after sonication, the CNTs assembled in bundles show additional sliding inside the bundle that prevents a satisfactory load transfer [13]. Non-covalent treatment preserves the properties of CNTs but the amount of surfactant has a strong influence on the final mechanical properties of the cement composite [14]. In fact, a small amount of surfactant reduces the protection against agglomeration, while large amounts lead to a reduction of the repulsion forces [15]. In both cases, sliding inside the bundles occurs and affects the load transfer. In spite of the detriment of graphitization degree caused by acids, covalent treatment ensures also a chemical bond with the matrix, and the presence of carboxylic groups enhances the reinforcement efficiency [13].

The above discussion seems to suggest the adoption of covalent treatment for SHM applications of CNT/cement composites. In fact, it ensures an effective dispersion of CNTs in the matrix, a mechanical efficiency due to the chemical bond between carboxylic groups and cement matrix and, above all, an optimal piezoresistive response (even in the case of cyclic loads) with a high signal-to-noise ratio. Acid treatment has a large capacity to functionalize nanotubes in large amount. However, this approach involves also multiple steps such as filtering, sonication, mixing and drying processes, which generate a lot of defects in the nanotubes and the yield rate is pretty low [16,17].

In order to overcome the main drawback related to the detrimental effect of acid functionalization on the graphitization degree, innovative RF plasma technologies for the functionalization of CNTs in view of sensor development for SHM applications are under investigation at the University of Cincinnati. They are able to attach the functional groups

on the surface of CNTs while preserving their mechanical properties. This functionalization procedure also improves dispersion of nanotubes in the host matrix. The proposed approach is called "dry functionalization" using cold plasma state. Plasma functionalization is clean, efficient, low-temperature approach using a glow discharge. It is able to decrease substantially the damage on the CNT. In fact, the surface modification of CNTs is achieved in low temperature plasmas. By such a treatment, oxygen and nitrogen containing groups can be bonded to the surface of CNTs. [18,19,20,21]. A homogeneous treatment of CNTs requires the development of appropriate techniques for fluidizing the CNTs in the plasma zone. The available studies related to plasma treatment of CNT materials [18,19,21,22] show that these techniques are based on expensive, low pressure plasma facilities which require sophisticated vacuum pumps, and complicate the deposition system.

Thus, an innovative plasma treatment [23,24] for CNT functionalization at low and atmospheric pressure using different precursor gases is investigated. The effect of the process parameters such as gas composition, plasma power and the nature of the CNT has been studied. Ammonia, HCOOH, H₂, O₂, and CO₂ have been experimented as plasma gases. The plasma environment that they create contributes to the attachment of different functional groups to the CNT surface such as: C-N=O, C-NH₂, C-OH, C-H, C=O, and COOH. Various parameters may influence the density of spores in the water after exposure to the plasma. These parameters are the type of gas or gas mixture used to generate the plasma, distance of the suspension to the plasma source, gas flow rate, and forward power to the plasma. A number of parameters influencing the functionalization of the CNT material have been investigated; they are:

1. frequency of the plasma, which determines how energetic are the plasma species;
2. treatment time;
3. type of gas or gas mixture (Helium, Hydrogen, Argon, Oxygen and ambient air) used to generate the plasma;
4. plasma gas flow rate;
5. distance of the suspension to the plasma source;
6. forward power to the plasma.

A matrix of experiments has been designed to observe how variation of these parameters affects the CNT functionalization over time. An example of selected parameters is reported in Table 1. The targeted plasma treatment conditions included optimal combination of parameters resulting in the most efficient functionalization using the lowest amount of input energy, gas volume and time. The optimization of the innovative plasma functionalization process has taken advantage of both the results of the experiments and the feedback from the analytical work after plasma treatment of the CNTs.

Table 1. Influence of Selected Plasma Parameters on CNT Functionalization—Matrix of Experiments.

Parameter	Value				
	Microwave			RF	
Plasma Frequency					
Time of Treatment (minutes)	1	5	10	20	30
Nature of the Plasma Gas	He	H ₂	Ar	O ₂	Air
Plasma Gas Flow Rate (SCLM)	1	2	3	4	5
Distance of CNT surface from Plasma Nozzle (cm)	-0.5	0	0.5	1.0	2.0
Power of the Plasma (W)	100	200	300	400	500

The approach to plasma functionalization of CNTs is based on the Atmospheric Plasma Deposition System. This torch is capable of generating high-density plasma of reactive species at ambient pressure and temperatures below 250°C. It is a downstream source that eliminates ion bombardment of the sample. The base unit is supplied with an applicator with 25 mm in diameter active area, and an air-cooled 300 W RF generator performing at 27.12 MHz. The RF atmospheric pressure plasma source is shown in Figure 1. It will produce a plasma environment at very low temperature (below 75°C), which will preserve the CNT materials from damaging. The RF applicator can be scaled up to circular or rectangular plasma sources with greater dimensions for treating big area CNT structures. The torch can be mounted on an automated scanning stage

to uniformly treat large substrates, from a few inches to several feet across. The plasma operates with helium and any reagent gas, such as oxygen, hydrogen, nitrogen, or carbon tetrafluoride.

The functionalized CNTs and their surface composition are characterized by X-ray Photoelectron Spectroscopy (XPS), Time-of-Flight Secondary Ion Mass Spectrometry (TOF SIMS) and Fourier Transform Infrared Spectroscopy (IRFT). XPS provides data related to the elemental composition on the surface of the CNTs after functionalization. TOF SIMS and FTIR help identifying the functional groups covalently bonded to the CNT surface. These three analytical techniques are available at the University of Cincinnati and applied in the present research.

The validation and optimization of the innovative RF plasma functionalization method is still in progress, but the herein discussed aspects and preliminary results point out that it represents a very promising and effective alternative for functionalization of CNTs. The ability to preserve the structure and, therefore, the mechanical properties of CNTs makes this method ideal for applications aimed at both the development of self-sensing materials and the improvement of the mechanical performance materials of cement based materials. An experimental validation based on the comparative analysis of the piezoresistive response of acid functionalized and plasma functionalized CNT/cement composites will be the objective of future investigations.

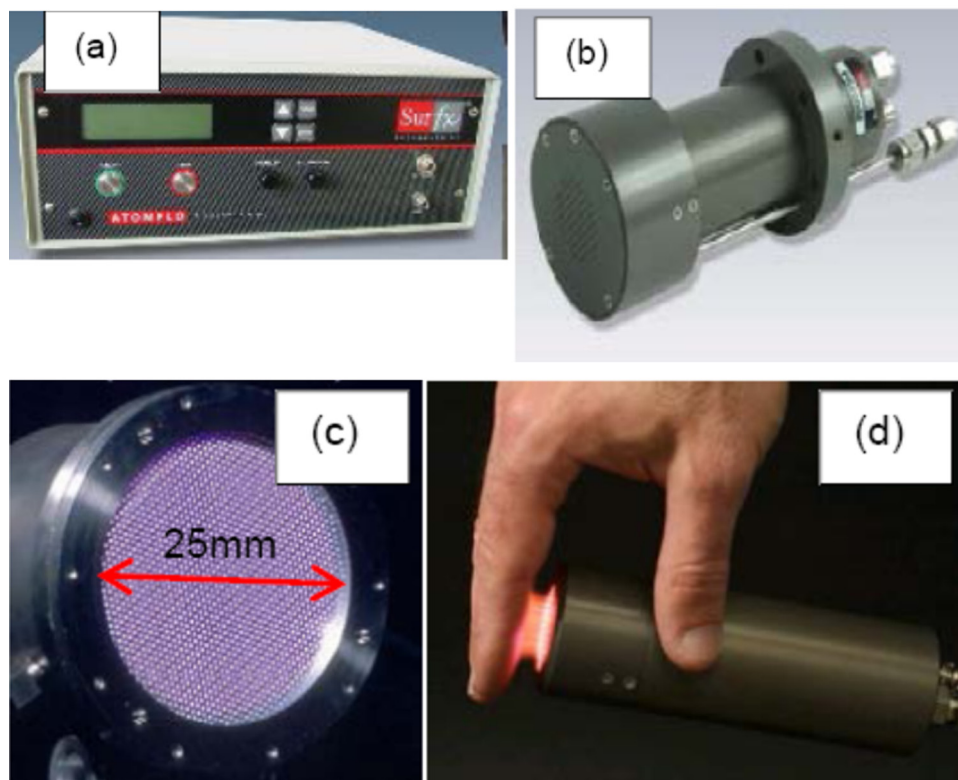


Figure 1. RF Atmospheric pressure plasma source: power supply (a); plasma torch (b); O₂ plasma source in action (c, d).

3. RECOMMENDED CNT CONCENTRATION AND DISPERSION IN CEMENT PASTE

The classical covalent and non-covalent treatments are not sufficient in themselves to obtain an effective dispersion of CNTs in the cement matrix. As mentioned in the previous section, the application of ultrasonic energy is absolutely required [14]. An extensive literature review reveals that, independently on the objective of the research (in the literature there are several studies focused on the analysis of the performance obtained from different functionalization treatments; some of them have been previously discussed, but there are also other interesting papers focused, for instance, on the analysis of the capability of different surfactants in dispersing MWCNTs and their compatibility with cement [25], or on the identification of the optimum weight ratio of surfactant to CNTs for complete dispersion [14], that are out of the scope of the present paper), functionalization is always applied in combination with mechanical agitation, usually ultrasonication. However, duration and power of sonication differ from one paper to another and they are sometimes not declared. Acid treatment is usually associated to sonication for 1–3 hours [5,7,26]. A summary of the adopted values of sonication power and time is reported in Table 2; in those case where the sonication power was not declared, it has been inferred from the model of the ultrasonic bath whenever possible.

A detailed description of the procedure for dispersion of CNTs by sonication and covalent treatment is reported in [26]. The information about sonication power is also critical, but it can be hardly recovered from a literature review. In principle, an excessive sonicating energy causes defects and serious damage to CNTs [2, 27]. In order to preserve the length and structure of CNTs, low power bath sonication is recommended [2]. The usually adopted sonicators are characterized by the following specifications: 80–130 W maximum input power and 20–40 kHz frequency. Moreover, the following value of the power per solution volume can be adopted as a reference to avoid breakdown of CNTs: 0.4626 W/ml [27].

Workability of the composite, percolation threshold and

cost mainly influence the choice of the type and quantity of CNTs to be dispersed in the cement matrix. MWCNTs are less expensive than SWCNTs [8] and represent a more profitable choice for extensive research purposes and practical applications. Higher workability problems are reported in the literature when SWCNTs are used to prepare the samples [28]. The fluidity of the mix, in particular, plays a primary role in molding. The drop of fluidity is due to the large surface area of CNTs that causes a significant amount of surface interactions within the mix. As a consequence, the use of MWCNTs, characterized by larger diameters and, therefore, a lower surface-area-to-volume (SA/V) ratio with respect to SWCNTs [27], can be recommended to ensure sufficient workability, in spite of the more effective mechanical reinforcement associated with the use of SWCNTs.

The fabrication of smart cement composites for SHM based on MWCNTs requires the choice of their aspect ratio (length-to-diameter ratio). In fact, it has a large influence on both dispersion and electro-mechanical behavior of the composite. Since sonication can damage long CNTs, the effective dispersion of long CNTs without breaking them is fairly difficult. Another drawback with the use of long CNTs is related to the percolation phenomenon. The inclusion of CNTs makes cement more conductive and this effect further advances with their addition until the volume fraction reaches the percolation threshold. Increasing the concentration of CNTs beyond this threshold only results in marginal increases in the electrical conductivity of the composite. Thus, the percolation theory [29] provides important guidelines for the manufacture of CNT/cement composites.

In [30] it is shown that the percolation concentration depends on conductive fibre geometry instead of system composition: the longer the conductive elements, the lower the threshold. Thus, long CNTs are more prone to create a continuous conductive path and this affects also the piezoresistive response of the composite. In fact, when a continuous network of CNTs is formed, the change in the resistance of the composite under the applied loads is mainly due to the change in geometry and, therefore, electrical resistance of the nanotube network. This resistance change is fairly low because of the very small elastic deformation of CNTs. On

Table 2. Sonication Power and Time in the Fabrication of Self-sensing CNT/Cement Composites.

Reference	Functionalization	Sonication Power [W]	Sonication Time [min]
Yu and Kwon (2009) [5]	Non-covalent	N.A.	60
Yu and Kwon (2009) [5]	Covalent	N.A.	60
Han <i>et al.</i> (2011) [35]	Non-covalent	130	120
Konsta-Gdoutos <i>et al.</i> (2010) [14]	Non-covalent	500	N.A.
Li <i>et al.</i> (2007) [9]	Covalent	100	N.A.
Li <i>et al.</i> (2005) [26]	Covalent	N.A.	180
Han <i>et al.</i> (2010) [7]	Non-covalent	130	120
Coppola <i>et al.</i> 2011 [31]	Non-covalent	N.A.	150

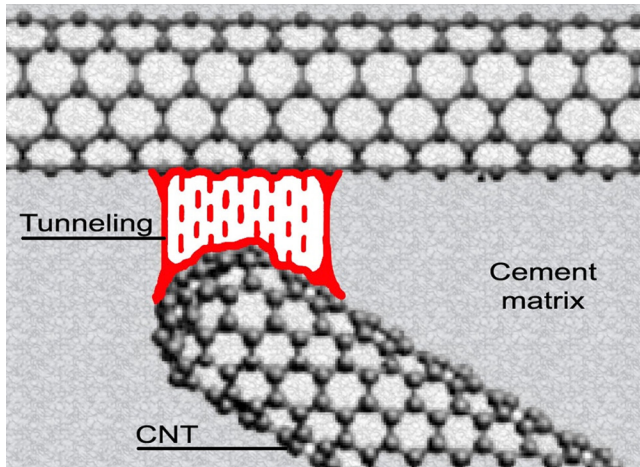


Figure 2. Illustration of electrical tunneling between adjacent carbon nanotubes in the cement matrix.

the contrary, the effective dispersion of CNTs in the matrix avoids the formation of a continuous conductive path, and the resistance change of the composite is mainly due to changes in the contact resistance. This is associated to thickness variations of the insulating matrix between adjacent nanotubes where tunneling (Figure 2) takes place. Thus, short MWCNTs are recommended over the long ones since they can be more effectively dispersed in the matrix. They lead to higher percolation threshold since the creation of a continuous conductive path is more difficult.

As reported in [31], the percolation threshold of CNT/cement composites is likely lower than 1% of cement content, when the matrix is made by cement paste and MWCNTs are adopted. This is in agreement with the typical concentration of CNTs (in the range 0.1–0.5% weight of cement) adopted in the fabrication of cement based sensors [5,7,9,31,32,33]. It is worth noting that the percolation threshold is higher when the matrix is made by mortar instead of cement paste [31]. This is a result of the double percolation, as discussed in [6].

4. ADDITIONAL REMARKS ON THE PREPARATION OF SAMPLES

Additional aspects about sensor fabrication concern the definition of an appropriate w/c ratio and the effect of water content on the piezoresistivity of MWCNT/cement composites. The variations of w/c ratio among a number of different studies are moderate. The w/c ratio is usually set in the range 0.4–0.6 for different types of functionalization, MWCNT characteristics and procedures of fabrication of the composite. It is worth pointing out here that the hydrophilic nature of acid treated CNTs can reduce the amount of available water for cement hydration [13]. Thus, a suitable hydration of the cement paste requires a w/c ratio in the range 0.5–0.6 when acid treated MWCNTs are used.

After preparation of the mix, it is usually poured into oiled molds, surface-smoothed and covered with plastic films. Specimens are demolded 24 h after casting and cured under the standard condition at a temperature of 20°C and a relative humidity of 100% for 28 days. Finally, they are dried, at room temperature or in oven. However, tests on these specimens are not fully representative of the actual conditions in the host structure. The real conditions of application in civil engineering require the consideration of the effect of water content on the piezoresistive response of the composite. In fact, even if the primary conduction path is represented by CNTs, the amount of un-hydrated water in the composite also influences the overall resistivity as an effect of the ion movement in the pore solution of hydrated cement. In [7] it is shown that water content plays an important role in determining the sensitivity of the sensors. In particular, this improves until a 6% water content, then it gets worse. Thus, excessive water content (over 7–8%) has to be avoided to obtain the best self-sensing performance.

A proper measurement scheme has to be set to measure the resistivity changes in the specimens. The main issues are related to the setting of the current frequency and the selection between the two-probe and the four-probe layout. In carboxyl MWCNT/cement composites the resistance shows a reversible pressure-sensitive response to compressive loading. However, these composites have both resistance and capacitance characteristics, and the capacitance is insensitive to compressive loading. The charging of the capacitor just causes a linear increase in the measured resistance during DC measurement [33]. This is an effect of electric polarization. The tendency to polarize decreases when the material is more conductive, so addition of CNTs to the cement paste reduces this effect. However, since CNT/cement composites are also capacitive, charge build-up is possible and appropriate countermeasures have to be taken to prevent polarization. Since capacitance is inversely proportional to current frequency, the effects of reactance can be reduced using high frequency AC, so that only the resistive component is used for sensing purposes. When the phase angle is zero, purely resistive impedance occurs.

Therefore, measurements of the phase angle at different current frequencies allow the identification of the best setting for the current frequency. Even if resistance is generally assumed constant and independent of frequency, the resistance of a circuit to AC is greater than its resistance to DC. This effect is small at low frequencies, but it has to be taken into account at high frequencies, where the difference becomes more pronounced [34]. The piezoresistive sensitivity of carboxyl MWCNT/cement composites also increases with the decrease of AC voltage amplitude [33]. In fact, high voltage amplitude at both ends of the composite can more easily induce capacitor charging and discharging during the test. Thus, a proper setting of the current frequency and adoption of low amplitude AC voltage give a contribution

in eliminating the effect of capacitance on the pressure-sensitive responses of carboxyl MWCNT/cement composites.

Clean and corrosion-free electrodes have to be used for resistance measurements. Both stainless steel and copper gauzes are usually adopted [31,35]. Additional recommendations about electrode design and measuring method can be found in [36], even if attention is there focused on carbon fiber cement paste piezoresistive sensors. The use of copper gauzes is recommended since copper shows high durability, low polarization and small contact resistance, and it can be more easily embedded into the composite. Moreover the area of voltage pole and the mesh size of gauze electrode do not influence the resistivity. Since the mesh size has negligible influence on the accuracy of measurements, fairly large values can be adopted to reduce the influence of the probes on the mechanical properties of the composite. The four-pole layout has to be adopted whenever possible, since it can eliminate the contact resistance whereas the direct-current two-pole method cannot.

The spacing between current and voltage poles does not influence the resistivity when larger than the critical value of 0.75 cm. Finally, since the specimen capacitance

becomes more influential at smaller inter-electrode spacing, the distance between the (inner) probes has to ensure that the resistivity values do not decrease but remain almost constant while increasing the spacing [37]. Previous studies have shown that this spacing can be set equal to 40 mm for carboxyl MWCNT/cement composites and four probe measurements [9,31].

In summary, as a result of the present research, a standardized fabrication procedure for CNT/cement sensors can be outlined as in Figure 3. The optimal concentration of MWCNTs can be found by changing the value of CNT concentration until the piezoresistive sensitivity of the composite is maximized.

5. CONCLUSIONS

The present study represents one of the outcomes of a joint US-Italy research program aiming at the development of a biomimetic SHM system for civil structures. The main components of such a system will be the embedded CNT/cement sensors. Thus, different aspects of fabrication of CNT/cement composites for SHM applications have been

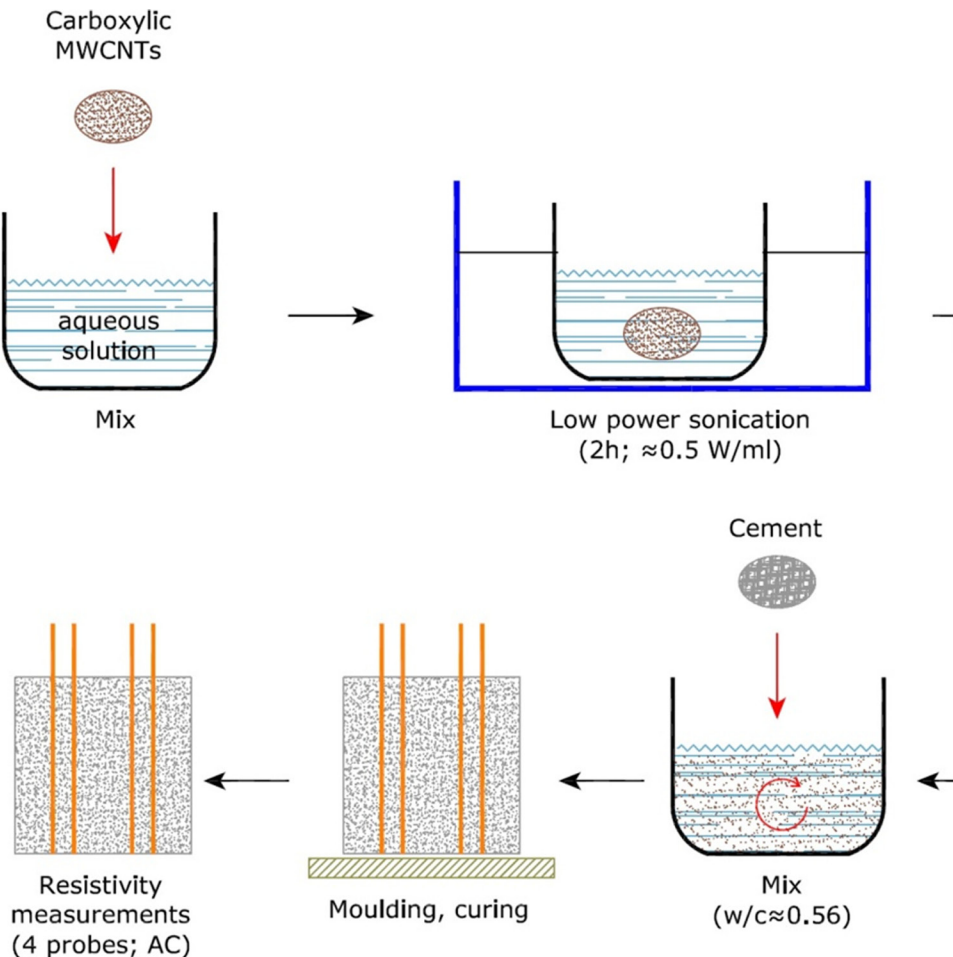


Figure 3. Illustration of the designed fabrication process of MWCNT/cement sensors.

discussed, focusing the attention in particular on an innovative RF plasma technology for CNT functionalization. This is able to attach different functional groups on the surface of CNTs without damaging them, thus preserving their excellent mechanical and electrical properties. The possibility to attach carboxyl groups makes the plasma functionalized CNTs appropriate for dispersion in cement matrices. The optimization of this innovative functionalization technology is still under development in view of the applications, but it can be already considered a promising alternative for CNT functionalization and fabrication of smart cement composites. As a result of the herein described research, guidelines for the standardized fabrication of effective CNT/cement sensors for SHM of civil structures have also been identified and reported.

In summary, carboxyl (both acid treated or plasma functionalized) MWCNTs have to be dispersed in aqueous solution. Low power sonication has to be also applied for 2 h when acid functionalization is adopted. CNTs can then be mixed with the cement paste (optimal w/c ratio ≈ 0.56). Copper gauzes characterized by a fairly coarse mesh can be used as electrodes and embedded in the paste at proper distance. A four probe layout is recommended. A spacing between current and voltage poles larger than 0.75 cm has to be adopted. After demolding and curing, the piezoresistive response can be measured through an impedance analyzer, by setting the AC current frequency in a way able to obtain purely resistive impedance. The definition of the most appropriate concentration of MWCNTs is still an open issue. However, a proper calibration of its value can be done by means of the maximization of the piezoresistive sensitivity of the composite. This specific aspect is out of the scope of the present paper. It is under development and represents the future step of the work.

6. ACKNOWLEDGMENTS

The present study has been carried out as a part of the “NANOSENSE” Research Project, funded in the framework of the Italy-USA Executive Programme (L. 401/90). Support by the Italian Ministry of Foreign Affairs is therefore gratefully acknowledged.

REFERENCES

- [1] Doebling, S.W., Farrar, C.R., Prime, M.B. and Shevitz, D.W., *Damage Identification and Health Monitoring of Structural and Mechanical Systems from Changes in their Vibration Characteristics: A Literature Review*, Technical Report LA-13070-MS, UC-900, Los Alamos National Laboratory, New Mexico 87545, USA (1996).
- [2] Kang, I., Schulz, M.J., Kim, J.H., Shanov, V. and Shi, D., “A carbon nanotube strain sensor for structural health monitoring”, *Smart Materials and Structures* 15, 737–748 (2006). <http://dx.doi.org/10.1088/0964-1726/15/3/009>
- [3] Minakuchi, S., Tsukamoto, H. and Takeda, N., “Hierarchical sensing system for detecting impact damage in composite structures combining a fiber optic spinal cord network and distributed sensor nerve cell devices”, *Proc. 7th International Workshop on Structural Health Monitoring, Stanford, CA, USA*, 878–885 (2009).
- [4] Iijima, S., “Helical microtubules of graphitic carbon”, *Nature* 354, 56–58 (1991). <http://dx.doi.org/10.1038/354056a0>
- [5] Yu, X. and Kwon, E., “A carbon nanotube/cement composite with piezoresistive properties”, *Smart Materials and Structures* 18 (2009).
- [6] Wen, S. and Chung, D.D.L., “Double percolation in the electrical conduction in carbon fiber reinforced cement-based materials”, *Carbon* 45, 263–267 (2007). <http://dx.doi.org/10.1016/j.carbon.2006.09.031>
- [7] Han, B., Yu, X. and Ou, J., “Effect of water content on the piezoresistivity of MWNT/cement composites”, *J. Mater. Sci.* 45, 3714–3719 (2010). <http://dx.doi.org/10.1007/s10853-010-4414-7>
- [8] Chen, S.J., Collins, F.G., Macleod, A.J.N., Pan, Z., Duan, W.H. and Wang, C.M., “Carbon nanotube–cement composites: A retrospect”, *The IES Journal Part A: Civil & Structural Engineering* 4, 254–265 (2011). <http://dx.doi.org/10.1080/19373260.2011.615474>
- [9] Li, G.Y., Wang, P.M. and Zhao, X., “Pressure-sensitive properties and microstructure of carbon nanotube reinforced cement composites”, *Cement & Concrete Composites* 29, 377–382 (2007). <http://dx.doi.org/10.1016/j.cemconcomp.2006.12.011>
- [10] Jia, Z., Wang, Z., Liang, J., Wei, B. and Wu, D., “Production of short multi-walled carbon nanotubes”, *Carbon* 37, 903–906 (1999). [http://dx.doi.org/10.1016/S0008-6223\(98\)00229-2](http://dx.doi.org/10.1016/S0008-6223(98)00229-2)
- [11] Duan, W.H., Wang, Q. and Collins, F., “Dispersion of carbon nanotubes with SDS surfactants: a study from a binding energy perspective”, *Chemical Science* 2, 1407–1413 (2011). <http://dx.doi.org/10.1039/c0sc00616e>
- [12] Ibarra, Y.S., Gaitero, J.J., Erkizia, E. and Campillo, I., “Atomic force microscopy and nanoindentation of cement pastes with nanotube dispersions”, *Physica Status Solidi(a)* 203, 1076–1081 (2006). <http://dx.doi.org/10.1002/pssa.200566166>
- [13] Musso, S., Tulliani, J.-M., Ferro, G. and Tagliaferro, A., “Influence of carbon nanotubes structure on the mechanical behavior of cement composites”, *Composites Science and Technology* 69, 1985–1990 (2009). <http://dx.doi.org/10.1016/j.compscitech.2009.05.002>
- [14] Konsta-Gdoutos, M.S., Metaxa, Z.S. and Shah, S.P., “Highly dispersed carbon nanotube reinforced cement based materials”, *Cement and Concrete Research* 40, 1052–1059 (2010). <http://dx.doi.org/10.1016/j.cemconres.2010.02.015>
- [15] Yu, J., Grossiord, N., Koning, C.E. and Loos, J., “Controlling the dispersion of multi-wall carbon nanotubes in aqueous surfactant solution”, *Carbon* 45, 618–623 (2007). <http://dx.doi.org/10.1016/j.carbon.2006.10.010>
- [16] Zhu, J., Kim, J., Peng, H., Margrave, J., Khabashesku, V. and Barrera, E., “Improving the Dispersion and Integration of Single-Walled Carbon Nanotubes in Epoxy Composites through Functionalization”, *Nano Letters* 3(8), 1107–1113 (2003). <http://dx.doi.org/10.1021/nl0342489>
- [17] Chen, R., Bangsaruntip, S., Drouvalakis, K., Kam, N., Shim, M., Li, Y., Utz, P. and Dai, H., “Noncovalent Functionalization of Carbon Nanotubes for Highly Specific Electronic Biosensors”, *PNAS* 100(9), 4984–4989 (2003).
- [18] Bruser, V., Heintze, M., Brandl, W., Marginean, G. and Bubert, H., “Surface Modification of Carbon Nanofibres in Low Temperature Plasmas”, *Diamond and Related Materials* 13, 1177–1181 (2004). <http://dx.doi.org/10.1016/j.diamond.2003.10.061>
- [19] Heintze, M., Bruser, V., Brandl, W., Marginean, G., Bubert, H. and Haiber, S., “Surface Modification of Carbon Nano-fibres in Fluidised Bed Plasma”, *Surface and Coating Technology* 174–175, 831–834 (2003). [http://dx.doi.org/10.1016/S0257-8972\(03\)00410-9](http://dx.doi.org/10.1016/S0257-8972(03)00410-9)
- [20] Parades, J., Martinez-Alonso, A. and Tascon, J., “Oxygen Plasma Modification of Submicron Vapor Grown Carbon Fibers as Studied by Scanning Tunneling Microscopy”, *Carbon* 40, 1101–1108 (2002). [http://dx.doi.org/10.1016/S0008-6223\(01\)00255-X](http://dx.doi.org/10.1016/S0008-6223(01)00255-X)
- [21] Shi, D., Lian, J., He, P., Wang, L., van Ooij, W., Schultz, M. and Mast, D., “Plasma Deposition of Ultrathin Polymer Films on Carbon Nanotubes”, *Applied Physics Letters* 81(27), 5216–5218 (2002). <http://dx.doi.org/10.1063/1.1527702>

- [22] Khare, B.N., Meyyappan, M., Kralj, J., Wilhite, P., Sisay, M., Imanaka, H., Koehne, J. and Baushchlicher, C.W. Jr., "A glow-discharge approach for functionalization of carbon nanotubes", *Applied Physics Letters* 81(27), 5237-5240 (2002). <http://dx.doi.org/10.1063/1.1533859>
- [23] Shanov, V., Datta, S., Miralai, F. and McDaniel, J., "Apparatus and Method for Treating a Workpiece Using Plasma Generated from Microwave Radiation", US Patent No 6,841,201(2005).
- [24] Datta, S., McDaniel, J., Miralai, F. and Shanov, V., "Portable Apparatus and Method for Treating a Workpiece", US Patent No 6,821,379 (2004).
- [25] Luo, J.L., Duan, Z. and Li, H., "The influence of surfactants on the processing of multi-walled carbon nanotubes in reinforced cement matrix composites", *Physica Status Solidi a-Applications and Materials Science* 206, 2783-2790 (2009).
- [26] Li, G.Y., Wang, P.M. and Zhao, X., "Mechanical behavior and microstructure of cement composites incorporating surface-treated multi-walled carbon nanotubes", *Carbon* 43, 1239-1245 (2005). <http://dx.doi.org/10.1016/j.carbon.2004.12.017>
- [27] Abu Al-Rub, R.K., Ashour, A.I. and Tyson, B.M., "On the aspect ratio effect of multi-walled carbon nanotube reinforcements on the mechanical properties of cementitious nanocomposites", *Construction and Building Materials* 35, 647-655 (2012). <http://dx.doi.org/10.1016/j.conbuildmat.2012.04.086>
- [28] Makar, J., "The effect of SWCNT and other nanomaterials on cement hydration and reinforcement", *Nanotechnology in civil infrastructure: a paradigm shift*, K. Gopalrishnan *et al.* eds., Heidelberg: Springer, Berlin, 103-130 (2011). http://dx.doi.org/10.1007/978-3-642-16657-0_4
- [29] Pike, G.E. and Seager, C.H., "Percolation and Conductivity: A Computer Study", *I. Physical Review B* 10, 1421-1434 (1973). <http://dx.doi.org/10.1103/PhysRevB.10.1421>
- [30] Xie, P., Gu, P. and Beaudoin, J.J., "Electrical percolation phenomena in cement composites containing conductive fibres", *Journal of Materials Science* 31, 4093-4097 (1996). <http://dx.doi.org/10.1007/BF00352673>
- [31] Coppola, L., Buoso, A. and Corazza, F., "Electrical Properties of Carbon Nanotubes Cement Composites for Monitoring Stress Conditions in Concrete Structures", *Applied Mechanics and Materials* 82, 118-123 (2011). <http://dx.doi.org/10.4028/www.scientific.net/AMM.82.118>
- [32] Han, B., Yu, X. and Kwon, E., "A self-sensing carbon nanotube/cement composite for traffic monitoring", *Nanotechnology* 20 (2009).
- [33] Han, B., Zhang, K., Yu, X., Kwon, E. and Ou, J., "Electrical characteristics and pressure-sensitive response measurements of carboxyl MWNT/cement composites", *Cement & Concrete Composites* (2012). <http://dx.doi.org/10.1016/j.cemconcomp.2012.02.012>
- [34] Robbins, A. and Miller, W.C., *Circuit analysis: theory and practice*, Thomson/Delmar Learning, New York (2003).
- [35] Han, B., Yu, X., Zhang, K., Kwon, E. and Ou, J., "Sensing properties of CNT-filled cement-based stress sensors", *Journal of Civil Structural Health Monitoring* 1, 17-24 (2011). <http://dx.doi.org/10.1007/s13349-010-0001-5>
- [36] Han, B., Guan, X. and Ou, J., "Electrode design, measuring method and data acquisition system of carbon fiber cement paste piezoresistive sensors", *Sensors and Actuators A* 135, 360-369 (2007). <http://dx.doi.org/10.1016/j.sna.2006.08.003>
- [37] Bantia, N., Djeridane, S. and Pigeon, M., "Electrical resistivity of carbon and steel micro-fiber reinforced cements", *Cement and Concrete Research* 22, 804-814 (1992). [http://dx.doi.org/10.1016/0008-8846\(92\)90104-4](http://dx.doi.org/10.1016/0008-8846(92)90104-4)



Theoretical Analysis of the Catalytic Chemical Vapor Deposition Synthesis of Carbon Nanotubes

K. RAJI* and C. B. SOBHAN

Nanotechnology Research Laboratory, School of Nano Science and Technology, National Institute of Technology, Calicut, India 673 601

KEYWORDS

Carbon Nanotubes
Chemical Vapor deposition
COMSOL Software
Deposition rate

ABSTRACT

A theoretical analysis of the Chemical Vapor Deposition (CVD) process for synthesis of carbon nanotubes, in order to predict the spatial distributions of the concentration, velocity and temperature inside the reactor has been presented in this paper. The analysis is performed by solving the governing differential equations pertaining to the process which involves catalytic chemical vapor deposition (CCVD) with acetylene as the carbon source and iron oxide as the catalyst. The system of equations, namely the momentum, energy and mass transport equations have been solved using the COMSOL software. The predicted values of the carbon nanotube yield from the chemical kinetics model have been verified using experimental results. The analysis presented offers an effective tool in designing the CVD furnace and deciding on the operational parameters to be used, in the synthesis of carbon nanotubes using the Chemical Vapor Deposition method.

© 2013 DEStech Publications, Inc. All rights reserved.

1. INTRODUCTION

Carbon nanotubes have attracted considerable attention from scientists due to the special properties of these nano-sized structures, which make them excellent candidates for various technological applications [1–3]. Of the various methods adopted to produce Carbon nanotubes [4–12], the Chemical Vapor Deposition (CVD) technique is a cheap and simple process, and hence has been investigated through experimental studies and theoretical modeling, with a view to optimize the technique [13–17]. The method involves a two-step procedure, consisting of a catalyst preparation step (coating of iron catalyst on an appropriate substrate) followed by deposition of the nanotubes on the catalyst-coated substrate placed inside a furnace, due to the chemical reactions, starting from a gaseous precursor such as acetylene. Carbon nanotubes will be formed if proper physical parameters are maintained in the process. The important influencing factors in the formation of carbon nanotubes are the synthesis temperature, pressure, the volumetric flow rate of

the precursor, the catalyst and the supporting material. These conditions can vary throughout the CVD reactor during the growth of carbon nanotubes. Since some previous publications [18–23] suggest that the geometry and yield of carbon nanotube are influenced by its growth temperature, it is required to find out the temperature distributions inside the furnace to develop a good theoretical model aimed at the design and optimization of the CVD reactor. A computational fluid dynamic model would provide a good description of the local temperature distribution and deposition of amorphous carbon inside the reactor.

Previous publications have explored the influence of various parameters of the CVD reactor during the carbon nanotube formation. Grujicic *et al.* [24] used a coupled boundary layer laminar flow hydrodynamic, heat transfer, gas-phase chemistry and surface chemistry model to examine CVD of carbon nanotubes consisting of methane and hydrogen in the presence of cobalt catalytic particle in a cylindrical reactor. The model determines the gas—phase fields for temperature, velocity, and species concentration as well as the surface coverages, the carbon nanotube growth rate and deposition rate of amorphous carbon. Kuwana *et al.* [25] applied a

*Corresponding author. Email: raji.kochandra@gmail.com

computational fluid dynamics model with multi step chemical reactions to calculate the yield of multi walled carbon nanotubes produced from a Xylene-based chemical vapor deposition reactor. A laboratory-scale two-step CVD reactor was developed, that can synthesize multiwalled carbon nanotubes and used to measure the total yield of nanotubes with a microbalance. They predicted the total yield and deposition rate of nanotubes over different time periods. In further work [26] a two-equation model was presented, which could predict the formation of iron nanoparticles from ferrocene fed in to a CVD reactor. The model, combined with an axisymmetric two-dimensional computational fluid dynamics (CFD) simulation, included the mechanism of nucleation and surface growth of an iron particle and bi-particle collision. The model predicted that the diameter of a particle will increase with an increase in the reaction temperature or the radial distance from the center of the reactor.

Kuwana *et al.* [27] applied a series of computational calculations to understand the gas-phase reactions of Xylene, a typical feedstock for carbon nanotubes. They combined a xylene reaction model and a soot formation model and calculated the isothermal pyrolysis of xylene to understand the gas-phase species during the CVD synthesis of carbon nanotubes. Their model showed that xylene and toluene were the major gas-phase species at temperatures lower than 973 K, implying that nanotubes were formed through the interaction between catalyst and xylene and/or toluene at these temperatures. At higher temperatures, however, a considerable amount of acetylene was found which possibly enhanced the growth of polycyclic aromatic hydrocarbons and soot as evidenced at 1373 K. Endo *et al.* [28] presented a computational fluid dynamics model to predict the production rate of nanotubes via catalytic decomposition of Xylene in a CVD reactor. In this model, two gas-phase reactions and four surface reactions were considered. This model predicted uniform velocity and temperature distributions in the furnace region and also the total production rates of CNTs.

A reaction scale simulation was performed on a tube flow CVD reactor by Lombardo *et al.* [29] using the software package COMSOL. The simulation was done to observe how different combinations of parameters affect the growth rate of CNTs, in order to understand how to optimize the reactor. The model revealed multiple limiting regimes of CNT growth at different reaction conditions. Mishra [30] carried out a CFD study to simulate velocity, temperature, and concentration profiles in a vertical chemical vapor deposition (CVD) reactor used for growing carbon nanofibers (CNFs). The numerical model was solved by taking conservation equations of momentum, energy, and species. Natural convection effects on the heat-transfer and the exothermic heat generation due to the decomposition of benzene were included. The simulation results revealed that approximately uniform temperature and concentration profiles existed in the reactor.

The present study investigates the processes in the CVD reactor using a computational model. The major objective of the investigation is obtaining the fluid dynamic behavior of the reacting flow, and to calculate concentration distribution of amorphous carbon (which will produce the CNTs) in the CVD reactor, for a given furnace wall temperature using the model.

Nomenclature

ρ	= density (Kg/m ³)
u	= Axial velocity (m/s)
T	= Temperature (K)
k	= Thermal conductivity (W/m K)
C_p	= Heat capacity at constant pressure (J/Kg K)
μ	= Viscosity (Pa s)
Q	= Heat due to chemical reaction (J/m ³ s)
Q_{ext}	= External heat added to the reactor (W/m ³)
R	= Rate expression (mol/m ³ s)
F	= Molar flow rate (mol/s)
V	= Reactor volume (m ³)

2. COMPUTATIONAL FLUID DYNAMICS MODEL

A computational Fluid Dynamics Model of the reacting flow in the CVD furnace can be helpful in determining the thermodynamic conditions in the reacting flow domain, nanotube growth rate, feed stock decomposition, byproduct compositions, transport rates and reaction mechanisms. Grujicic *et al.* [24] have reported investigations on determining the process parameters, growth conditions and fabricated material microstructure relationships during the growth of CNTs. In the present work, the CFD analysis of the reacting flow inside the CVD reactor during CNT synthesis is aimed at obtaining deposition of amorphous carbon, as will be explained here.

2.1. The Physical System

A schematic of the chemical vapor deposition apparatus for producing carbon nanotubes is shown in Figure 1. This method used acetylene as the precursor and grew carbon nanotubes on a ceramic substrate, vacuum-coated with the iron oxide catalyst, placed in a tubular quartz furnace. After the deposition, the product was scraped from the substrate, and purified with nitric acid and hydrogen peroxide to separate out the carbon nanotubes. The carbon nanotubes synthesized at 700°C were characterized using Scanning Electron Microscopy (SEM) and Transmission Electron Microscopy (TEM), the results of which are shown in Figures 2 and 3. The SEM images indicate that the product obtained is in the form of a bundle of carbon nanotubes.

In order to get a clearer understanding of the structure of the synthesized carbon nanotubes, TEM micrographs were

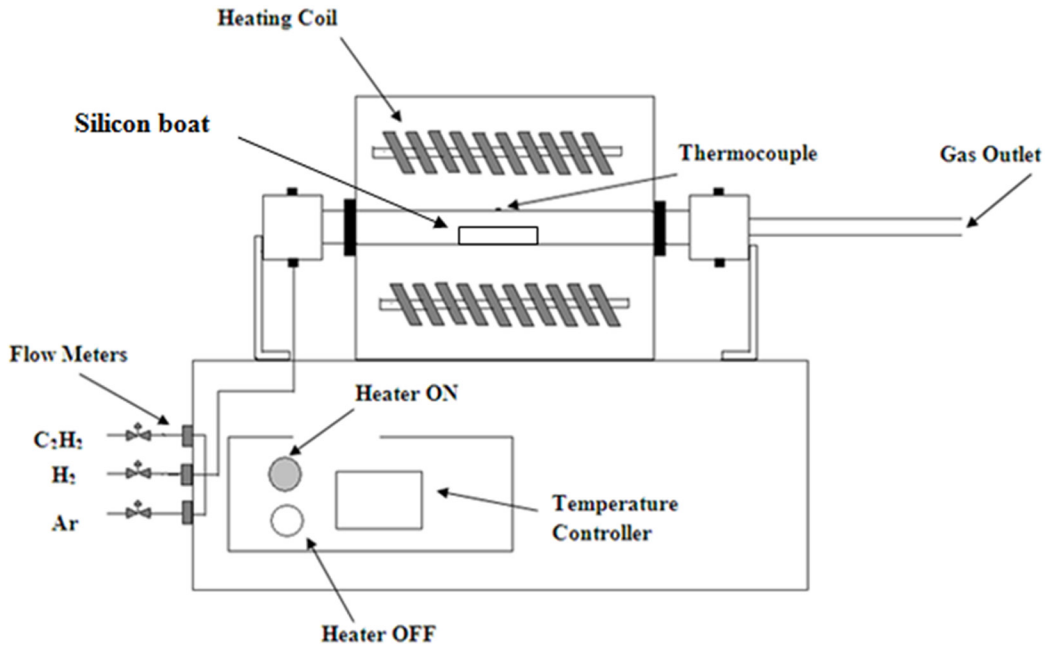


Figure 1. Schematic diagram of the CVD apparatus.

obtained. The diameter of the carbon nanotubes formed was found to lie in the range of 10–15 nm. The variation of the yield of carbon nanotubes as a function of the furnace temperature is shown in Figure 4 for the case of a volumetric flow rate of 0.07 lpm, at the end of 40 minutes of reaction. The predicted values of the carbon nanotubes yield [37] have been verified using experimental results. The results are found to match well. It is noted that there is a range of furnace temperatures where the yield steadily increases with respect to the furnace temperature, for a given flow rate. A detailed description of the experimental set up, the synthesis, the purification process [29–36] and microscopic analysis have been presented in an earlier publication [37].

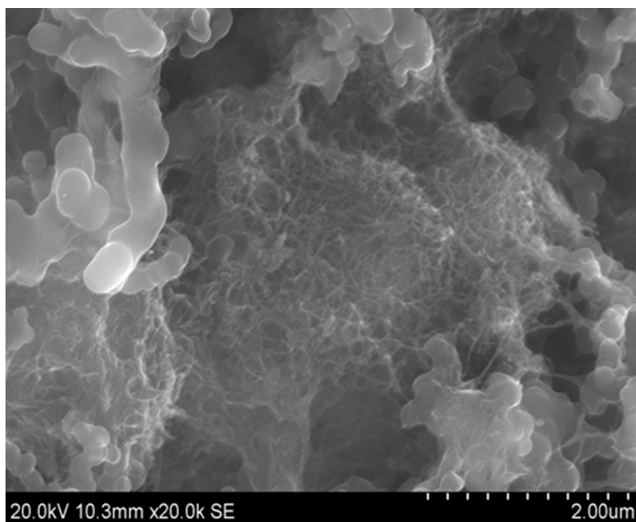


Figure 2. SEM image of CNTs at 700°C (2 μm resolution).

2.2. Computational Model for the Reaction

The elementary reactions of carbon nanotube formation have been described in a previous publication [37]. These reactions are the acetylene decomposition, iron carbide formation and iron carbide decomposition. The reactions were described based on the VLS growth process and modeled using chemical kinetics. The entire CVD process can be divided in

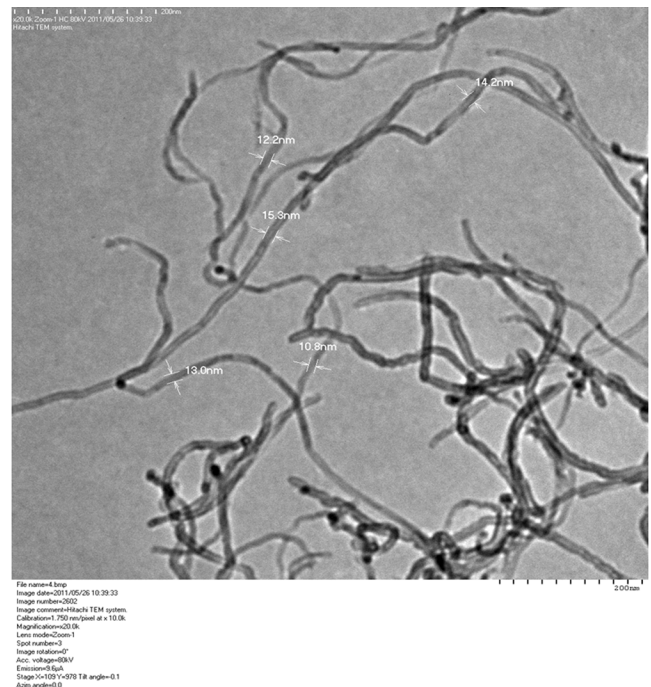


Figure 3. TEM image of CNTs at 700°C (200 nm).

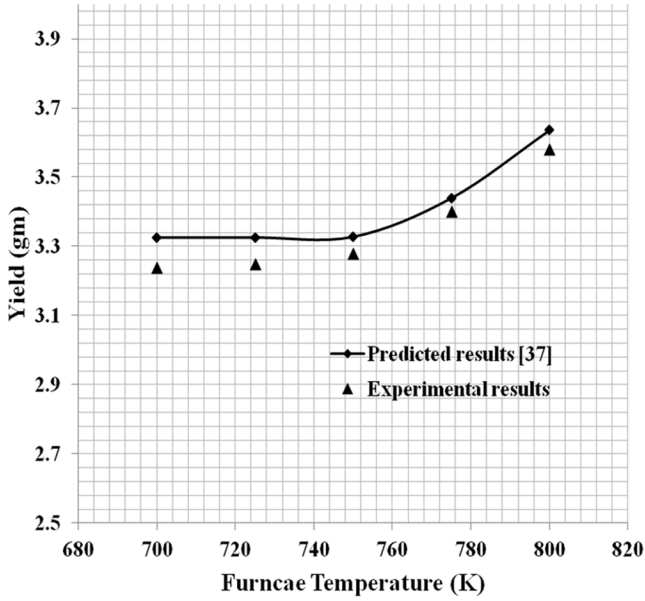


Figure 4. Yield of carbon nanotubes with furnace temperature (Predicted and Experimental).

to a reaction phase and a growth phase. The main reaction component in the process is the acetylene decomposition, and the growth components are iron carbide formation and iron carbide decomposition. As the latter two mainly happen through mass transfer (i.e. diffusion), it can be assumed that the acetylene decomposition is the main stream of the reaction, to be considered in the computational model. The reactor is assumed as a plug flow reactor. The design equation [Equation (1)] and energy balance equations [Equation (2)] are solved to get the conversion throughout the reactor, as given by,

$$\frac{dF_i}{dV} = R_i \quad (1)$$

$$\sum_i F_i C_{p,i} \frac{dT}{dV} = Q + Q_{ext} \quad (2)$$

2.3. Fluid Dynamics Model

The computational model adopted in the investigation is based on three dimensional, laminar and steady state flow, along with gas phase reactions. Figure 5 shows the geometrical configuration of the CVD reactor used in the numerical simulation. The equations of mass, momentum, energy, and mass transport [Equations (3), (4), (5), (6) and (7)] are solved to obtain the spatial distributions of temperature, velocity and concentration in the tubular reactor. The local variation of the fluid density is shown in Figure 6. This variation is a result of the mass depletion from the gas phase due to decomposition, and is incorporated in the energy equa-

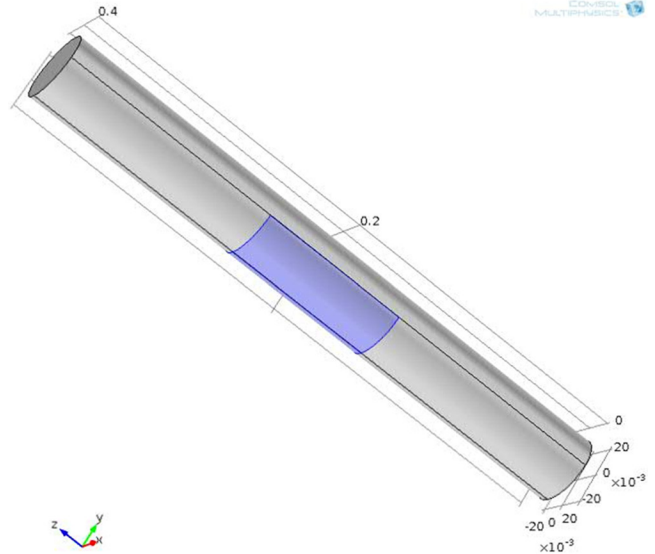


Figure 5. Geometrical configuration of the CVD reactor for simulation. The shaded region represents the catalyst container (silicon boat).

tion, as estimated through the mass conversion obtained by solving the chemical kinetic equations [Equations (1) and (2)]. Source terms which appropriately describe the reaction heat fluxes along the flow domain are also incorporated in the energy equation.

$$\nabla \cdot (\rho \vec{u}) = 0 \quad (3)$$

$$\rho \vec{u} \cdot \nabla \vec{u} = \nabla \cdot [-pI + \eta(\nabla \vec{u} + (\nabla \vec{u})^T) - \left(\frac{2\eta}{3}\right)(\nabla \cdot \vec{u})I] \quad (4)$$

$$\rho C_p u \cdot \nabla T = \nabla \cdot (k \nabla T) + Q \quad (5)$$

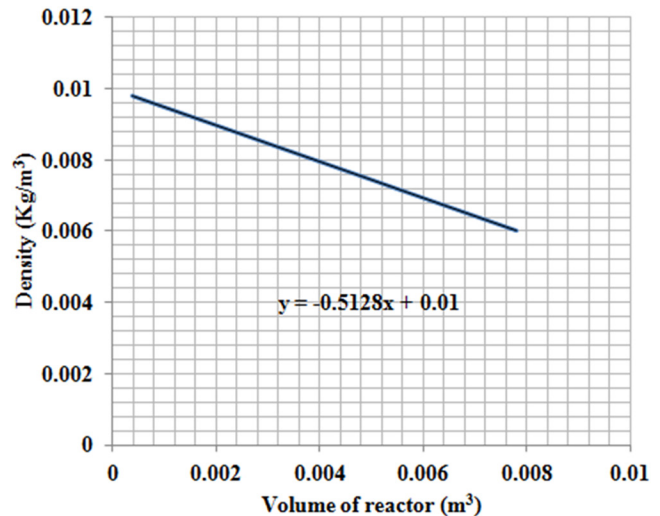


Figure 6. Density variation in the fluid inside the CVD reactor.

$$\nabla \cdot (-D_i \nabla c_i) + u \cdot \nabla c_i = R_i \quad (6)$$

$$N_i = -D_i \nabla c_i + u c_i \quad (7)$$

Where Q is appropriately chosen at the spatial location depending on whether the chemical change is locally exothermic or endothermic in nature.

The boundary conditions at the inlet of the reactor are a constant acetylene flow rate (4.2 lph) and a constant temperature (300 K). On the walls, a uniform temperature of 1000 K is imposed as the boundary condition, corresponding to a practical physical system. The no slip boundary condition was employed at the surfaces of the wall.

3. RESULTS AND DISCUSSIONS

The computational fluid dynamics calculations performed using the COMSOL software package yielded the temperature distribution inside the CVD furnace during the formation of carbon nanotubes, through the solution of the governing equations. The temperature at which the growth process takes place is one of major parameters which decide the size and yield of the carbon nanotubes. The local temperature in the furnace has been obtained by solving momentum and energy equation simultaneously with the results (density

change) obtained from the chemical model. The major results obtained are discussed below.

Figure 7 shows the spatial velocity distribution inside the reactor. It can be seen that the magnitude of velocity is maximum at the centerline of the reactor duct. It is also understood that at the region of the reactor where the catalyst container (boat) is placed, the magnitude of the velocity is higher compared to other regions, as expected due to the constriction in the cross sectional area available for the flow.

Figure 8 shows the temperature distribution inside the CVD reactor. At the entry region, a significant temperature drop is observed in radial direction. After this, until the deposition region, the temperature variation is found to be negligible, and the fluid temperature is found to be close to the surface temperature. Beyond the deposition region also, temperatures are found to be close to the wall temperature. A considerable change in temperature can be seen inside and near the catalyst container (boat) region of the reactor, where the nanotube deposition process takes place.

The decrease observed in temperatures at the boat region is the cumulative effect of the endothermic and exothermic reactions taking place in the reactor, which results in a reduced equilibrium temperature in this region. This means that that the growth temperature for the carbon nanotube formation is different from the furnace temperature, which is normally controlled. Hence, it would be more effective to use this ac-

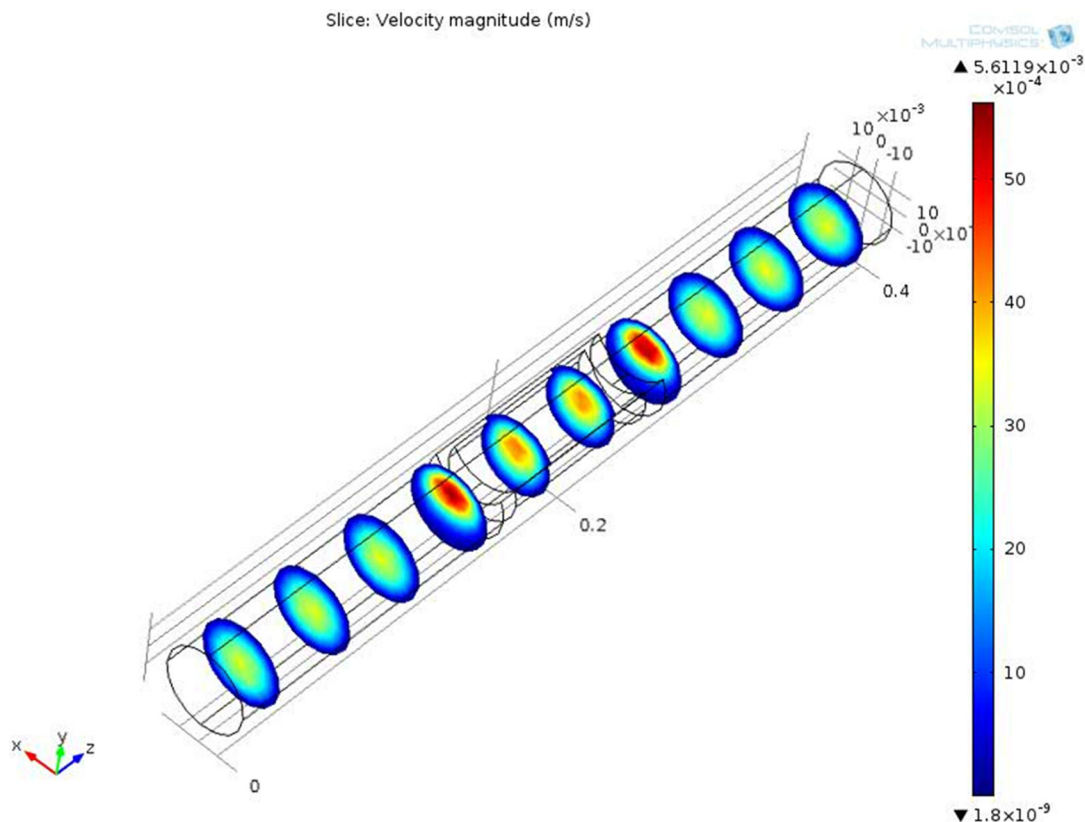


Figure 7. Velocity distribution inside CVD reactor.

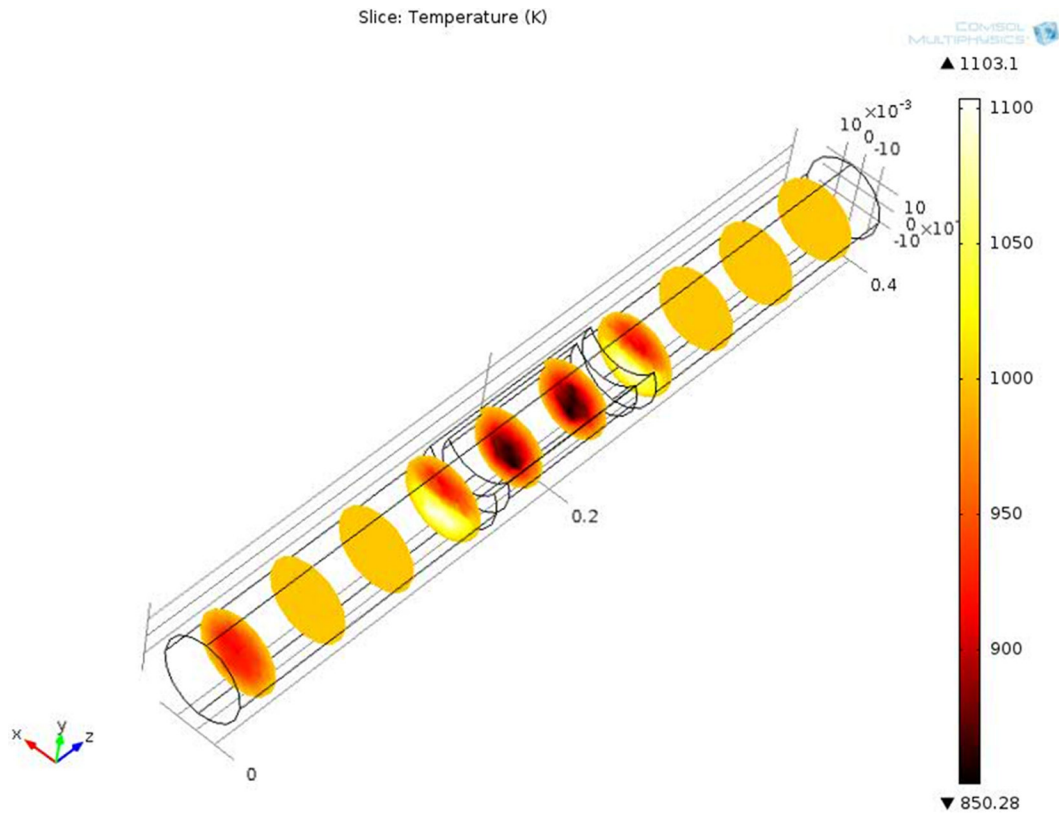


Figure 8. Temperature distribution inside CVD reactor.

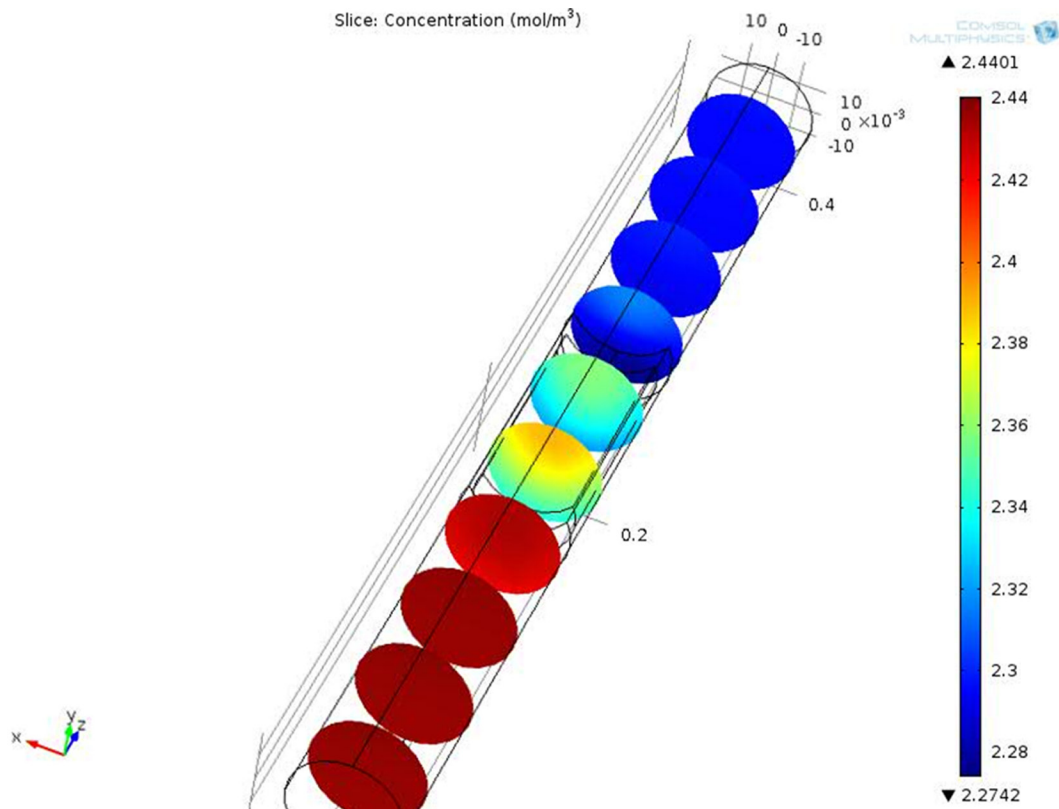


Figure 9. Concentration distribution of amorphous carbon inside CVD reactor.

tual growth temperature to set the operating temperature of the furnace accordingly. Figure 9 shows the spatial concentration distribution of amorphous carbon inside the reactor. At the entry region the quantity of amorphous carbon is more when compared to the deposition region of CNTs. It can be shown that the deposition of amorphous carbon is decreased with the length of the reactor. The carbon nanotubes will be produced from the amorphous carbon in the catalyst region of CVD reactor (deposition region of CNTs).

4. CONCLUSIONS

A computational fluid dynamic simulation has been performed to determine the temperature and concentration distribution inside a CVD reactor during carbon nanotube formation. A CVD reactor which involves acetylene as precursor and iron oxide as catalyst has been analyzed. The reactor is considered as a plug flow reactor. The density change due to the depletion of mass in the decomposition reaction has been calculated by solving mass balance equation (design equation of the reactor) with the energy balance equation in the CVD reactor. The velocity and temperature fields inside the reactor have been obtained by solving the governing differential equations of energy and momentum conservation. The distribution of concentration of amorphous carbon is obtained by solving the mass transport equations. It is concluded from the investigation that a considerable variation exists in the local temperature inside the reactor, at regions near the catalyst container, where the actual deposition process takes place, which makes the deposition temperature different from the furnace wall temperature, which is practically taken as the furnace temperature. This information can be used in developing precise theoretical models, and optimizing the CVD reactor for CNT synthesis.

REFERENCES

- [1] Charles P. Poole, Jr. and Frank J. Owen, *Introduction to Nanotechnology*, John Wiley Inter science publication, Canada (2003).
- [2] Endo, M., Strano, M. S., and Ajayan, P. M., "Potential Applications of Carbon nanotubes" A. Jorio, G. Dresselhaus, M. S. Dresselhaus (Eds.), *Carbon Nanotubes, Topics Appl. Physics 111*, 13–62 (2008).
- [3] Baughman, R. H., Zakhidov, A. A., Heer, W. A., "Carbon Nanotubes-The Root towards Applications," *Science* 297 (2002).
- [4] Yu, Z., Chen, D., Totdal, B., Zhao, T., Dai, Y., Yuan, W., Holmen, A., "Catalytic engineering of Carbon Nanotube Production," *Applied Catalysis* 279, 223–233 (2005). <http://dx.doi.org/10.1016/j.apcata.2004.10.032>
- [5] Gavrilov, Y. V., "The Synthesis of Few Walled Carbon Nanotubes by the Catalytic Pyrolysis of Methane and the Kinetics of their Accumulation," *Russian journal of Physical Chemistry* 81, 1502–1506 (2006).
- [6] Meyappan, M., *Carbon Nanotubes, Science and Applications*, CRC press (2004). <http://dx.doi.org/10.1201/9780203494936>
- [7] Choi, G. S., Cho, Y. S., Son, K. H., Kim, D. J., "Mass production of Carbon nanotubes using Spin-coating of Nanoparticles," *Micro-electronic Engineering*, pp. 77–82 (2003). [http://dx.doi.org/10.1016/S0167-9317\(03\)00028-5](http://dx.doi.org/10.1016/S0167-9317(03)00028-5)
- [8] Terrado, E., Redrado, M., Munoz, E., Maser, W. E., Benito, A. M., Martinez, M. T., "Carbon nanotube Growth on Cobalt-sprayed substrates by Thermal CVD," *Science and Engineering* 26, 1185–1188 (2006). <http://dx.doi.org/10.1016/j.msec.2005.09.054>
- [9] Terrado, E., Redrado, M., Munoz, E., Maser, W. K., A. M. Benito, M. T. Martinez, M. T., "Aligned Carbon Nanotubes Grown on Alumina and Quartz Substrates by a Simple Thermal CVD Processes," *Diamond and Related Materials* 15, 1059–1063 (2006). <http://dx.doi.org/10.1016/j.diamond.2005.10.071>
- [10] Rizzo, A., Rossi, R., Signore, M. A., Piscopiello, E., Capodieci, L., Pentassuglia, R., Dikonimos, T., Giorgi, R., "Effect of Fe Catalyst Thickness and C₂H₂/H₂ flow rate ratio on the Vertical Alignment of Carbon Nanotubes Grown by Chemical Vapor Deposition," *Diamond and Related Materials* 17, 1502–1505 (2008). <http://dx.doi.org/10.1016/j.diamond.2008.01.026>
- [11] Lee, C. J., Park, J., "Growth and Structure of Carbon Nanotubes Produced by Thermal Chemical Vapour deposition," *Carbon* 39, 1891–1896 (2001). [http://dx.doi.org/10.1016/S0008-6223\(00\)00311-0](http://dx.doi.org/10.1016/S0008-6223(00)00311-0)
- [12] Wang, X., Volodin, A., Haesendonck, C. V., Moreau, N., Fonseca, A., Janos, B., Nagy, J. B., "Controllable Growth of Individual, Uniform Carbon nanotubes by Thermal Chemical Vapour Deposition," *Physica E* 25, 597–604 (2004). <http://dx.doi.org/10.1016/j.physe.2004.09.001>
- [13] Oncel, C., Yurum, Y., "Carbon Nanotube Synthesis via through the Catalytic CVD Method: A Review on the Effect of Reaction Parameters," Taylor & Francis, 17–37 (2006).
- [14] Okamoto, A., Shinohara, H., "Control of Diameter Distribution of Single Walled Carbon Nanotubes Using the Zeolite-CCVD Method at atmospheric Pressure," *Carbon* 43, 431–436 (2004). <http://dx.doi.org/10.1016/j.carbon.2004.10.006>
- [15] Nasibulin, A. G., Pikhitsa, P. V., Jiang, H., Kauppinen, E. I., "Correlation between catalyst particle and Single walled carbon nanotube diameters," *Carbon* 43, 2251–2257 (2005). <http://dx.doi.org/10.1016/j.carbon.2005.03.048> Kato, T., Jeong, G. H., Hirata, T., Hatakeyama, R., "Structure Control of Carbon Nanotubes Using Radio-Frequency Plasma Enhanced Chemical Vapour Deposition," *Thin Solid Films* 457, 2–6 (2004).
- [16] Kato, T., Jeong, G.H., Hirata, T., Hatakeyama, R., "Structure Control of Carbon Nanotubes Using Radio-Frequency Plasma Enhanced Chemical Vapour Deposition," *Thin Solid Films* 457, 2-6(2004). <http://dx.doi.org/10.1016/j.tsf.2003.12.002>
- [17] Gopinath, P., Jay Gore, J., "Chemical kinetic considerations for post flame synthesis of carbon nanotubes in premixed flames using a support catalyst," *Combustion and Flame* 151, 542–550 (2007). <http://dx.doi.org/10.1016/j.combustflame.2006.05.004>
- [18] Kwok, C. T. M., Reizman, B. J., Daniel, E., Agnew, D. E., Weistrofer, G. S. S., Strano, M. S., Seebauer, E. G., "Temperature and Time Dependence study of Single-walled Carbon nanotube Growth by Catalytic Chemical Vapor Deposition," *Carbon* 48, 1279–1288 (2010). <http://dx.doi.org/10.1016/j.carbon.2009.11.053>
- [19] Iyuke, S. E., Abdulkareem, S. A., Afolabi, S. A., Piennar, C. H. Z., "Catalytic Production of Carbon Nanotubes in a Swirled Fluid Chemical Vapor Deposition Reactor" *International Journal of Chemical Engineering* 5 (2007).
- [20] Pirard, S. L., Douven, S., Bossuot, C., Heyen, G., Pirard, J. P., "A kinetic study of multi-walled carbon nanotube synthesis by catalytic chemical vapor deposition using a Fe-Co/Al₂O₃ catalyst," *Carbon* 45, 1167–1175 (2007). <http://dx.doi.org/10.1016/j.carbon.2007.02.021>
- [21] Khedr, M. H., Halim, K. S. A., Soliman, N. K., 2008 "Effect of Temperature on the Kinetics of Acetylene Decomposition over Reduced Iron Oxide Catalyst for the Production of Carbon nanotubes" *Applied Surface Science*, 255, 2375–2381 (2008). <http://dx.doi.org/10.1016/j.apsusc.2008.07.096>
- [22] Wirth, C. T., Zhang, C., Zhong, G., Hofmann, S., Robertson, J., "Diffusion and Reaction Limited Growth of Carbon Nanotube Forests." *ACS NANO*, 3, 3562–3566 (2009). <http://dx.doi.org/10.1021/nn900613e> PMID:19877596
- [23] Samandari-Masouleh, L., Mostoufi, N., Khodadi, A., Mortazavi, Y.,

- Maghrebi, M., 2012, "Modeling the Growth of Carbon Nanotubes in a Floating Catalyst Reactor." *Ind.Eng.Chem.Res.* 51, 1143–1149 (2012). <http://dx.doi.org/10.1021/ie201137j>
- [24] Grujicic, M., Cao, G., Gersten, B., "Optimization of Chemical Vapor Deposition Process for Carbon Nanotubes Fabrication." *Appl. Surf.Science* 191, 223–239 (2002). [http://dx.doi.org/10.1016/S0169-4332\(02\)00210-6](http://dx.doi.org/10.1016/S0169-4332(02)00210-6)
- [25] Kuwana, K., Endo, H., Saito, K., Qian, D., Grulke, R. A, E. A., "Catalyst deactivation in CVD synthesis of carbon nanotubes." *Carbon* 43, 253–260 (2005). <http://dx.doi.org/10.1016/j.carbon.2004.09.008>
- [26] Kuwana, K., Saito, K., "Modeling CVD synthesis of carbon nanotubes: Nanoparticle formation from ferrocene." *Carbon*, 43, 2088–2095 (2005). <http://dx.doi.org/10.1016/j.carbon.2005.03.016>
- [27] Kuwana, K., Li, T., Saito, K., "Gas-phase reactions during CVD synthesis of carbon nanotubes: Insights via numerical experiments." *Chemical Engineering Science* 61, 6718–6726(2006). <http://dx.doi.org/10.1016/j.ces.2006.07.006>
- [28] Endo, H., Kuwana, K., Saito, K., Qian, D., Andrews, R., Grulke, E., A., "CFD prediction of carbon nanotube production rate in a CVD reactor." *Chemical Physics Letters*, 387, 307–311 (2004). <http://dx.doi.org/10.1016/j.cplett.2004.01.124>
- [29] Djordjevic, V., Djustebek, J., Cveticanin, J., Velickovic, S., Veljkovic, M., M. Bokorov, Babicstojic, B., Neskovic, O., "Methods of Purification and Characterization of Carbon Nanotubes," *Journal of Optoelectronics and Advanced Materials* 8, 1631–1634 (2006).
- [30] Yu, H., Li, W. N., Qu, Y., Tian, X., Dong, Z. Wang, Y., Qin, K., Ren, W., 2008, "Purification of SWNTs Using High-Speed Centrifugation," Proceedings of the 3rd IEEE Int.Conf.on Nano/Micro Engineered and Molecular Systems.
- [31] Chiang, I. W., Brinson, B. E., Smalley, R. E., Margrave, J. L., Hauge, R. H., 2001, "Purification and Characterization of Single-wall Carbon nanotubes," *J.Phys.Chem* 105, pp. 1157–1161. <http://dx.doi.org/10.1021/jp003453z>
- [32] Colomer, J. F., Piedigrosso, P., Fonseca, A., Nagy, B., "Different Purification Methods of Carbon Nanotubes Produced by Catalytic Synthesis," *Synthetic Materials* 103, 2482–2483 (1999). [http://dx.doi.org/10.1016/S0379-6779\(98\)01066-2](http://dx.doi.org/10.1016/S0379-6779(98)01066-2)
- [33] Rosolen, J. M., Montoro, L. A., Matsubara, E. Y., Marchesin, M. S., Nascimento, L.F., Simone Tronto, "Step-by-Step Chemical Purification of Carbon Nanotubes Analyzed by High Resolution Electron Microscopy," *Carbon* 44, 3239–3301 (2006).
- [34] Moon, J. M., An, K. H., Lee, Y. H., Park, Y. S., Bae, D. J., Park, G. S., "High-Yield Purification of Single walled Carbon Nanotubes," *J.Phys.Chem* 105, 5567–5681 (2001). <http://dx.doi.org/10.1021/jp0102365>
- [35] Bougrine, A., Nagi, B., Ghanbaja, J., Billaud, D., "Purification and Structural Characterization of Single walled Carbon Nanotubes," *Synthetic Materials* 103, 2480–2481 (1999). [http://dx.doi.org/10.1016/S0379-6779\(98\)01064-9](http://dx.doi.org/10.1016/S0379-6779(98)01064-9)
- [36] Hou, P. X., 2002, "Multi-Step Purification of Carbon Nanotubes," *Carbon* 40, pp.81–85. [http://dx.doi.org/10.1016/S0008-6223\(01\)00075-6](http://dx.doi.org/10.1016/S0008-6223(01)00075-6)
- [37] Raji, K., Thomas, S., Sobhan, C. B., 2011, "A Chemical Kinetic Model for Chemical Vapor Deposition of Carbon Nanotubes," *Applied Surface Science* 257, 10562–10570. <http://dx.doi.org/10.1016/j.apsusc.2011.07.051>



Letter from the Editor

The 21st century has ushered in a tremendous level of interest in multifunctional composites. Composites that were once used only as structural reinforcements now have the added dimension of multi functionality, and are being used in novel applications such as structural composite batteries for the next generation of electric vehicles and soldier combat gear; structural embedded communication systems in helmets and vehicles; structural thermal management systems; and even in outer space exploration vehicles for radiation and debris shielding. Other novel features of these multifunctional composites include self-cooling, self-healing, adaptive and active morphing, and smart composites, all of which are topics of interest for this journal. As the world looks towards new ways to conserve energy and material and minimize cost, another important area of interest for this journal is in bio and green composites and renewable, sustainable composite manufacturing technologies.

We felt it was necessary to create a new platform primarily focused on reporting on the latest advances in this field, in addition to the more traditional areas of composites technologies. Amidst great anticipation, the Journal of Multifunctional Composites was launched in April 2013. I am pleased to report that in a short period of time, the journal has already generated a lot of interest from the scientific community. A lot of hard work has gone into launching this new journal and I am personally grateful to all the members of the editorial advisory board and the publishers for their continued efforts in making this journal a success. The second volume of this journal, in 2014, will contain four issues: January, April, July, and October.

With the exception of the first article, this October 2013 issue features a compilation of select papers from the 4th International Conference on Smart Materials and Nanotechnology in Engineering (SMN2013). I am grateful to Dr. Jayantha A Epaarachchi, Dr. Gayan C Kahandawa, and Dr. Mainul Islam from the University of Southern Queensland in Australia for serving as the guest editors for this issue. The January 2014 issue will contain more these papers.



Synthesis and Characterization of Ultralong Single-Walled Carbon Nanotubes

JIANING AN¹ and LIANXI ZHENG^{1,*}

¹*School of Mechanical and Aerospace Engineering, Nanyang Technological University, Nanyang Avenue 50, Singapore 639798*

KEYWORDS

Single-walled carbon nanotubes
Synthesis
Raman spectroscopy
Electrical measurements

ABSTRACT

Ultralong aligned single-walled carbon nanotubes (SWNTs) are very useful for high performance nanoelectronics because they have uniform properties along tube axis. In this study, ultralong and well-aligned SWNT arrays were synthesized via an ultralow gas flow chemical vapor deposition (CVD) system using ethanol as the carbon source. Raman spectroscopy was employed to comprehensively characterize the as-grown SWNTs. The intensity ratio of D band and G band (I_D/I_G) of the SWNTs was extremely low, indicating the nanotubes are of high quality. The frequencies of RBM and G band acquired along one isolated tube axis maintained constant over a large length scale, which reveals that the SWNT is structural and chiral uniform. Field-effect transistors (FETs) were fabricated with such ultralong single nanotube as conduction channel, exhibiting excellent performances. Our results show possibility of large scale fabricating SWNT-based electronic devices and perspective of creating integrated circuits on individual SWNTs.

© 2013 DEStech Publications, Inc. All rights reserved.

1. INTRODUCTION

As promising building blocks for the next generation electronics, single-walled carbon nanotubes (SWNTs) possesses unique characteristics and remarkable structural, physical, and electrical properties. Accordingly, intense researches have been dedicated to fabricating SWNT-based nanodevices and improving their performance [1–3]. One way to achieve high-performance nanodevices is to utilize ultralong and aligned SWNTs as the basic architectures, because these ultralong SWNTs with low density of defects could exhibit extraordinary electrical behaviors, which are comparable to the best short SWNTs [4], and at the same time the superior length together with the uniform structures along the tube axis enables large-scale fabrication of nanodevices on one SWNT, which facilitates the scaling in integrated circuits [5].

Raman spectroscopy has been widely used for characterizing SWNTs, because it is a noncontact and nondestructive measurement, operated at room temperature and in air. For

the ultralong SWNTs, the radial breathing mode (RBM) is useful to obtain the diameter of the examined nanotube, through the relations between the RBM frequency and the diameter of the SWNT [6]. The G band of the SWNT is used to identify its conducting type, based on the line shape of the G feature [7]. The intensity ratio of D band and G band (I_D/I_G) can be used as an evaluation of the quality of the SWNTs. Furthermore, the consistence of the RBM and G band frequencies along the tube length provide the direct evidence of the structural and chiral uniform of the specific nanotube.

In this study, we controllably synthesized ultralong SWNTs on Si/SiO₂ substrates, using chemical vapor deposition (CVD) method. The as-grown SWNT arrays were observed to be centimeter-long, well separated on the substrates. Raman spectra acquired on isolated nanotubes reveal that the nanotubes are of high quality. For each individual SWNT, the consistence of the frequencies of the Raman features suggests that the nanotube is structural and chiral uniform along its length. The field-effect transistors (FETs) made from the as-grown SWNTs exhibit excellent performances. The performance parameters of the SWNT-based FETs were also analyzed. Our results show a promising fu-

*Corresponding author. Tel: 65 67904163; Email: lxzheng@ntu.edu.sg

ture of employing SWNTs as the building blocks of nano-electronics.

2. EXPERIMENTAL DETAILS

2.1. Synthesis of Single-walled Carbon Nanotubes

Compared with other growth method, gas-flow-guided CVD is an appealing approach to obtain horizontally-aligned ultralong SWNTs on surfaces, which almost invariably requires the presence of transition metal nanoparticles as the catalysts [8]. In our experiments, the FeCl_3 ethanol solution, with a concentration ranging from 0.005 M to 0.1 M, was used as catalytic precursors, which will decompose at high temperatures to produce Fe nanoparticles. For a typical growth process, the FeCl_3 ethanol solution was first applied with a dig-pen onto one end of silicon substrates with 500 nm thermally grown oxide. The sample was then placed into a horizontal 1-inch quartz tube furnace. At ambient pressure, the furnace was heated to the desired temperature (975°C) under a flow of 120 sccm argon (Ar) and 30 sccm hydrogen (H_2), in order to decompose and reduce the catalyst complex into Fe nanoparticles. After 10 min, the Ar and H_2 flow was reduced to 6 sccm and 4 sccm, respectively. In the meanwhile, ethanol vapor was introduced into the furnace by bubbling Ar through ethanol (20°C) at a controlled rate of 20 sccm to start the CNT growth. Here, choosing ethanol as the carbon source is because it contains oxygen atoms and is also difficult to decompose without catalysts, which facilitate the growth of clean and long SWNTs. After a 40 min synthesis period, the ethanol supply was terminated and the furnace was cooled to room temperature under ~ 120 sccm Ar.

2.2. Characterization of Single-walled Carbon Nanotubes

The as-obtain samples were characterized by scanning electron microscopy (SEM, Jeol, JSM-7600F) at an accelerating voltage of 1 kV. Images with magnifications as low as $25\times$ could still clearly show the existence of SWNTs, due to a charging effect of the substrate. Atomic force microscopy (AFM, Digital Instrument IIIa, Santa Barbara, California, U.S.) in tapping mode was utilized to obtain 3D morphologies of SWNTs. The AFM height profile can give the diameter information of SWNTs. Confocal Raman system (Renishaw, Via Microscope, 50 mW) was utilized to characterize the microstructure of specific individual SWNTs. Raman imaging and Raman spectra were obtained with excitation wavelength of 514 nm through a $100\times$ objective.

2.3. Electrical Measurements on Single-walled Carbon Nanotubes

The electronic properties of individual SWNTs were studied using a back-gated FET structure at room temperature. Figure 1(a) is schematic of a typical FET geometry for electron transport measurement. An individual SWNT was positioned to bridge a pair of metal electrodes (Ti/Au, 10 nm/60 nm), which acted as the “source” and “drain”, respectively. The electrodes were fabricated on top of the SWNT-grown SiO_2 layer by lithographic techniques. The SiO_2 layer was used as the gate dielectric, whose thickness is 500 nm. The silicon wafer itself was used as the gate electrode. The SEM image [Figure 1(b)] of the device verified that there was one individual SWNT lying across the pair of metal electrodes, the channel length L varied from $20\ \mu\text{m}$ to $300\ \mu\text{m}$.

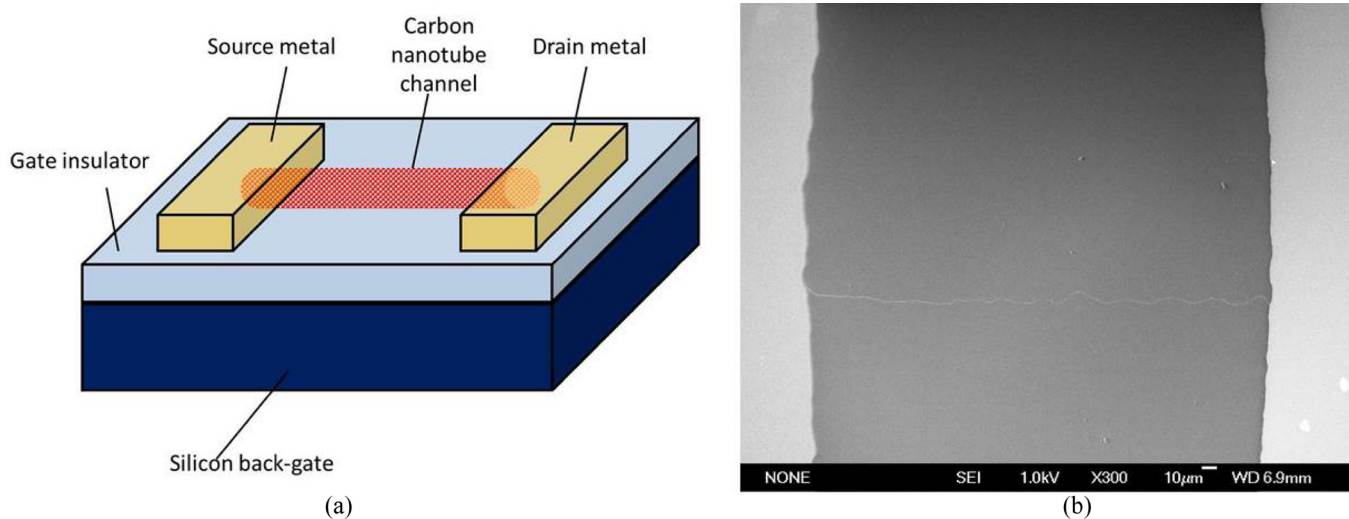


Figure 1. (a) Schematic representation of device geometry for electron transport measurement. (b) SEM image of the back-gated FET. An individual SWNT forms the FET channel connecting metal source and drain electrodes. The silicon wafer acts as the gate.

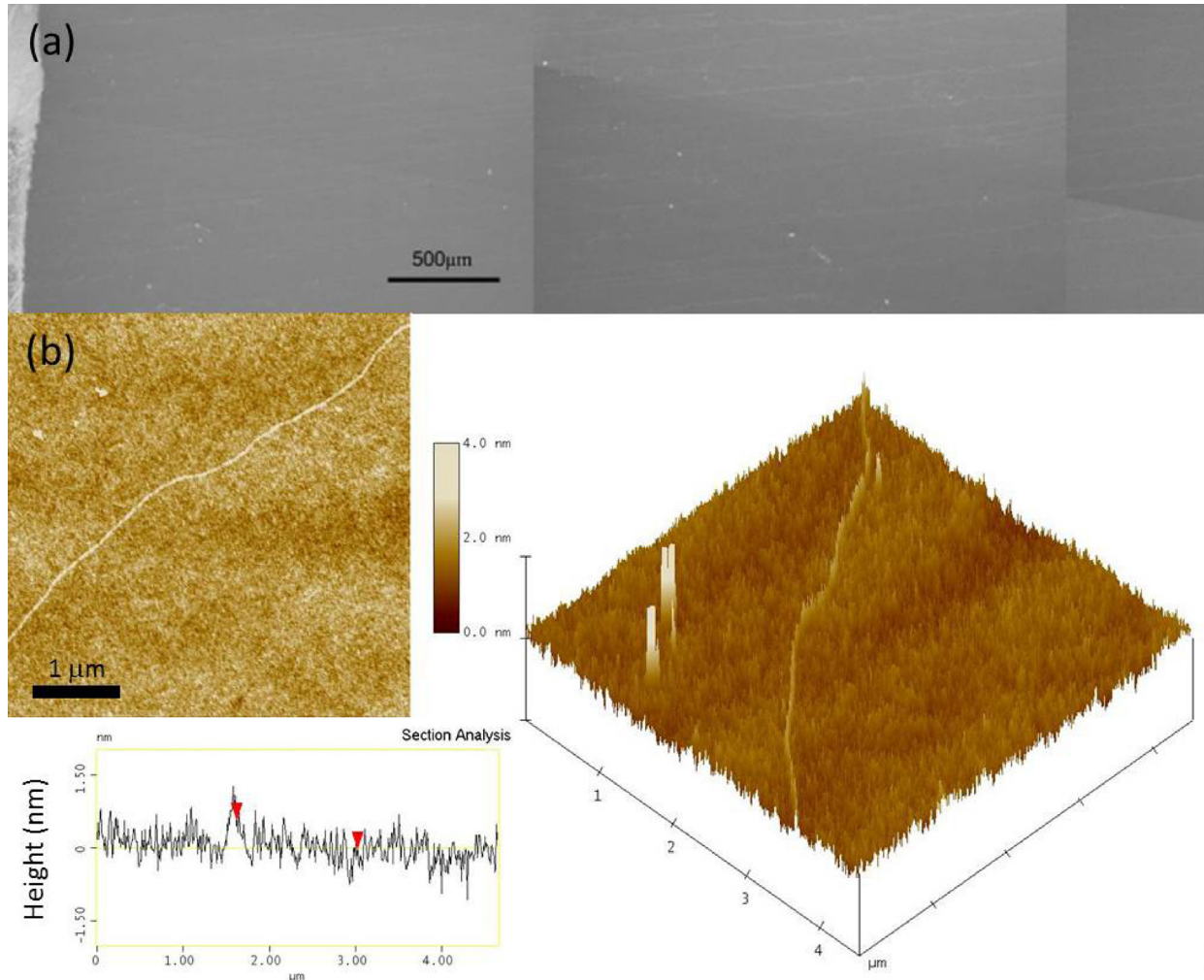


Figure 2. (a) A typical SEM image of SWNTs synthesized under the optimized growth conditions. Some of the nanotubes are able to extend to the edge of the substrate. (b) 2D and 3D AFM image of an individual SWNT grown on Si/SiO₂ substrate, respectively. Height profile indicates the diameter of the SWNT is around 1.4 nm.

3. RESULTS AND DISCUSSION

3.1. Synthesis of Ultralong Single-walled Carbon Nanotubes

Of the most common methods for CNT production, CVD is the most suitable approach because of the advantages for large scale production, diameter, length and orientation controlled growth, and in situ growth for electronics, etc [9]. Synthesis of CNTs using CVD method involves many parameters, such as carbon precursors, catalyst, temperature, pressure, gas flow rate, deposition time, and reactor geometry. Herein we present the SWNTs obtained under the optimized growth condition after carrying out a parametric study. A typical SEM image [Figure 2(a)] shows horizontally aligned SWNTs being well separated from each other, with an average spacing of 100 μm, in good alignment perpendicular to the catalyst stripe. Some of the SWNTs are able to extend over 2 cm (which is the length of the substrate). The

AFM image and the corresponding height profile reveal that as-obtained ultralong CNTs have diameters in the range of 1.3–1.9 nm, indicating these CNTs are SWNTs. Figure 2(b) shows one representative isolated nanotube, with the diameter around 1.4 nm from the height profile.

3.2. Uniformity of the Single-walled Carbon Nanotubes

Raman imaging of the as-grown SWNTs were performed with 514 nm excitation. A representative segment image of one isolated SWNT with a total length of 1 cm is shown in Figure 3(a). Figure 3(b) reveals its corresponding Raman features. The distinct RBM and the extremely weak D-band imply that the SWNT is of high-quality. RBM frequency at 171 cm⁻¹ is assigned to semiconducting tube within the resonance window under 514 nm excitation, where resonance Raman scattering is associated with the E_{33}^S transition. According to the relationship between the RBM frequency and the diameter of the tube: $d_t = 248/\omega_{RBM}$ [6], we calculate

the tube diameter to be 1.45 nm. By fitting its corresponding G band with the Lorentzian function, a sharp Lorentzian line shape is obtained, with the G^+ and G^- peaks are centered at 1598 cm^{-1} and 1576 cm^{-1} , respectively, confirming its semi-conducting nature [Figure 3(c)]. The exceedingly low intensity ratio I_D/I_G indicates that the density of defects in this segment is quite low. Figure 3(d) shows a series of Raman spectra of the typical single tube, which were obtained over $150\text{ }\mu\text{m}$ along its length. The RBM and G peak frequencies of every single spot were found the same, indicating a high degree of structural and chiral consistence in this SWNT.

Figure 4(a) and 4(b) display typical Raman features of

another individual nanotube, which is assigned to be metallic, with 514 nm excitation. The frequency of RBM with 488 nm excitation was observed $\sim 153\text{ cm}^{-1}$, this corresponds to a metallic tube with diameter of 1.62 nm. The G band shows a typical BWF line shape, indicating the metallic characteristic. A series of Raman spectra were taken along the length of the nanotube, frequencies of the RBM and G^+ peak as a function of position along the tube axis are plotted in Figure 4(c) and 4(d), respectively. The frequencies of RBM and G^+ peak are quite stable, suggesting that the diameter and chirality of the tubes do not change during the growth process.

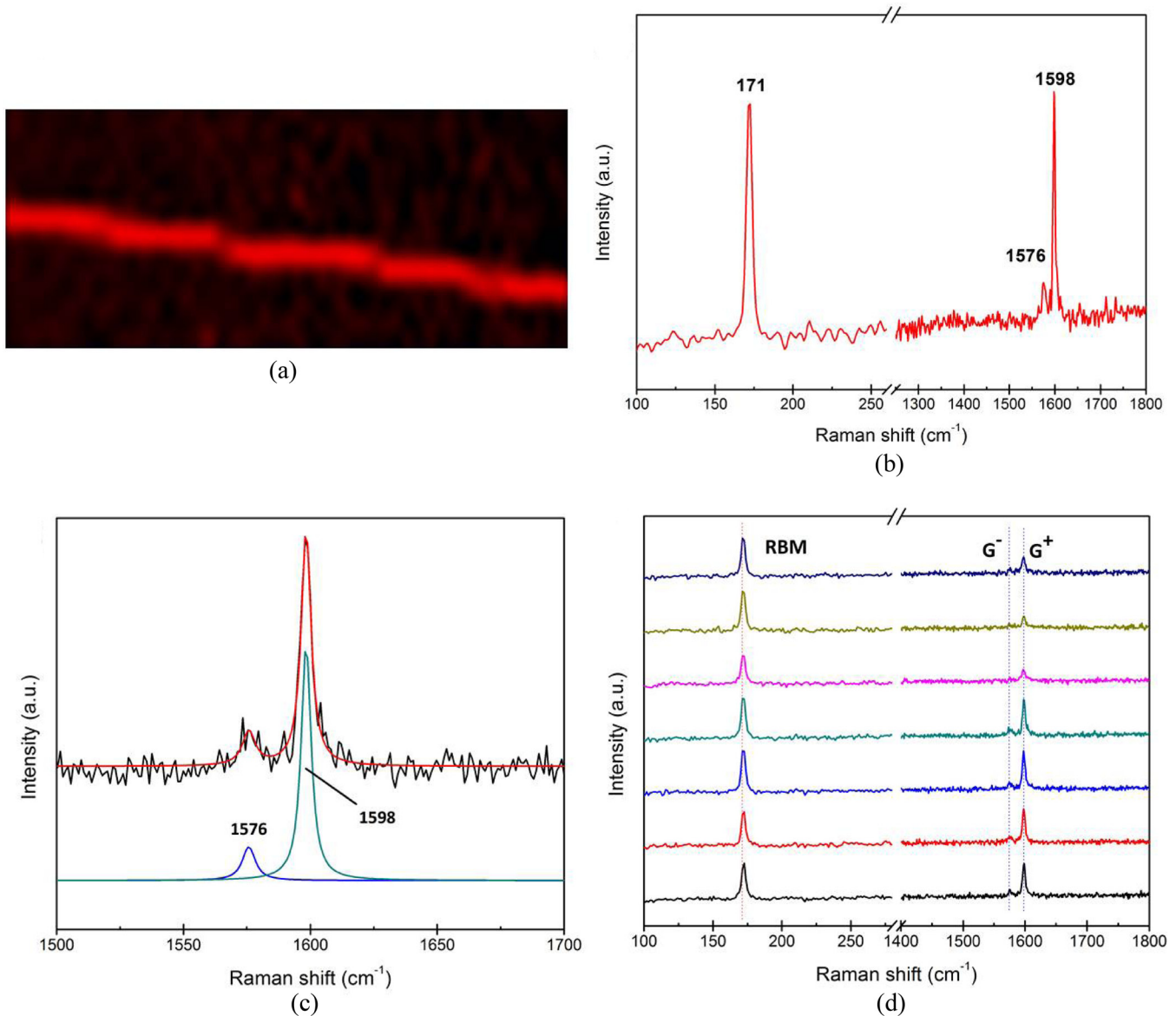


Figure 3. (a) Raman imaging of as-grown SWNTs, individual SWNTs can be identified. (b) A typical Raman spectrum of an isolated nanotube, RBM and G-band features are shown. (c) Corresponding Lorentzian fitting of G-band. (d) Evolution of Raman features of the isolated SWNT along its length. The series of Raman spectra were taken every $20\text{ }\mu\text{m}$ from left end to right end of the tube. The Raman image and spectroscopy were taken with 514 nm excitation wavelength.

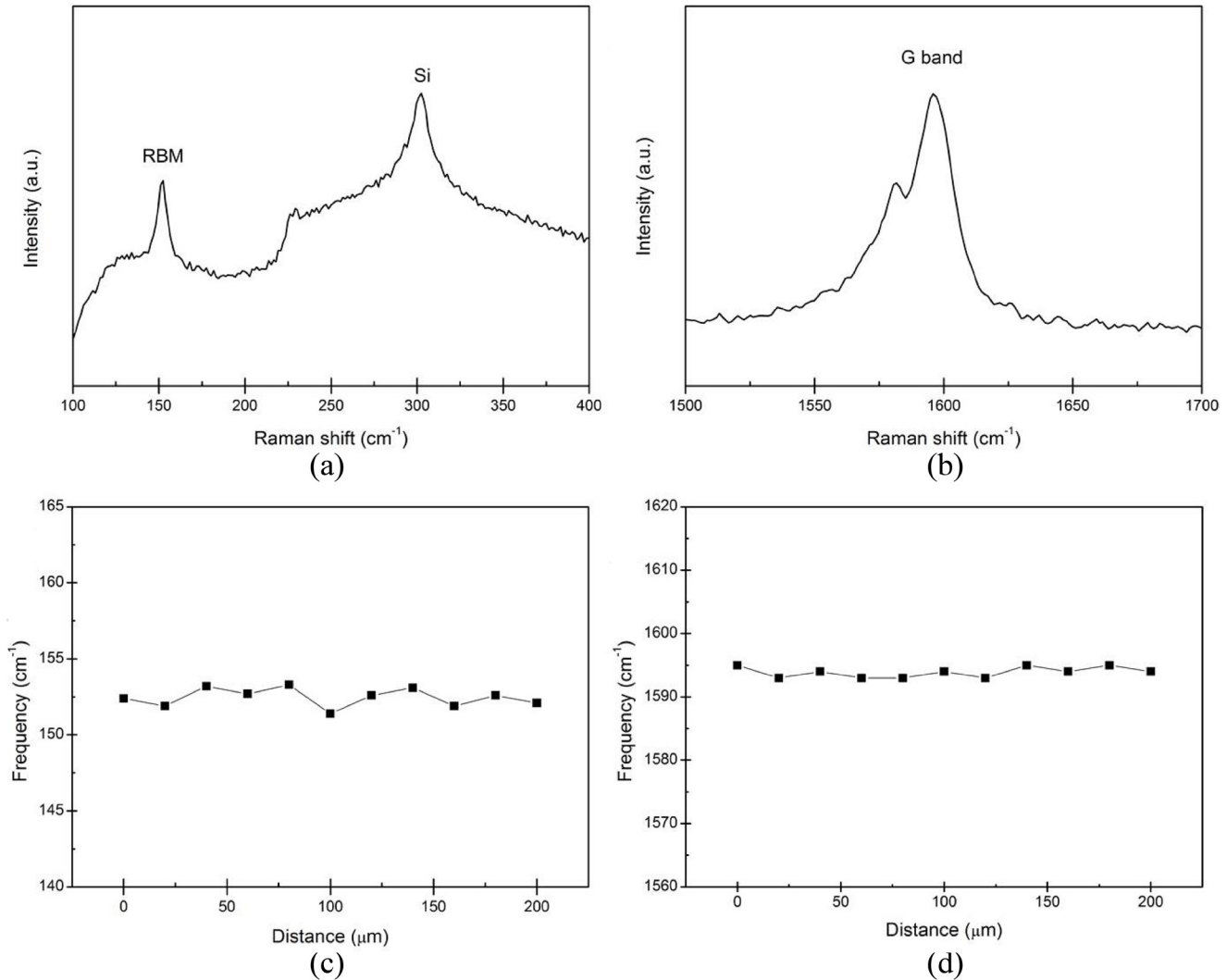


Figure 4. RBM (a) and G band (b) for a 200 μm long segment of one individual metallic SWNT. The frequency of the RBM (c) and G⁺ peak (d) of the SWNT as a function of position along its length are shown, respectively.

3.3. Electrical Measurements on Isolated Single-walled Carbon Nanotube

Since electrical properties of a SWNT are intimately related to its diameter and chirality, and also affected by its structural uniformity, we carried out electrical measurement on both metallic and semiconducting SWNTs, respectively. Figure 5(a) and 5(c) display the I-V characteristics for an individual metallic SWNT and a semiconducting SWNT, respectively. The gate voltage varied from -24 V to 24 V. The source-drain current of the metallic SWNT shows weak gate-voltage dependence, while for the semiconducting SWNT, there is an obvious “on” and “off” state in the $I_{ds}-V_g$ characteristics. The corresponding electrical behavior for the individual semiconducting SWNT incorporated in the back-gated FET device (channel length is 300 μm) is exhibited in Figure 5(d), which was recorded under constant bias voltage of 2 V. The curve displays a typical p type FET,

with the current on/off ratio (I_{on}/I_{off}) around 10^3 , which is comparable to that of short channel length SWNT FETs. The threshold voltage (V_t), the voltage where the nanotube just begins to be conductive, is extracted to be -5 V, and the corresponding transconductance (g_m) is calculated to be 81 nS.

4. CONCLUSION

In conclusion, we have successfully synthesized ultralong, horizontally aligned, well-separated SWNTs by using a CVD method. Several instruments, such as SEM, AFM, and Raman spectroscopy were utilized to characterize the as-grown SWNTs. The results show that the as-prepared SWNTs are of high quality, with relatively low density of defects. Characterization on specific individual SWNTs indicates that the nanotubes are structural and chiral uniform along their length. Semiconducting and metallic SWNTs can also be distinguished by conducting electrical measurements

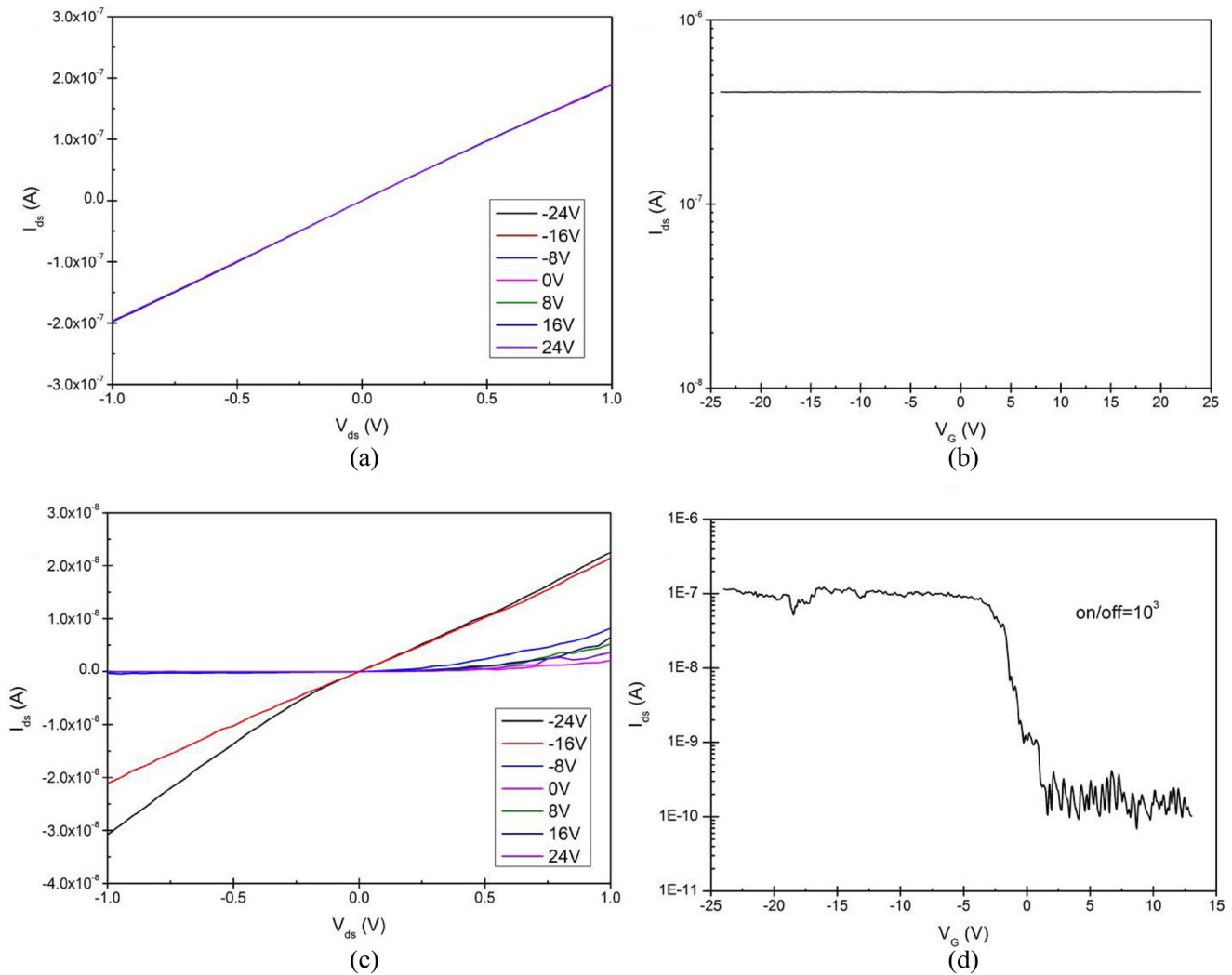


Figure 5. Measured I_{ds} - V_{ds} curves for (a) an individual metallic SWNT and (c) an individual semiconducting SWNT under seven different gate voltages. Their corresponding electrical behavior of the room-temperature current (I_{ds}) versus gate voltage (V_g) is exhibited in (b) and (d), respectively, under a bias voltage $V_{ds} = 2$ V.

on individual nanotubes. Back-gated FETs fabricated with individual semiconducting exhibited excellent performances. The extraordinary electrical properties of the ultralong, uniform SWNTs show great potential in large-scale fabrication of nanodevices on individual SWNTs.

REFERENCES

- [1] Dai, H., Javey A., Pop, E., Mann, D., Kim, W., and Lu, Y., "Electrical transport properties and field effect transistors of carbon nanotubes," *Nano*, *1*(1), 1–13 (2006). <http://dx.doi.org/10.1142/S1793292006000070>
- [2] Chen, Z., Appenzeller, J., Lin, Y., Sippel-Oakley, J., Rinzler, A., Tang, J., Wind, S. J., Solomon, P. M., and Avouris, P., "An integrated logic circuit assembled on a single carbon nanotube," *Science*, *311*(5768), 1735–1735 (2006). <http://dx.doi.org/10.1126/science.1122797> PMID:16556834
- [3] Avouris, P., Chen, Z., and Perebeinos, V., "Carbon-based electronics," *Nat. Nanotechnol.*, *2*(10), 605–615 (2007). <http://dx.doi.org/10.1038/nnano.2007.300> PMID:18654384
- [4] Li, S., Yu, Z., Rutherglen, C., and Burke, P. J., "Electrical Properties of 0.4 cm Long Single-Walled Carbon Nanotubes," *Nano Lett.*, *4*(10), 2003–2007 (2004). <http://dx.doi.org/10.1021/nl048687z>
- [5] Liu, Z., Jiao, L., Yao, Y., Xian, X., and Zhang, J., "Aligned, Ultralong Single-Walled Carbon Nanotubes: From Synthesis, Sorting, to Electronic Devices," *Adv. Mater.*, *22*(21), 2285–2310 (2010). <http://dx.doi.org/10.1002/adma.200904167> PMID:20358529
- [6] Jorio, A., Saito, R., Hafner, J. H., Lieber, C. M., Hunter, M., McClure, T., Dresselhaus, G., and Dresselhaus, M. S., "Structural (n, m) Determination of Isolated Single-Wall Carbon Nanotubes by Resonant Raman Scattering," *Phys. Rev. Lett.*, *86*(6), 1118–1121 (2001). <http://dx.doi.org/10.1103/PhysRevLett.86.1118> PMID:11178024
- [7] Dresselhaus, M.S., Dresselhaus, G., Saito, R., and Jorio, A., "Raman spectroscopy of carbon nanotubes," *Phys. Rep.*, *409*(2), 47–99 (2005). <http://dx.doi.org/10.1016/j.physrep.2004.10.006>
- [8] Zhang, Y., and Zheng, L., "Towards chirality-pure carbon nanotubes," *Nanoscale*, *2*(10), 1919–1929 (2010). <http://dx.doi.org/10.1039/c0nr00222d> PMID:20835436
- [9] Dai, H., "Carbon nanotubes: opportunities and challenges," *Surf. Sci.*, *500*(1–3), 218–241 (2002). [http://dx.doi.org/10.1016/S0039-6028\(01\)01558-8](http://dx.doi.org/10.1016/S0039-6028(01)01558-8)